


Equilibration of weakly coupled QCD plasmas

Xiaojian Du  and Sören Schlichting 

Fakultät für Physik, Universität Bielefeld, D-33615 Bielefeld, Germany

 (Received 28 January 2021; accepted 9 July 2021; published 14 September 2021)

We employ a nonequilibrium quantum chromodynamics kinetic description to study the kinetic and chemical equilibration of the quark-gluon plasma at weak coupling. Based on our numerical framework, which explicitly includes all leading order processes involving light flavor degrees of freedom, we investigate the thermalization process of homogeneous and isotropic plasmas far-from equilibrium and determine the relevant timescales for kinetic and chemical equilibration. We further simulate the longitudinally expanding preequilibrium plasma created in ultrarelativistic heavy-ion collisions at zero and nonzero density of the conserved charges and study its microscopic and macroscopic evolution toward equilibrium.

DOI: [10.1103/PhysRevD.104.054011](https://doi.org/10.1103/PhysRevD.104.054011)

I. INTRODUCTION

Nonequilibrium systems are ubiquitous in nature and of relevance to essentially all disciplines of modern physics. Despite the appearance of nonequilibrium phenomena in a variety of different contexts, there is a rather limited number of theoretical methods to study the real-time evolution of quantum systems, most of which rely on a set of approximations to study microscopic and macroscopic real-time properties of complex many-body systems.

Specifically, for fundamental theories of nature, the question of understanding and describing nonequilibrium processes in the strongly interacting quantum chromodynamics (QCD) sector of the standard model has gained considerable attention in light of high-energy heavy-ion collision experiments at the Relativistic Heavy-Ion Collider (RHIC) and the Large Hadron Collider (LHC). Somewhat surprisingly, it turns out that the complex spacetime dynamics of high-energy heavy-ion collisions on space- and timescales ~ 10 fm can be rather well described by modern formulations of relativistic viscous hydrodynamics [1], which has become the primary tool of heavy-ion phenomenology [2,3]. Nevertheless, due to the limited availability of theoretical approaches, it remains to some extent an open question how the macroscopic hydrodynamic behavior emerges from the underlying nonequilibrium dynamics of QCD, albeit significant progress in this direction has been achieved in recent years [4–15].

Beyond high-energy heavy-ion collisions similar questions arise in cosmology, where the nonequilibrium dynamics of QCD and QCD-like theories can certainly be expected to play a prominent role in producing a thermal abundance of standard model particles between the end of inflation and big bang nucleosynthesis. However, at the relevant energy scales, the field content of the early universe is not necessarily well constrained, and a detailed understanding of the thermalization of the early universe at least requires the knowledge of the coupling of the standard model degrees of freedom to the inflation sector, which makes this problem significantly more difficult. Nevertheless, studies of the thermalization of the isolated QCD sector still bear relevance to this question, as some of the basic insights into the thermalization process of QCD or QCD-like plasmas can be adapted to cosmological models, as recently discussed e.g., in Refs. [16–18].

Even though QCD exhibits essentially nonperturbative phenomena such as confinement at low energies, strong interaction matter becomes weakly coupled at asymptotically high energies owing to the renowned property of asymptotic freedom. Specifically, for thermal QCD properties, it is established from first principles lattice QCD simulations that above temperatures $T_{pc} \sim 155$ MeV [19–22] hadronic bound states dissolve into a quark-gluon plasma (QGP) and the approximate chiral symmetry of light-flavor QCD is restored. While (resummed) perturbative approaches to QCD are able to describe the most important static thermal properties of high-temperature QCD down to approximately $\sim 2T_{pc}$ [23], the perturbative description appears to be worse for dynamical properties, where e.g., next-to-leading order calculations of transport coefficients [24,25] yield large corrections to the leading order results [26,27], indicating a poor convergence of the perturbative expansion. Nevertheless, it is conceivable that

Published by the American Physical Society under the terms of the Creative Commons Attribution 4.0 International license. Further distribution of this work must maintain attribution to the author(s) and the published article's title, journal citation, and DOI. Funded by SCOAP³.

at energy scales corresponding to $\gtrsim 4T_{pc}$, achieved during the early stages of high-energy heavy-ion collisions [28], perturbative descriptions can provide useful insights into the early-time nonequilibrium dynamics of the system. Besides the potential relevance to early-universe cosmology and heavy-ion phenomenology, it is also of genuine theoretical interest to understand the unique microscopic dynamics of thermalization processes in QCD or QCD-like plasmas.

During the past few years, significant progress in understanding thermalization and “hydrodynamization,” i.e., the onset of hydrodynamic behavior, in high-energy heavy-ion collisions has been achieved, within the limiting cases of weakly coupled QCD [4,6–9] and strongly coupled holographic descriptions [11,29–31]. Despite clear microscopic differences, a common finding is that the evolution of macroscopic quantities, such as the energy momentum tensor, follows a hydrodynamic behavior well before the system reaches an approximate state of local thermal equilibrium.

Specifically, for weakly coupled QCD plasmas, a detailed microscopic understanding of the thermalization process has also been established, as described e.g., in the recent reviews [32,33]. Different weak-coupling thermalization scenarios based on parametric estimates [34–37] distinguish between two broadly defined classes of nonequilibrium systems, commonly referred to as overoccupied or underoccupied [32], which undergo qualitatively different thermalization processes. While the thermalization of overoccupied QCD plasmas proceeds via a self-similar direct energy cascade [38–41], as is the case for many far-from equilibrium systems [42–44], underoccupied QCD plasmas undergo the so-called “bottom-up” scenario [34] where thermalization proceeds via an inverse energy cascade, which is in many ways unique to QCD and QCD-like systems. Earlier parametric estimates have now been supplemented with detailed simulations of the nonequilibrium dynamics based on classical-statistical lattice gauge theory [38–41,45] and effective kinetic theory [46–51]. However, with the exception of Refs. [47,50], all of the aforementioned studies have been performed for $SU(N_c)$ Yang-Mills theory, i.e., only taking into account the bosonic degrees of freedom and neglecting the effect of dynamical fermions.

The central objective of this paper is to extend the study of thermalization processes of weakly coupled non-Abelian plasmas to include all relevant quark and gluon degrees of freedom. Based on the leading order effective kinetic theory of QCD [52], we perform numerical simulations of the nonequilibrium dynamics of the QGP, to characterize the mechanisms and timescales for kinetic and chemical equilibration processes. By explicitly taking into account all light flavor degrees of freedom, i.e., gluons (g) as well as $u, \bar{u}, d, \bar{d}, s, \bar{s}$ quarks/antiquarks, we further investigate the nonequilibrium dynamics of

QCD plasmas at zero and nonzero values of the conserved u, d, s charges.

We organize the discussion in this paper as follows. We begin with a brief explanation of the general setup in Sec. II, where we discuss the characterization of weakly coupled nonequilibrium QCD plasmas in Sec. II A and outline their effective kinetic description in Sec. II B. Based on this framework, we study different thermalization mechanisms of the QGP, starting with the chemical equilibration of near-equilibrium systems in Sec. III. Subsequently, in Sec. IV we investigate kinetic and chemical equilibration processes in far-from equilibrium systems considering the two stereotypical examples of overoccupied systems in Sec. IV A and underoccupied systems in Sec. IV B. In Sec. V we continue with the study of longitudinally expanding QCD plasmas, which are relevant to describe the early time dynamics of high-energy heavy-ion collisions. Here, we mainly focus on the microscopic aspects underlying the isotropization of the pressure and evolution of the QGP chemistry at zero and nonzero net-baryon density, and we refer to our companion paper [53] for additional discussions on the implications of our findings in the context of relativistic heavy-ion collisions. We conclude in Sec. VI with a brief summary of our most important findings and a discussion of possible future extensions. Appendixes A, B, and C contain additional details regarding the details of our numerical implementation of the QCD kinetic equations.

II. NONEQUILIBRIUM QCD

Generally the description of nonequilibrium processes in QCD represents a challenging task, and at present can only be achieved in limiting cases, such as the weak coupling limit. We employ a leading order kinetic description of QCD [52], where the nonequilibrium evolution of the system is described in terms of the phase-space density $f(\vec{x}, \vec{p}, t)$ of on-shell quarks and gluons. We will focus on homogenous systems, for which the phase-space density $f(\vec{x}, \vec{p}, t) = f(\vec{p}, t)$ only depends on momenta and time, and investigate the nonequilibrium dynamics of the QGP, based on numerical solutions of the QCD kinetic equations. Below we provide an overview of the relevant ingredients, with additional details on the numerical implementation provided in Appendixes A, B, and C.

A. Nonequilibrium properties of the quark-gluon plasma

Before we address the details of the QCD kinetic description, we briefly introduce a few relevant quantities that will be used to characterize static properties and interactions in nonequilibrium systems. We first note that both equilibrium, as well as nonequilibrium systems can

be characterized in terms of their conserved charges, which for the light flavor degrees of freedom of QCD correspond to the conserved energy density e , and the conserved net-charge densities Δn_u , Δn_d , Δn_s of up, down, and strange quarks. Evidently in thermal equilibrium, the maximal entropy principle uniquely determines the phase-space distribution of gluons and quarks,

$$\begin{aligned} f_g^{\text{eq}}(p, T) &= \frac{1}{e^{p/T} - 1}, \\ f_{q_f}^{\text{eq}}(p, T, \mu_f) &= \frac{1}{e^{(p-\mu_f)/T} + 1}, \\ f_{\bar{q}_f}^{\text{eq}}(p, T, \mu_f) &= \frac{1}{e^{(p+\mu_f)/T} + 1}, \end{aligned} \quad (1)$$

with well-defined temperature T_{eq} and chemical potential $\mu_{f,\text{eq}}$ determined by the values of the densities of the charges according to

$$\begin{aligned} e &= \int \frac{d^3 p}{(2\pi)^3} p \left[\nu_g f_g(\vec{p}) + \nu_q \sum_f (f_{q_f}(\vec{p}) + f_{\bar{q}_f}(\vec{p})) \right] \\ &\stackrel{\text{(eq)}}{=} \left[\nu_g \frac{\pi^2}{30} + \nu_q \frac{\pi^2}{120} \sum_f \left(7 + \frac{30}{\pi^2} z_f^2 + \frac{15}{\pi^4} z_f^4 \right) \right] T_{\text{eq}}^4, \\ \Delta n_f &= (n_q - n_{\bar{q}})_f = \int \frac{d^3 p}{(2\pi)^3} [\nu_q (f_{q_f}(\vec{p}) - f_{\bar{q}_f}(\vec{p}))] \\ &\stackrel{\text{(eq)}}{=} \frac{\nu_q}{6} \left[z_f + \frac{1}{\pi^2} z_f^3 \right] T_{\text{eq}}^3. \end{aligned} \quad (2)$$

where we denote $z_f = \frac{\mu_{f,\text{eq}}}{T_{\text{eq}}}$ for the three light flavors $f = u, d, s$, which we will treat as massless throughout this work. Even though a nonequilibrium system can no longer be characterized uniquely in terms of its conserved charges, it is nevertheless useful to associate effective temperatures T_{ldm} and chemical potentials $\mu_{f,ldm}$ with the system, which can be determined via the so-called Landau matching procedure of determining T_{ldm} , $\mu_{f,ldm}$ from the conserved charges according to the relations in Eq. (2). Specifically for systems with conserved energy and charge densities, T_{ldm} and $\mu_{f,ldm}$ will ultimately determine the equilibrium temperature $T_{\text{eq}} = T_{ldm}$ and chemical potential $\mu_{f,\text{eq}} = \mu_{f,ldm}$ once the system has thermalized.

Besides the densities of the conserved quantities, there is another set of important quantities relevant to describe the interactions in nonequilibrium QCD plasmas [52]. Specifically, this includes the in-medium screening masses of quarks and gluons, which in the case of the gluon can be expressed as in terms of the Debye mass

$$\begin{aligned} m_D^2 &= \frac{4g^2}{d_A} \int \frac{d^3 p}{(2\pi)^3} \frac{1}{2p} \left[\nu_g C_A f_g(\vec{p}) \right. \\ &\quad \left. + \nu_q C_F \sum_f (f_{q_f}(\vec{p}) + f_{\bar{q}_f}(\vec{p})) \right] \\ &\stackrel{\text{(eq)}}{=} \frac{g^2}{6d_A} \left[\nu_g C_A + \nu_q C_F \sum_f \left(1 + \frac{3}{\pi^2} z_f^2 \right) \right] T_{\text{eq}}^2 \end{aligned} \quad (3)$$

with nonequilibrium gluon and quark distributions $f_g(\vec{p})$, $f_q(\vec{p})$, $f_{\bar{q}}(\vec{p})$. Similarly, the thermal quark masses $m_{Q_f}^2$ for $f = u, d, s$ quarks also enter in the kinetic description and can be expressed as

$$\begin{aligned} m_{Q_f}^2 &= g^2 C_F \int \frac{d^3 p}{(2\pi)^3} \frac{1}{2p} [2f_g(\vec{p}) + (f_{q_f}(\vec{p}) + f_{\bar{q}_f}(\vec{p}))] \\ &\stackrel{\text{(eq)}}{=} \frac{g^2}{8} C_F \left[1 + \frac{1}{\pi^2} z_f^2 \right] T_{\text{eq}}^2. \end{aligned} \quad (4)$$

While the screening masses m_D^2 and $m_{Q_f}^2$ determine the elastic scattering matrix elements, the calculation of the effective rates for inelastic processes also requires the asymptotic masses of quarks and gluons, $m_{\infty,a}^2$ which to leading order in perturbation theory can be related to the respective screening masses according to $m_{\infty,g}^2 = m_D^2/2$ and $m_{\infty,Q_f}^2 = 2m_{Q_f}^2$. Since inelastic interactions are induced by elastic collisions, their effective in-medium rates are also sensitive to the density of elastic interaction partners

$$\begin{aligned} m_D^2 T^* &= \frac{g^2}{d_A} \int \frac{d^3 p}{(2\pi)^3} \left\{ \nu_g C_A f_g(\vec{p}) (1 + f_g(\vec{p})) \right. \\ &\quad \left. + \nu_q C_F \sum_f [f_{q_f}(\vec{p}) (1 - f_{q_f}(\vec{p})) \right. \\ &\quad \left. + f_{\bar{q}_f}(\vec{p}) (1 - f_{\bar{q}_f}(\vec{p}))] \right\}, \end{aligned} \quad (5)$$

which receives the usual Bose enhancement $f_g(\vec{p})(1 + f_g(\vec{p}))$ and Fermi blocking $f_{q/\bar{q}}(\vec{p})(1 - f_{q/\bar{q}}(\vec{p}))$ factors. Since we will frequently characterize the nonequilibrium evolution of the QGP in terms of the above dynamical scales, we further note that the quantity $g^2 T^*$ characterizes the rate of small angle scatterings in the plasma, with T^* defined such that in equilibrium $T^* \stackrel{\text{(eq)}}{=} T_{\text{eq}}$ corresponds to the equilibrium temperature.

B. Effective kinetic theory of quark-gluon plasma

We adopt an effective kinetic description of the QGP, which at leading order includes both “2 ↔ 2” elastic processes as well as effective “1 ↔ 2” collinear inelastic processes. Specifically for a spatially homogeneous system, the time evolution of the phase-space density of quarks

and gluons is then described by the Boltzmann equation for QCD light particles “ $a = g, u, \bar{u}, d, \bar{d}, s, \bar{s}$ ”

$$\frac{\partial}{\partial t} f_a(\vec{p}, t) = -C_a^{2 \leftrightarrow 2}[f](\vec{p}, t) - C_a^{1 \leftrightarrow 2}[f](\vec{p}, t), \quad (6)$$

where $C_a^{2 \leftrightarrow 2}[f](\vec{p}, t)$ is the $2 \leftrightarrow 2$ elastic collision term and $C_a^{1 \leftrightarrow 2}[f](\vec{p}, t)$ is the $1 \leftrightarrow 2$ inelastic collision term.

With regards to the numerical implementation, we follow previous works and solve the QCD Boltzmann equation directly as an integro-differential equation using pseudo-spectral methods [31,54]. Our numerical implementation of the nonequilibrium dynamics relies on a discretized form of the Boltzmann equation

$$\begin{aligned} n(i_p, j_\theta, k_\phi, t) &= \int \frac{d^3 p}{(2\pi)^3} W_{(i_p, j_\theta, k_\phi)}(\vec{p}) f(\vec{p}, t) \\ &= \int \frac{d^3 p}{(2\pi)^3} w_i^{(p)}(p) w_j^{(\theta)}(\theta) w_k^{(\phi)}(\phi) f(\vec{p}, t), \end{aligned} \quad (7)$$

based on a weight function algorithm [55], which is described in detail in Appendix A. Based on Eq. (7), the discretized form of the Boltzmann equation for species “ a ” can be written as

$$\begin{aligned} \frac{\partial}{\partial t} n_a(i_p, j_\theta, k_\phi, t) \\ = -C_a^{2 \leftrightarrow 2}[n](i_p, j_\theta, k_\phi, t) - C_a^{1 \leftrightarrow 2}[n](i_p, j_\theta, k_\phi, t), \end{aligned} \quad (8)$$

where in accordance with Eq. (7), $C_a^{2 \leftrightarrow 2}[n](i_p, j_\theta, k_\phi, t)$ and $C_a^{1 \leftrightarrow 2}[n](i_p, j_\theta, k_\phi, t)$ correspond to discretized moments of the collision integral as described in Appendix B. Based on a suitable choice of the weight functions $w_i^{(p)}(p)$, $w_j^{(\theta)}(\theta)$, and $w_k^{(\phi)}(\phi)$, the discretization of the collision integrals is performed such that it ensures an exact conservation of the particle number for elastic collision, as well as an exact conservation of energy for both elastic and inelastic collisions. The evolution algorithm of the discretized form of the Boltzmann equation is described in Appendix C.

1. Elastic collisions

Within our effective kinetic description, we include all leading order elastic scattering processes between quarks and gluons, where following previous works [4,7,46,50] the relevant in-medium scattering matrix elements are determined based on an effective isotropic screening assumption.

a. Collision integral.—We follow the notation of Arnold, Moore, and Yaffe (AMY) [52], where the elastic collision integrals for particle a with momentum \vec{p}_1 participating in

scattering process $a, b \rightarrow c, d$ with $p_1, p_2 \leftrightarrow p_3, p_4$ take the form

$$\begin{aligned} C_a^{2 \leftrightarrow 2}[f](\vec{p}_1) &= \frac{1}{2\nu_a} \frac{1}{2E_{p_1}} \\ &\times \sum_{cd} \int d\Pi_{2 \leftrightarrow 2} |\mathcal{M}_{cd}^{ab}(\vec{p}_1, \vec{p}_2 | \vec{p}_3, \vec{p}_4)|^2 F_{cd}^{ab}(\vec{p}_1, \vec{p}_2 | \vec{p}_3, \vec{p}_4) \end{aligned} \quad (9)$$

with $d\Pi_{2 \leftrightarrow 2}$ denoting the measure

$$\begin{aligned} d\Pi_{2 \leftrightarrow 2} &= \frac{d^3 p_2}{(2\pi)^3} \frac{1}{2E_{p_2}} \frac{d^3 p_3}{(2\pi)^3} \frac{1}{2E_{p_3}} \frac{d^3 p_4}{(2\pi)^3} \frac{1}{2E_{p_4}} \\ &\times (2\pi)^4 \delta^{(4)}(p_1 + p_2 - p_3 - p_4) \end{aligned} \quad (10)$$

and $\nu_G = 2(N_c^2 - 1) = 16$, $\nu_Q = 2N_c = 6$ denoting the number of gluon and quark degrees of freedom. By $|\mathcal{M}_{cd}^{ab}(\vec{p}_1, \vec{p}_2 | \vec{p}_3, \vec{p}_4)|^2$ we denote the square matrix element for the process “ $a, b \leftrightarrow c, d$ ” summed over spin and color for all particles, while $F_{cd}^{ab}(\vec{p}_1, \vec{p}_2 | \vec{p}_3, \vec{p}_4)$ is the statistical factor for the “ $a, b \leftrightarrow c, d$ ” scattering process

$$\begin{aligned} F_{cd}^{ab}(\vec{p}_1, \vec{p}_2 | \vec{p}_3, \vec{p}_4) \\ = f_a(\vec{p}_1) f_b(\vec{p}_2) (1 \pm f_c(\vec{p}_3)) (1 \pm f_d(\vec{p}_4)) \\ - f_c(\vec{p}_3) f_d(\vec{p}_4) (1 \pm f_a(\vec{p}_1)) (1 \pm f_b(\vec{p}_2)) \end{aligned} \quad (11)$$

where “ \pm ” provides a Bose enhancement (+) for gluons and Fermi blocking (−) for quarks, such that the first term in Eq. (11) represents a loss term, whereas the second term in Eq. (11) corresponds to a gain term associated with the inverse process.

b. Scattering matrix elements.—Elastic scattering matrix elements for the various $2 \leftrightarrow 2$ processes can be calculated in perturbative QCD (pQCD) [52], with the corresponding leading order matrix elements listed in Table I, where g is the gauge coupling, $s = (p_1 + p_2)^2$, $t = (p_1 - p_3)^2$ and $u = (p_1 - p_4)^2$ denote the usual Mandelstam variables, and $C_F = \frac{N_c^2 - 1}{2N_c} = \frac{4}{3}$, $C_A = N_c = 3$, $d_F = N_c = 3$, $d_A = N_c^2 - 1 = 8$ denote the group theoretical factors. However, due to the enhancement of soft t , u -channel gluon and quark exchanges, the vacuum matrix elements in Table I give rise to divergent scattering rates, which inside the medium are regulated by incorporating screening effects via the insertions of the hard-thermal loop (HTL) self-energies, as discussed in detail in [52]. Even though it should in principle be possible to include the full HTL self-energies in the calculation of the in-medium elastic scattering matrix elements (at least for homogenous and isotropic systems), this would represent yet another significant complication as the corresponding expressions would have to be reevaluated numerically at each time step and we did not pursue

TABLE I. Summary of $2 \leftrightarrow 2$ elastic processes and their leading order pQCD scattering amplitudes.

| Processes $a, b \leftrightarrow c, d$ | Matrix element $ \mathcal{M}_{cd}^{ab}(\vec{p}_1, \vec{p}_2 \vec{p}_3, \vec{p}_4) ^2$ |
|--|--|
| $gg \leftrightarrow gg$ | $4g^4 d_A C_A^2 (9 + \frac{(s-u)^2}{t} + \frac{(s-t)^2}{u} + \frac{(t-u)^2}{s^2})$ |
| $qg \leftrightarrow qg, \bar{q}g \leftrightarrow \bar{q}g$ | $-8g^4 d_F C_F^2 (\frac{u}{s} + \frac{s}{u}) + 8g^4 d_F C_F C_A (\frac{s^2+u^2}{t})$ |
| $q\bar{q} \leftrightarrow gg$ | $8g^4 d_F C_F^2 (\frac{u}{t} + \frac{t}{u}) - 8g^4 d_F C_F C_A (\frac{t^2+u^2}{s^2})$ |
| $qq \leftrightarrow qq, \bar{q}\bar{q} \leftrightarrow \bar{q}\bar{q}$ | $8g^4 \frac{d_F^2 C_F^2}{d_A} (\frac{t^2+s^2}{u} + \frac{u^2+s^2}{t}) + 16g^4 d_F C_F (C_F - \frac{C_A}{2}) (\frac{s^2}{t} \underline{u})$ |
| $q\bar{q} \leftrightarrow q\bar{q}$ | $8g^4 \frac{d_F^2 C_F^2}{d_A} (\frac{s^2+u^2}{t} + \frac{t^2+u^2}{s^2}) + 16g^4 d_F C_F (C_F - \frac{C_A}{2}) (\frac{u^2}{st})$ |
| $q_1 q_2 \leftrightarrow q_1 q_2$ | $8g^4 \frac{d_F^2 C_F^2}{d_A} (\frac{s^2+u^2}{t})$ |
| $q_1 \bar{q}_2 \leftrightarrow q_1 \bar{q}_2$ | |
| $\bar{q}_1 \bar{q}_2 \leftrightarrow \bar{q}_1 \bar{q}_2$ | |
| $q_1 \bar{q}_1 \leftrightarrow q_2 \bar{q}_2$ | $8g^4 \frac{d_F^2 C_F^2}{d_A} (\frac{t^2+u^2}{s^2})$ |

this further. Instead, we follow previous works [4,7,46,50], and incorporate an effective isotropic screening, where soft t - and u -channel exchanges are regulated by screening masses m_D^2 and $m_{Q_f}^2$ for different species of internal exchange particles, by replacing t and u in the singly and doubly underlined expressions in Table I with

$$\begin{aligned} \underline{t} &= t \left(1 + \frac{\xi_g^2 m_D^2}{\vec{q}_t^2} \right), & \underline{u} &= u \left(1 + \frac{\xi_g^2 m_D^2}{\vec{q}_u^2} \right), \\ \underline{\underline{t}} &= t \left(1 + \frac{\xi_q^2 m_{Q_f}^2}{\vec{q}_t^2} \right), & \underline{\underline{u}} &= u \left(1 + \frac{\xi_q^2 m_{Q_f}^2}{\vec{q}_u^2} \right), \end{aligned} \quad (12)$$

where $\vec{q}_t = \vec{p}_1 - \vec{p}_3$, $\vec{q}_u = \vec{p}_1 - \vec{p}_4$ is the spatial momentum of the exchanged particle and the parameters $\xi_g = \frac{e_b^5}{2\sqrt{2}}$ and $\xi_q = \frac{e}{\sqrt{2}}$ have been determined in [50] by matching to leading order HTL results. Based on the above expressions for the collision integrals and scattering matrix elements, the corresponding integrals for the discretized moments $C_a^{2 \leftrightarrow 2}[n](i_p, j_\theta, k_\phi, t)$ are then calculated at each time step by performing a Monte Carlo sampling described in detail in Appendix B 1.

2. Inelastic collisions

Within our effective kinetic description, we include all leading order inelastic scattering processes between quarks and gluons, where following previous works [4,7,46,50] the relevant in-medium scattering matrix elements are determined within the formalism of Arnold, Moore, and Yaffe [52], by solving an integro-differential equation for the effective collinear emission/absorption rates to take into account coherence effects associated with the Landau-Pomeranchuk-Migdal (LPM) effect [56–58].

a. Collision integral.—Generally, the inelastic collision integral for particle “a” with momentum \vec{p}_1 participating

in the splitting process $a \rightarrow b, c$ ($p_1 \leftrightarrow p_2, p_3$) and the inverse joining process $a, b \rightarrow c$ ($p_1, p_2 \leftrightarrow p_3$) takes the form

$$\begin{aligned} C_a^{1 \leftrightarrow 2}[f](\vec{p}_1) &= \frac{1}{2\nu_a} \frac{1}{2E_{p_1}} \sum_{bc} \int d\Pi_{1 \leftrightarrow 2}^{a \leftrightarrow bc} |\mathcal{M}_{bc}^a(\vec{p}_1 | \vec{p}_2, \vec{p}_3)|^2 F_{bc}^a(\vec{p}_1 | \vec{p}_2, \vec{p}_3) \\ &+ \frac{1}{\nu_a} \frac{1}{2E_{p_1}} \int d\Pi_{1 \leftrightarrow 2}^{ab \leftrightarrow c} |\mathcal{M}_c^{ab}(\vec{p}_1, \vec{p}_2 | \vec{p}_3)|^2 F_c^{ab}(\vec{p}_1, \vec{p}_2 | \vec{p}_3) \\ &= \frac{1}{2\nu_a} \frac{1}{2E_{p_1}} \sum_{bc} \int d\Pi_{1 \leftrightarrow 2}^{a \leftrightarrow bc} |\mathcal{M}_{bc}^a(\vec{p}_1 | \vec{p}_2, \vec{p}_3)|^2 F_{bc}^a(\vec{p}_1 | \vec{p}_2, \vec{p}_3) \\ &- \frac{1}{\nu_a} \frac{1}{2E_{p_1}} \int d\Pi_{1 \leftrightarrow 2}^{ab \leftrightarrow c} |\mathcal{M}_{ab}^c(\vec{p}_3 | \vec{p}_1, \vec{p}_2)|^2 F_{ab}^c(\vec{p}_3 | \vec{p}_1, \vec{p}_2), \end{aligned} \quad (13)$$

where $d\Pi_{1 \leftrightarrow 2}^{a \leftrightarrow bc}$ and $d\Pi_{1 \leftrightarrow 2}^{ab \leftrightarrow c}$ denote the measures

$$\begin{aligned} \int d\Pi_{1 \leftrightarrow 2}^{a \leftrightarrow bc} &= \int \frac{d^3 p_2}{(2\pi)^3} \frac{1}{2E_{p_2}} \int \frac{d^3 p_3}{(2\pi)^3} \frac{1}{2E_{p_3}} \\ &\times (2\pi)^4 \delta^{(4)}(p_1 - p_2 - p_3), \\ \int d\Pi_{1 \leftrightarrow 2}^{ab \leftrightarrow c} &= \int \frac{d^3 p_2}{(2\pi)^3} \frac{1}{2E_{p_2}} \int \frac{d^3 p_3}{(2\pi)^3} \frac{1}{2E_{p_3}} \\ &\times (2\pi)^4 \delta^{(4)}(p_1 + p_2 - p_3). \end{aligned} \quad (14)$$

$|\mathcal{M}_{bc}^a(\vec{p}_1 | \vec{p}_2, \vec{p}_3)|^2$ and $|\mathcal{M}_c^{ab}(\vec{p}_1, \vec{p}_2 | \vec{p}_3)|^2$ are the matrix element squares for process “ $a \leftrightarrow b, c$ ” and “ $a, b \leftrightarrow c$.” $F_{cd}^a(\vec{p}_1 | \vec{p}_3, \vec{p}_4)$ and $F_c^{ab}(\vec{p}_1, \vec{p}_2 | \vec{p}_3)$ are the statistical factors

$$\begin{aligned} F_{bc}^a(\vec{p}_1 | \vec{p}_2, \vec{p}_3) &= f_a(\vec{p}_1) (1 \pm f_b(\vec{p}_2)) (1 \pm f_c(\vec{p}_3)) \\ &- f_b(\vec{p}_2) f_c(\vec{p}_3) (1 \pm f_a(\vec{p}_1)), \\ F_c^{ab}(\vec{p}_1, \vec{p}_2 | \vec{p}_3) &= f_a(\vec{p}_1) f_b(\vec{p}_2) (1 \pm f_c(\vec{p}_3)) \\ &- f_c(\vec{p}_3) (1 \pm f_a(\vec{p}_1)) (1 \pm f_b(\vec{p}_2)), \end{aligned} \quad (15)$$

where again “±” provides a Bose enhancement (+) for gluon and Fermi blocking (−) for quarks.

Since for ultrarelativistic particles, the $1 \leftrightarrow 2$ processes require collinearity to be kinematically allowed, the collision integral in Eq. (13) can be recast into an effectively one-dimensional collinear process

$$C_a^{1 \leftrightarrow 2}[f](p) = \frac{1}{2\nu_a} \int_0^1 dz \left[\sum_{bc} \frac{d\Gamma_{bc}^a}{dz}(p, z) \nu_a F_{bc}^a(p|z p, \bar{z} p) - \frac{1}{z^3} \frac{d\Gamma_{ab}^c}{dz}\left(\frac{p}{z}, z\right) \nu_c F_{ab}^c\left(\frac{p}{z} \middle| p, \frac{\bar{z}}{z} p\right) - \frac{1}{\bar{z}^3} \frac{d\Gamma_{ab}^c}{dz}\left(\frac{p}{\bar{z}}, \bar{z}\right) \nu_c F_{ab}^c\left(\frac{p}{\bar{z}} \middle| p, \frac{z}{\bar{z}} p\right) \right], \quad (16)$$

where z and $\bar{z} = 1 - z$ are the collinear splitting/joining fractions, and the effective inelastic rate $\frac{d\Gamma_{bc}^a}{dz}$ in Eq. (16) is obtained within the framework of AMY [52], by considering the overall probability of a single radiative emission/absorption over the course of multiple successive elastic interactions, reduced to an effective collinear rate by integrating over the parametrically small transverse momentum accumulated during the emission/absorption process.¹

b. Effective inelastic rate.—Based on the formalism of AMY [52], the effective inelastic rate can be expressed in the following factorized form:

$$\frac{d\Gamma_{bc}^a}{dz}(p, z) = \frac{\alpha_s P_{bc}^a(z)}{[2pz(1-z)]^2} \int \frac{d^2 \vec{p}_b}{(2\pi)^2} \text{Re}[2\vec{p}_b \cdot \vec{g}_{(p,z)}(\vec{p}_b)], \quad (17)$$

where the matrix element for the collinear splitting is expressed in terms of the leading-order QCD splitting functions Dokshitzer–Gribov–Lipatov–Altarelli–Parisi (DGLAP) [60–62],

$$\begin{aligned} P_{gg}^g(z) &= \frac{2C_A(1-z(1-z))^2}{z(1-z)}, \\ P_{qq}^g(z) &= \frac{z^2 + (1-z)^2}{2}, \\ P_{gq}^q(z) &= \frac{C_F(1 + (1-z)^2)}{z}, \\ P_{qq}^q(z) &= \frac{C_F(1 + z^2)}{1-z}. \end{aligned} \quad (18)$$

Second, the factor $\int \frac{d^2 \vec{p}_b}{(2\pi)^2} \text{Re}[2\vec{p}_b \cdot \vec{g}_{(p,z)}(\vec{p}_b)]$ encodes the relevant aspects of the current-current correlation function inside the medium and satisfies the following integral

¹We note that several different notations for the rate $\frac{d\Gamma_{bc}^a}{dz}$ exist in the literature, and we refer to the Appendix of Ref. [59] for a comparison of different notations.

equation for particles a, b, c carrying momentum fraction $1, z, 1 - z$,

$$\begin{aligned} 2\vec{p}_b &= i\delta E_{(p,z)}(\vec{p}_b) \times \vec{g}_{(p,z)}(\vec{p}_b) + \frac{1}{2} \int \frac{d^2 \vec{q}}{(2\pi)^2} \frac{d\bar{\Gamma}^{\text{el}}}{d^2 \vec{q}} \\ &\times \{ (C_b^R + C_c^R - C_a^R) [\vec{g}_{(p,z)}(\vec{p}_b) - \vec{g}_{(p,z)}(\vec{p}_b - \vec{q})] \\ &+ (C_c^R + C_a^R - C_b^R) [\vec{g}_{(z,p)}(\vec{p}_b) - \vec{g}_{(p,z)}(\vec{p}_b - z\vec{q})] \\ &+ (C_a^R + C_b^R - C_c^R) [\vec{g}_{(p,z)}(\vec{p}_b) - \vec{g}_{(p,z)}(\vec{p}_b - (1-z)\vec{q})] \}, \end{aligned} \quad (19)$$

with

$$\delta E_{(p,z)}(\vec{p}_b) = \frac{\vec{p}_b^2}{2pz(1-z)} + \frac{m_{\infty,b}^2}{2zp} + \frac{m_{\infty,c}^2}{2(1-z)p} - \frac{m_{\infty,a}^2}{2p}, \quad (20)$$

where $m_{\infty,a}^2, m_{\infty,b}^2, m_{\infty,c}^2$ denote the asymptotic masses of particles a, b, c , i.e., $m_{\infty,g}^2 = \frac{m^2}{2}$ for gluons and $m_{\infty,q_f}^2 = 2m_{Q_f}^2$ for quarks; C_a^R, C_b^R, C_c^R denote the Casimir of the representation of, i.e., $C_q^R = C_F$ for quarks and $C_g^R = C_A$ for gluons; and $\frac{d\bar{\Gamma}^{\text{el}}}{d^2 \vec{q}}$ denotes the differential elastic scattering rate stripped by its color factor, which is given by

$$\frac{d\bar{\Gamma}^{\text{el}}}{d^2 \vec{q}} = g^2 T^* \frac{m_D^2}{\vec{q}^2(\vec{q}^2 + m_D^2)} \quad (21)$$

at leading order [52].

Self-consistent solutions to Eq. (19) can be efficiently constructed in impact parameter space, i.e., by performing a Fourier transformation with respect to \vec{p}_b (see e.g., [63]), where the effects of multiple elastic scatterings during a single emission/absorption can be resummed. Since the effective inelastic rates depend on the kinematic variables p, z as well as the time dependent medium parameters $T^*(t), m_D^2(t), m_{Q_f}^2(t)$, in practice we tabulate the rates as a function of p, z for different values of $T^*, m_D^2, m_{Q_f}^2$ around their momentary values $T^*(t), m_D^2(t), m_{Q_f}^2(t)$, such that for small variations $T^*, m_D^2, m_{Q_f}^2$ which occur in every time step we interpolate between neighboring points, whereas for larger variations of $T^*, m_D^2, m_{Q_f}^2$ which occur over the course of many time steps the entire database gets updated. Similar to the elastic scattering processes, the discretized versions $C_a^{1 \leftrightarrow 2}[n](i_p, j_\phi, k_\phi, t)$ of the inelastic collision integrals in Eq. (16) are then calculated using a Monte Carlo sampling, as described in more detail in Appendix B 2.

Even though we will always employ Eq. (19) to calculate the effective inelastic rates in our numerical studies, it proves insightful to briefly consider the two limiting cases

where the formation time $t_{\text{form}} \sim 1/\delta E_{(p,z)}(\vec{p}_b)$ of the splitting is small or large compared to the inverse of the (small angle) elastic scattering rate $1/\Gamma_{el} \sim 1/(g^2 T^*)$ and closed analytic expressions for the effective inelastic rates can be obtained. We first consider the limit of small formation times, commonly referred to as the Bethe-Heitler regime [64], where radiative emissions/adsorptions

are induced by a single elastic scattering and Eq. (19) can be solved perturbatively (see e.g., [32]), yielding

$$\left. \frac{d\Gamma_{bc}^a}{dz} \right|_{\text{BH}}(p, z) = 2\alpha_s P_{bc}^a(z) g^2 T^* \mathcal{I}_{bc}^{a,\text{BH}}(z), \quad (22)$$

where

$$\begin{aligned} \mathcal{I}_{bc}^{a,\text{BH}}(z) = & \int \frac{d^2 \vec{p}_b}{(2\pi)^2} \int \frac{d^2 \vec{q}}{(2\pi)^2} \frac{m_D^2}{\vec{q}^2 (\vec{q}^2 + m_D^2)} \frac{\vec{p}_b}{\vec{p}_b^2 + \mu_{bc}^a(z)} \\ & \times \left\{ (C_b^R + C_c^R - C_a^R) \left[\frac{\vec{p}_b}{\vec{p}_b^2 + \mu_{bc}^a(z)} - \frac{\vec{p}_b - \vec{q}}{(\vec{p}_b - \vec{q})^2 + \mu_{bc}^a(z)} \right] + (C_c^R + C_a^R - C_b^R) \left[\frac{\vec{p}_b}{\vec{p}_b^2 + \mu_{bc}^a(z)} - \frac{\vec{p}_b - z\vec{q}}{(\vec{p}_b - z\vec{q})^2 + \mu_{bc}^a(z)} \right] \right. \\ & \left. + (C_a^R + C_b^R - C_c^R) \left[\frac{\vec{p}_b}{\vec{p}_b^2 + \mu_{bc}^a(z)} - \frac{\vec{p}_b - \bar{z}\vec{q}}{(\vec{p}_b - \bar{z}\vec{q})^2 + \mu_{bc}^a(z)} \right] \right\}, \quad (23) \end{aligned}$$

with $\mu_{bc}^a(z) = (1-z)m_{\infty,b}^2 + zm_{\infty,c}^2 - z(1-z)m_{\infty,a}^2$, such that the effective inelastic rate is essentially determined by the small angle elastic scattering rate ($\sim g^2 T^*$).

Since the typical transverse momentum acquired in a single scattering is $\vec{p}_b^2 \sim m_D^2$, the validity of this approximation requires the formation time $t_{\text{form}} \sim \frac{2pz(1-z)}{m_D^2}$ to be small compared to the mean free time between small angle scatterings $t_{\text{mfp}} \sim \Gamma_{el}^{-1} \sim 1/g^2 T^*$, giving rise to a characteristic energy scale $\omega_{\text{BH}} = \frac{m_D^2}{g^2 T^*}$ such that for $2pz(1-z) \lesssim \omega_{\text{BH}}$ radiative emissions/adsorptions typically occur due to a single elastic scattering. Conversely, for $2pz(1-z) \gtrsim \omega_{\text{BH}}$ the radiative emission/adsorption occurs coherently over the course of many elastic scatterings, leading to the famous Landau-Pomeranchuk-Migdal suppression [56–58] of the effective inelastic interaction rate. Specifically, in the high-energy limit $2pz(1-z) \gg \omega_{\text{BH}}$, the effective rate can be approximated as [32,59,65]

$$\begin{aligned} \left. \frac{d\Gamma_{bc}^a}{dz} \right|_{\text{HO}}(p, z) \\ = \frac{\alpha_s}{2\pi} P_{bc}^a(z) \sqrt{\frac{\hat{q}}{p}} \sqrt{\frac{zC_c^R + (1-z)C_b^R - z(1-z)C_a^R}{z(1-z)}}, \quad (24) \end{aligned}$$

with $\hat{q} = g^2 T^* \frac{m_D^2}{2\pi}$, where in contrast to Eq. (22) the effective rate is determined by the formation time $t_{\text{form}}^{-1} \sim \sqrt{\frac{\hat{q}}{2pz(1-z)}}$ of the splitting/merging rather than the elastic scattering rate.

III. CHEMICAL EQUILIBRATION OF NEAR-EQUILIBRIUM SYSTEMS

Before we address kinetic and chemical equilibration of non-Abelian plasmas which are initially far-from equilibrium, we will address the conceptually simpler case of studying the

chemical equilibration of systems, where initially there is only one species of particles present. While it is conceivable that such a kind of states could be created in a cosmological environment, whenever the QCD sector is selectively populated via the coupling to e.g., the standard model Higgs or other beyond the standard model (BSM) particles, our primary goal is to understand and characterize the dynamics underlying chemical equilibration of the QGP, and we do not claim relevance to any particular physics application. We will for simplicity assume that, e.g., due to the interaction with other non-QCD particles, the particle species that is present initially is already in thermal equilibrium at a given temperature T_0 and chemical potential μ_0 , such that over the course of the chemical equilibration process the energy of the dominant species needs to be redistributed among all QCD degrees of freedom, until eventually the final equilibrium state with a different temperature T_{eq} and chemical potential μ_{eq} is reached.

Since the leading order kinetic description of massless QCD degrees of freedom is manifestly scale invariant, we can express the relevant momentum and timescales in terms of an arbitrary chosen unit. Naturally, for this kind of investigation, we will express our results in terms of the final equilibrium temperature T_{eq} and chemical potential μ_{eq} , such that the corresponding estimates of the physical timescales can be obtained by evaluating the expressions for the relevant temperatures and densities. Even though we employ a leading order weak-coupling description, we will investigate the behavior for different values of the QCD coupling strength,² typically denoted by the 't Hooft

²While for pure Yang-Mills theory, one can show that the results do not separately depend on g and N_c , but only on the combination $g^2 N_c$ [54]. In non-Abelian gauge theories with fundamental fermions, the general dependence on the gauge coupling g , the number of colors N_c and the number of flavors N_f are more complicated and we only consider the case $N_c = 3$ and $N_f = 3$ relevant to QCD at currently available collider energies.

coupling $\lambda = g^2 N_c$, and frequently express the dependence on the coupling strength in terms of macroscopic quantities, such as the shear-viscosity to entropy density ratio $\eta/s \sim 1/g^4$ [26,27].

A. Chemical equilibration at zero density

We first consider the case of chemical equilibration at zero (net-) density of the conserved u , d , s charges, where the systems feature equivalent numbers of quarks and antiquarks, resulting in zero chemical potentials for all quark flavors. We distinguish two cases, where in the first case the system initially features a thermal distribution of gluons, without any quarks or antiquarks present at the initial time, whereas in the second case the system is initially described by the same distribution of quarks/antiquarks for all flavors, without gluons present in the system. Specifically, for the first case with thermal gluons only, we have

$$\begin{aligned} f_g(p, t=0) &= \frac{1}{e^{p/T_0} - 1}, \\ f_{q_f}(p, t=0) &= 0, \\ f_{\bar{q}_f}(p, t=0) &= 0, \end{aligned} \quad (25)$$

where due to energy conservation, the initial parameter T_0 can be related to thermal equilibrium temperature T_{eq} by $\nu_g \frac{\pi^2}{30} T_0^4 = (4\nu_g + 7\nu_q N_f) \frac{\pi^2}{120} T_{\text{eq}}^4$ according to Eq. (2). Similarly, for the second case where only quarks/antiquarks are initially present in the system, we have

$$\begin{aligned} f_g(p, t=0) &= 0, \\ f_{q_f}(p, t=0) &= \frac{1}{e^{p/T_0} + 1}, \\ f_{\bar{q}_f}(p, t=0) &= \frac{1}{e^{p/T_0} + 1}, \end{aligned} \quad (26)$$

and the initial parameter T_0 has the following relation to final equilibrium temperature T_{eq} by $\nu_q N_f \frac{7\pi^2}{120} T_0^4 = (4\nu_g + 7\nu_q N_f) \frac{\pi^2}{120} T_{\text{eq}}^4$ according to Eq. (2).

Since the final equilibrium temperature T_{eq} is a constant scale, it is then natural to express other scales in terms of T_{eq} , or alternatively in terms of their corresponding equilibrium values, such as $m_D^2(T_{\text{eq}}), m_Q^2(T_{\text{eq}}), \dots$. Besides providing a reference scale for static equilibrium quantities, the inverse of the equilibrium temperature $\sim \frac{1}{T_{\text{eq}}}$ also provides a natural timescale for the evolution of the system, and it is convenient to express the time evolution in units of the near-equilibrium kinetic relaxation time

$$\tau_R = \frac{4\pi\eta/s}{T_{\text{eq}}}, \quad (27)$$

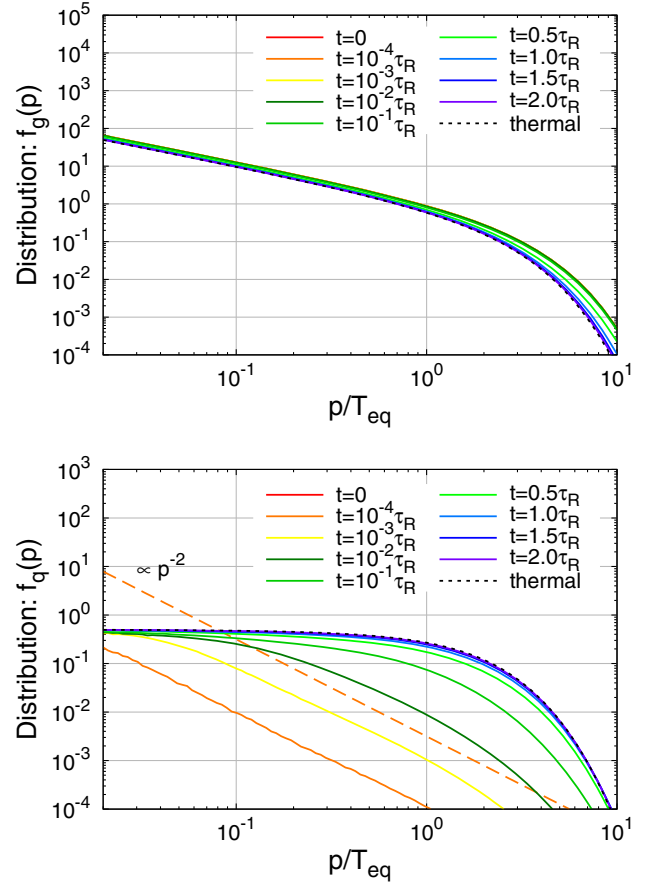


FIG. 1. Evolution of gluon $f_g(t, p)$ and quark $f_q(t, p)$ distribution for *gluon dominated initial conditions* ($\lambda = 1$) at different times $0 \leq t \leq 2\tau_R$ expressed in units of the equilibrium relaxation time τ_R in Eq. (27). Spectra of antiquarks $f_{\bar{q}}(t, p)$ are identical to the spectra of quarks $f_{\bar{q}}(p)$ at zero density and not depicted in the figure.

where η/s is the constant shear viscosity to entropy density ratios, with $\eta/s \simeq 1900, 35, 1$ for 't Hooft couplings $\lambda = g^2 N_c = 4\pi\alpha_s N_c = 0.1, 1, 10$ [50].³

1. Spectra evolution

We first investigate the evolution of the phase-space distribution of quarks and gluons over the course of the chemical equilibration of the QGP. We present our results in Figs. 1 and 2, where we depict the evolution of the spectra of quarks and gluons for initially gluon (Fig. 1) and quark (Fig. 2) dominated systems.

Starting with the evolution of the gluon dominated system in Fig. 1, one observes that the gluon spectrum only varies modestly over the course of the chemical

³We have performed independent extractions of η/s within our implementation of QCD kinetic theory, which—as discussed in Sec. V—agree with the results previously obtained by Kurkela and Mazeliauskas in [50].

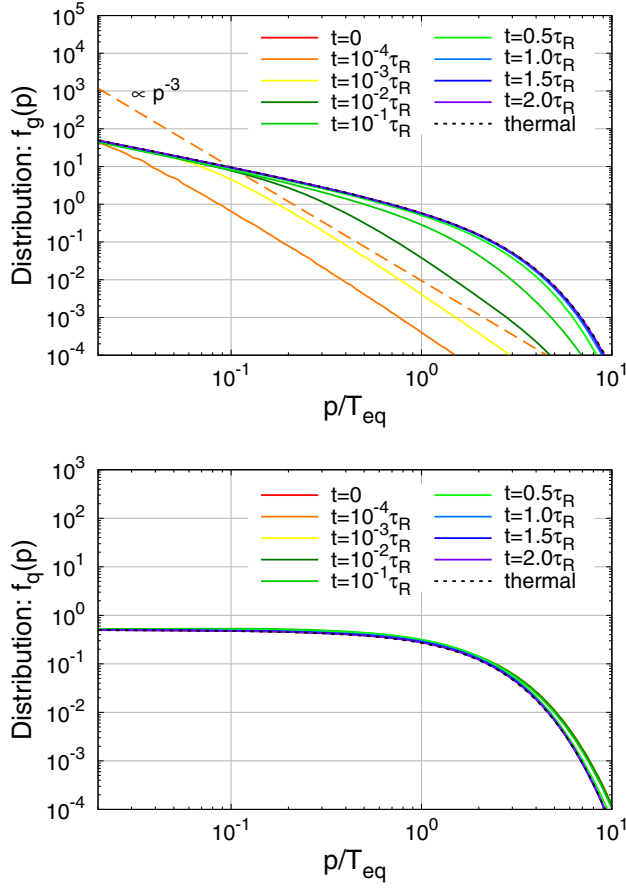


FIG. 2. Evolution of gluon $f_g(t, p)$ and quark $f_q(t, p)$ distribution for *quark/antiquark dominated initial conditions* ($\lambda = 1$) at different times $0 \leq t \leq 2\tau_R$ expressed in units of the equilibrium relaxation time τ_R in Eq. (27). Spectra of antiquarks $f_{\bar{q}}(t, p)$ are identical to the spectra of quarks $f_q(p)$ at zero density and not depicted in the figure.

equilibration of the system, such that throughout the evolution the spectrum can be rather well described by an effectively thermal distribution $f_g(\vec{p}, t) \simeq \frac{1}{\exp(p/T_g(t))-1}$, with a time dependent temperature $T_g(t)$, decreasing monotonically from the initial value $T_g(t=0) = T_0$ to the final equilibrium temperature $T_g(t \rightarrow \infty) = T_{\text{eq}}$. Due to soft gluon splittings $g \rightarrow q\bar{q}$ and elastic quark/gluon conversion $gg \rightarrow q\bar{q}$, the quark/antiquark spectra quickly built up at soft scales $p \lesssim T_{\text{eq}}$, as can be seen from the spectra at early times ($t \ll \tau_R$) in the bottom panel of Fig. 1. The quark/antiquark follows a power-law spectrum $f_{q/\bar{q}}(\vec{p}, t) \propto 1/p^2$ associated with the Bethe-Heitler spectrum. While the production of quark/antiquark at low momentum continues throughout the early stages of the evolution, the momentum of previously produced quarks/antiquarks increases due to elastic interactions, primarily $qg \leftrightarrow qg$ and $\bar{q}g \leftrightarrow \bar{q}g$ scattering, such that by the time $t \simeq 0.5\tau_R$ the spectrum of produced quarks/antiquarks extends all the way to the temperature scale $p \sim T_{\text{eq}}$ and eventually approaches

equilibrium on a timescale on the order one to two times the kinetic relaxation time τ_R .

Similar behavior can be observed for the quark/antiquark dominated scenario, which is depicted in Fig. 2. While quarks/antiquarks feature approximately thermal spectra $f_{q/\bar{q}}(\vec{p}, t) \simeq \frac{1}{\exp(p/T_q(t))+1}$, gluons are initially produced at low momentum mainly due to the emission of soft gluon radiation $q \rightarrow qg$, which at early times ($t \ll \tau_R$) gives rise to a power-law spectrum $f_g(\vec{p}, t) \propto 1/p^3$ associated with the Bethe-Heitler spectrum. Subsequently, elastic and inelastic processes lead to a production of gluons with momenta $p \sim T_{\text{eq}}$ until the system approaches equilibrium on a timescale on the order of the kinetic relaxation time τ_R .

2. Collision rates

While the evolution of the spectra in Figs. 1 and 2 provides an overview over the chemical equilibration process, we will now investigate how the individual QCD processes contribute to the evolution of the gluon and quark/antiquark spectra in Figs. 1 and 2. We provide a compact summary of our findings in Figs. 3 and 4, where we present the result for the collision rates

$$r_g = \frac{\nu_g}{\lambda^2 T_{\text{eq}}^3} p^2 C_g[f], \quad r_{q/\bar{q}} = \frac{N_f \nu_q}{\lambda^2 T_{\text{eq}}^3} p^2 C_{q/\bar{q}}[f] \quad (28)$$

for initially gluon dominated (Fig. 3) and initially quark dominated scenarios (Fig. 4). Different columns in Figs. 3 and 4 show the collision rates of individual processes at the initial time $t = 0$, at an intermediate time $t = 0.1\tau_R$ and near equilibrium at time $t = 0.5\tau_R$. We note that due to the zero net-density of u, d, s quarks, the quark and antiquark collision rates in Figs. 3 and 4 are identical and briefly remind the reader that according to our convention in Eq. (6), positive contributions to the collision rate represent a number loss and negative collision rates exhibit a number gain for the specific particle.

a. Gluon dominated scenario.—Starting with the collision rates for the gluon dominated scenario in Fig. 3, one observes that at initial time $t = 0$, the gluon splitting process $g \rightarrow q\bar{q}$ shown by the dark blue curve is dominating the production of quarks/antiquarks. By comparing the collision rates for quarks and gluons, one finds that gluons with momenta $p \simeq 1-2T_{\text{eq}}$ copiously produce soft quarks/antiquarks at low momenta $p \ll T_{\text{eq}}$. Since the individual splittings are typically asymmetric with $z(1-z) \ll 1$, the energy of thermal gluons is redistributed to soft quarks/antiquarks, and the splittings fall into the Bethe-Heitler regime as typically $pz(1-z) \lesssim \omega_{\text{BH}} \sim T_{\text{eq}}$. In addition to the inelastic splitting, elastic conversion processes $gg \rightarrow q\bar{q}$ shown as a lime curve evenly redistribute the energy of gluons with momenta $p \simeq T_{\text{eq}}$ into quarks/antiquarks at an intermediate scale $p \simeq T_{\text{eq}}$. Due to the absence of quarks

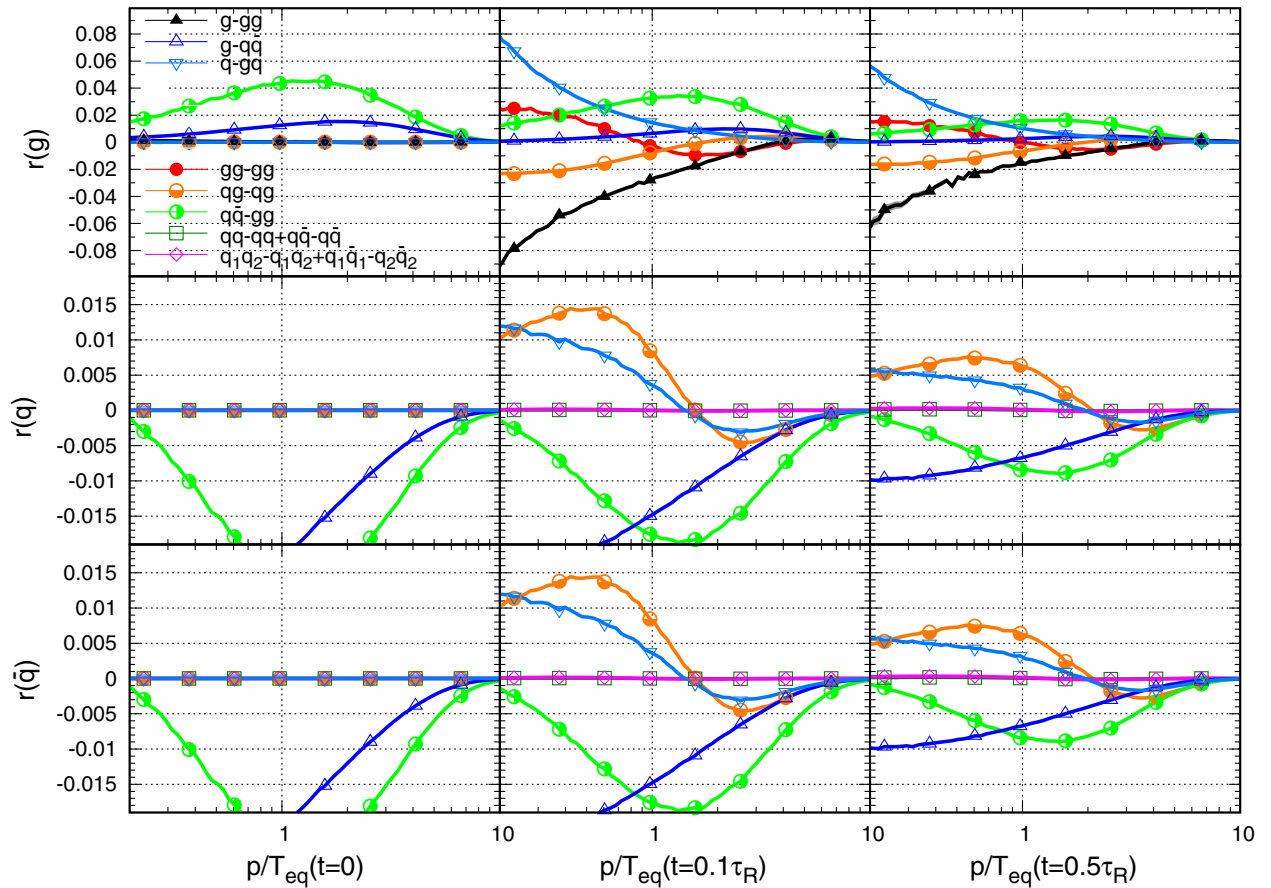


FIG. 3. Collision rates r for gluons (upper), quarks (middle), and antiquarks (lower) defined in Eq. (28) for *gluon dominated initial conditions* at initial time $t = 0$ (left), at intermediate time $t = 0.1\tau_R$ (middle), and during the approach toward equilibrium $t = 0.5\tau_R$ (right).

and antiquarks at initial time, the contributions of all other processes involving quarks/antiquarks in the initial state vanish identically at initial time, as do the collision rates for processes involving only gluons due to the detailed balance in the gluon sector.

Subsequently, as quarks/antiquarks are produced at low momenta, additional scattering processes involving quarks/antiquarks in the initial state become increasingly important, as can be seen from the second column of Fig. 3, where we present the collision rates at $t = 0.1\tau_R$. While the rate of the initial quark/antiquark production processes $g \rightarrow q\bar{q}$, $gg \rightarrow q\bar{q}$ decrease, as the corresponding inverse processes $q\bar{q} \rightarrow g$, $q\bar{q} \rightarrow gg$ start to become important, elastic scattering of quarks and gluons $qg \rightarrow qg$ (orange curve) and gluon absorption $gq \rightarrow q$ (light blue curve) become of comparable importance. Specifically, in each of these processes, the previously produced quarks/antiquarks at low momentum $p \ll T_{\text{eq}}$ gain energy via elastic scattering or absorption of gluons, resulting in an increase of the spectrum for $p \gtrsim 1.5T_{\text{eq}}$. By inspecting the collision rates for gluons in the top panel of Fig. 3, one observes that the depletion of soft gluons ($p \ll T_{\text{eq}}$) due to gluon absorption

by quarks $gq \rightarrow q$ is primarily compensated by the emission of soft gluon radiation due to the $g \rightarrow gg$ process (black curve). Beside the aforementioned process, the elastic scattering of gluons $gg \rightarrow gg$ (red curve) also plays an equally important role in redistributing energy among gluons, clearly indicating that over the course of the chemical equilibration process the gluon distribution also falls out of kinetic equilibrium.

Eventually, the chemical equilibration process proceeds in essentially the same way, until close to equilibrium the collision rates of all processes decrease as the corresponding inverse processes start to become of equal importance, as seen in the right column of Fig. 3 where we present the collision rates at $t = 0.5\tau_R$. By the time $t \simeq 2\tau_R$, which is no longer shown in Fig. 3, all the collision rates decrease by at least 1 order of magnitude as the system gradually approaches the detailed, balanced chemical and kinetic equilibrium state.

b. Quark/antiquark dominated scenario.—Next we will analyze the collision rates in the quark/antiquark dominated scenario shown in Fig. 4 and compare the underlying dynamics to the gluon dominated scenario in Fig. 3.

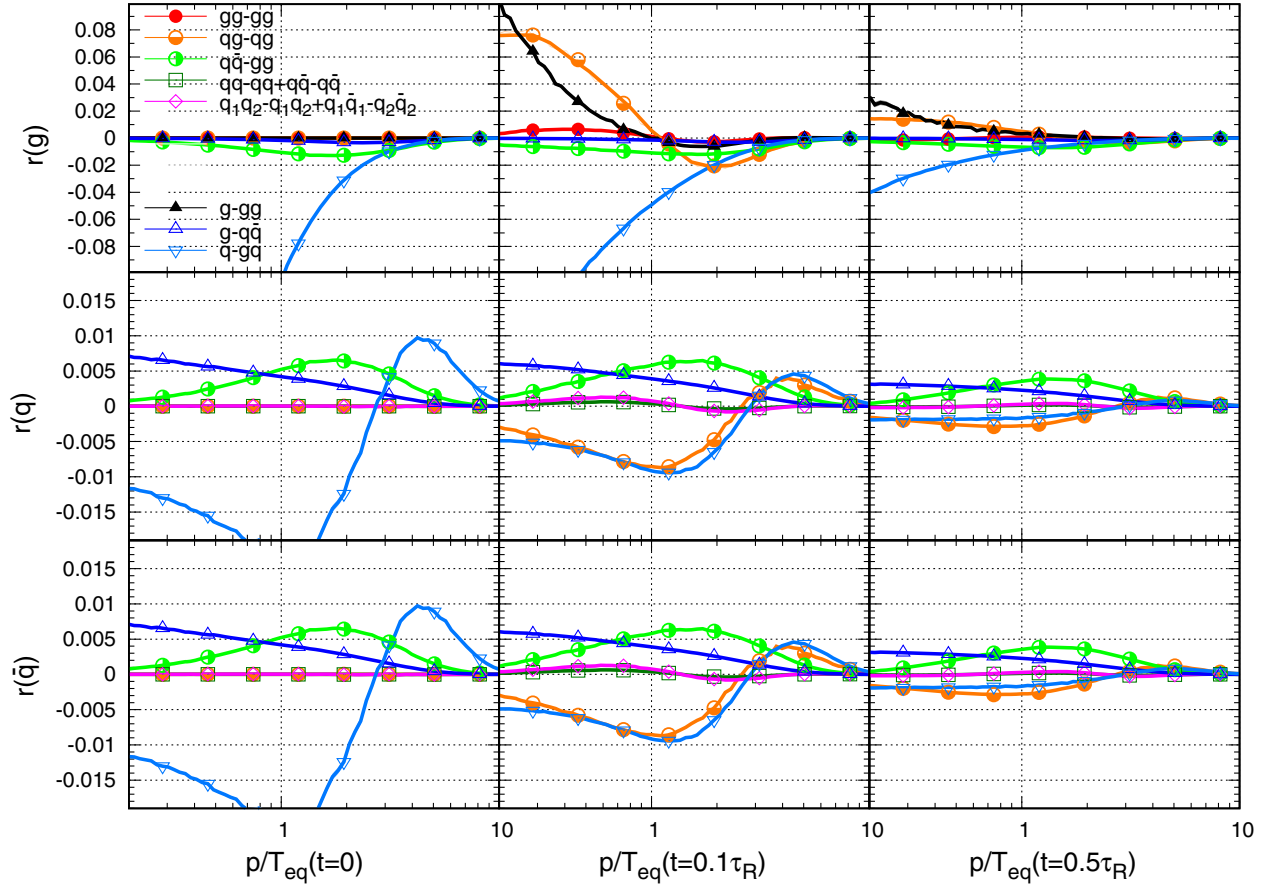


FIG. 4. Collision rates r for gluons (upper), quarks (middle), and antiquarks (lower) defined in Eq. (28) for *quark/antiquark dominated initial conditions* at initial time $t = 0$ (left), at intermediate time $t = 0.1\tau_R$ (middle), and during the approach toward equilibrium $t = 0.5\tau_R$ (right).

Starting from the collision rates at the initial time shown again in the left panel, one finds that in addition to quark/antiquark annihilation via elastic $q\bar{q} \rightarrow gg$ (lime) and inelastic $q\bar{q} \rightarrow g$ (dark blue) processes, soft gluons are copiously produced by $q \rightarrow gq$ Bremsstrahlungs processes initiated by hard quarks/antiquarks with momenta $p \gtrsim 3T_{\text{eq}}$. Notably the $q \rightarrow gq$ process also leads to the redistribution of the energy of quarks/antiquarks from momenta $p \gtrsim 3T_{\text{eq}}$, to lower momenta $p \lesssim 3T_{\text{eq}}$; however, the negative collision rate for the $q \rightarrow gq$ process partially cancels against the positive contribution from $q\bar{q} \rightarrow g$ processes, such that there is effectively no increase/decrease of the quark/antiquark distributions at very low momenta $p \ll T_{\text{eq}}$. Similar to the processes involving only gluons at $t = 0$ in Fig. 3, processes involving only quarks and antiquarks (green, pink) in Fig. 4 vanish identically at $t = 0$ due to cancellations of gain and loss terms in the statistical factor, while other processes $gg \rightarrow gg$, $qg \rightarrow qg$, $g \rightarrow gg$ are exactly zero due to the absence of gluons in the initial state. By comparing the collision integrals for quarks and gluons in Figs. 3 and 4, one also observes that inelastic processes are initially much more dominant for the

quark/antiquark dominated scenario in Fig. 3 as compared to the gluon dominated scenario in Fig. 4.

Similar to the evolution in the gluon dominated scenario, the energy of the soft gluons produced in the previous stage increases through successive elastic and inelastic interactions, as can be seen from the middle column of Fig. 4, where we present the collision rates at the intermediate time $t = 0.1\tau_R$ for the quark dominated case. By inspecting the collision rates for gluon in more detail, one finds that quark-gluon scattering $qg \rightarrow qg$ (orange) as well as $gg \rightarrow g$ (black) are the dominant processes that increase the number of hard $p \gtrsim T_{\text{eq}}$ gluons. Elastic scattering between gluons $gg \rightarrow gg$ (red) plays a less prominent role for the evolution of the gluons, as do elastic (green) $q\bar{q} \rightarrow gg$ and inelastic (dark-blue) $q\bar{q} \rightarrow g$ conversions. With regards to the collision rates for quarks and antiquarks, one finds that elastic $q\bar{q} \rightarrow gg$ (lime) and inelastic $q\bar{q} \rightarrow g$ (dark blue) annihilation processes as well as $q \rightarrow gq$ Bremsstrahlung processes continue to deplete the number of hard quarks/antiquarks. However at this stage of the evolution, $qg \rightarrow qg$ scattering processes (orange) also lead to an efficient energy transfer from quarks to gluons, depleting the

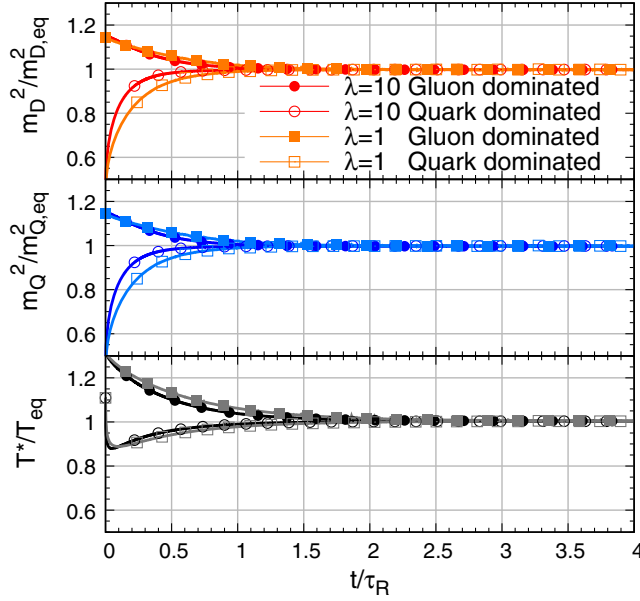


FIG. 5. Evolution of the characteristic scales $m_D^2(t)$ (red), $m_Q^2(t)$ (blue), and $T^*(t)$ (black) during the chemical equilibration process for the quark dominated (open symbol) and gluon dominated (closed symbol) scenarios at two different coupling strengths $\lambda = 1$ (lighter color/square) and $\lambda = 10$ (darker color/circle). Scales are normalized to their respective equilibrium values, while the evolution time t is normalized to the equilibrium relaxation time τ_R in Eq. (27) in order to take into account the leading coupling dependence.

number of hard quarks $p \gtrsim 2T_{\text{eq}}$ in the system. While the nonvanishing quark/antiquark scattering rates (green, pink) reveal slight deviations of quark/antiquark spectra from kinetic equilibrium, these processes clearly have a sub-leading effect.

Subsequently, the evolution continues along the same lines as illustrated in the right column for $t = 0.5\tau_R$, with the collision rates of all processes decreasing as the system approaches kinetic and chemical equilibrium.

3. Scale evolution

Beyond the characterization of the microscopic processes in terms of spectra and collision rates, it is instructive to investigate the evolution of the characteristic scales m_D^2 , m_Q^2 , and T^* defined in Sec. II A, which further provides a compact way to compare the timescales of the chemical equilibration process at different coupling strengths. Corresponding results are presented in Fig. 5, where we compare the evolution of the various scales for quark and gluon dominated initial conditions at two different coupling strengths $\lambda = 1, 10$. By taking into account the corresponding change in the equilibrium relaxation rate τ_R [cf. Eq. (27)], one finds that the time evolution of the various scales are quite similar, and rather insensitive to the coupling strength, such that by the time $t = 1 \sim 2\tau_R$ all

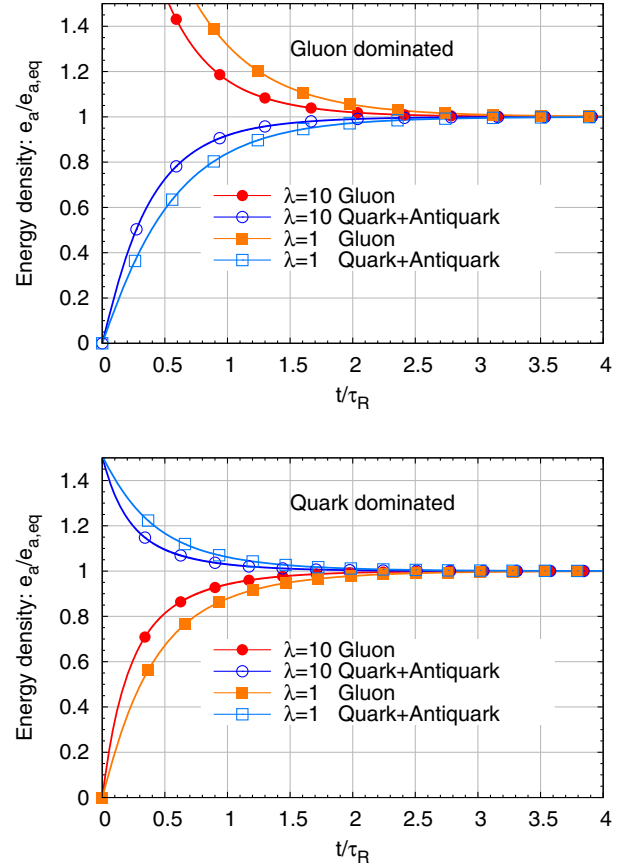


FIG. 6. Evolution of the energy densities of gluons e_g (red/closed symbols) and quarks plus antiquarks $\sum_f e_{q_f} + e_{\bar{q}_f}$ (blue/open symbols) for the quark dominated (bottom) and gluon dominated (top) scenarios at different coupling strengths $\lambda = 10$ (darker color/circle) and $\lambda = 1$ (lighter color/square). Energies of each species are normalized to their equilibrium values, while the evolution time t is normalized to the equilibrium relaxation time τ_R in Eq. (27) in order to take into account the leading coupling dependence.

relevant dynamical scales are within a few percent of their equilibrium values.

During the earlier stages, $t \lesssim \tau_R$, some interesting patterns emerge in the evolution of m_D^2 , m_Q^2 , and T^* , which can be readily understood from considering the evolution of the spectra in Figs. 1 and 2, along with different effects that quarks and gluons have on each of these quantities. Since the occupancy of soft quarks is always limited to below unity, soft gluons contribute more significantly to in-medium screening, such that in the gluon dominated case the screening masses m_D^2 and m_Q^2 in Fig. 5 decrease monotonically, whereas in the quark dominated case one observes a monotonic increase of the same quantities. The effective temperature T^* which characterizes the strength of elastic interactions inside the medium, drops throughout the chemical equilibration process for the gluon dominated case, whereas for quark dominated initial conditions, the

evolution of T^* shows a nonmonotonic behavior featuring a rapid initial drop followed by a gradual increase of T^* toward its equilibrium value. By careful inspection of the spectra in Fig. 2, one finds that this rather subtle effect should be attributed to the effects of Bose enhancement and Fermi suppression in the determination of T^* .

Besides the evolution of the characteristic scales m_D^2 , m_Q^2 , and T^* , it is also important to understand how the overall energy is shared and transferred between quark and gluon degrees of freedom over the course of the evolution. A compact overview of the energy transfer during the chemical equilibration process is provided in Fig. 6, where we show the evolution of the energy density of gluons as well as quarks and antiquarks for the two scenarios. Starting from a rapid energy transfer at early times, the flattening of the individual energy densities toward later times eventually indicates the approach toward chemical equilibrium. Even though the evaluation of an exact chemical equilibration time depends on the quantitative criterion for how close the energy densities (or other scales) are compared with what their equilibrium values are, the figures still speak for themselves indicating the occurrence of chemical equilibration roughly at the same timescale as kinetic equilibration, with

$$t_{\text{chem}}^{\text{eq}} \simeq t_{\text{kin}}^{\text{eq}} \simeq 1 - 2 \times \frac{4\pi\eta/s}{T_{\text{eq}}}, \quad (29)$$

subject to mild variations for the two different coupling strengths.

B. Chemical equilibration of finite density systems

So far we have investigated the chemical equilibration of charge neutral QCD plasmas, and we will now proceed to study the chemical equilibration process of QCD plasmas at finite density of the conserved u , d , s charges, featuring an excess of quarks to antiquarks (or vice versa). Since a finite net charge density of the system can only be realized in the presence of quarks/antiquarks, we will focus on quark dominated initial conditions and modify the corresponding initial conditions as

$$\begin{aligned} f_g(p, t=0) &= 0, \\ f_{q_f}(p, t=0) &= \frac{1}{e^{(p-\mu_f)/T_0} + 1}, \\ f_{\bar{q}_f}(p, t=0) &= \frac{1}{e^{(p+\mu_f)/T_0} + 1}, \end{aligned} \quad (30)$$

where for simplicity, we consider equal densities of u , d , and s quarks. Similar to Eqs. (25) and (26), the initial parameters T_0 and μ_0 can be related to corresponding equilibrium temperature T_{eq} , and equilibrium chemical potential μ_{eq} via the Landau matching procedure in Eq. (2). Due to energy and charge conservation, T_{eq} and

μ_{eq} , then determine the final equilibrium state of the system, and we will characterize the different amounts of net charge in the system in terms of the ratio $\mu_{\text{eq}}/T_{\text{eq}}$, with $\mu_{\text{eq}}/T_{\text{eq}} = 0$ corresponding to the charge neutral plasma considered in the previous section.

When comparing the evolution at different coupling strengths, we follow the same procedure as discussed above and express the evolution time in units of the kinetic relaxation time

$$\tau_R(T, \mu) = \frac{4\pi}{T_{\text{eff}}} \left(\frac{\eta(T, \mu) T_{\text{eff}}}{e+p} \right)^{\mu=0} \frac{4\pi\eta/s}{T_{\text{eq}}}, \quad (31)$$

which in accordance with the last equality reduces to the same expression for a charge neutral system ($\mu = 0$) in Eq. (27). The effective temperature is evaluated as $T_{\text{eff}} = \left(\frac{30e}{\pi^2 \nu_{\text{eff}}} \right)^{\frac{1}{4}}$ with effective degree of freedom $\nu_{\text{eff}} = \nu_G + \frac{7}{4} \nu_Q N_f$, such that $T_{\text{eff}} \xrightarrow{\mu=0} T_{\text{eq}}$. Since we did not explicitly determine the dependence of the shear-viscosity $\eta(T, \mu)$ on the chemical potential μ for all coupling strengths λ , we will approximate $\frac{\eta(T, \mu) T}{e+p} \approx \frac{\eta(T, \mu) T}{e+p} \Big|_{\mu=0}$ by the corresponding value of $\frac{\eta(T, \mu) T}{e+p} \Big|_{\mu=0} = \frac{\eta}{s}$ at vanishing density of the conserved charges, which are quoted below Eq. (27).

1. Spectra evolution

We follow the same logic as in the charge neutral case and first investigate the evolution of the spectra of quarks, antiquarks, and gluons, which is presented in Fig. 7 for the chemical equilibration of a system with quark chemical potentials $\mu_{\text{eq}}/T_{\text{eq}} = 2.5$. Similar to the quark dominated scenario at zero density, we find that the spectra for quarks and antiquarks are always close to a thermal distribution with the expected moderate deviation at intermediate times. Specifically, the antiquark spectra in the low momentum sector $p \lesssim 0.3T_{\text{eq}}$ are depleted at intermediate times $t \lesssim 0.5\tau_R$, due to elastic $q\bar{q} \rightarrow gg$ and inelastic $q\bar{q} \rightarrow g$ conversions. Besides quark/antiquark annihilations, the radiative emission of gluons due to $q \rightarrow qg$ and $\bar{q} \rightarrow \bar{q}g$ processes leads to a rapid population of the soft gluon sector seen in the top panel of Fig. 7. By comparing the results in Figs. 2 and 7, one finds that the soft gluon sector builds up even more rapidly at finite density as compared to zero density, such that already by the time $t = 10^{-3}\tau_R$, the gluon distribution at low momentum $p \lesssim 0.1T_{\text{eq}}$ features a quasithermal spectrum $f(p \ll T_{\text{eq}}) \simeq T_{\text{eq}}/p$, whereas the high momentum tail is yet to be populated. Eventually on a timescale of $t \simeq 1.5\tau_R$, a sufficiently large number of hard gluons has been produced and the spectra of all particle species relax toward equilibrium, such that significant deviations from the thermal distributions are no longer visible for $t = 1.5\tau_R$ in Fig. 7.

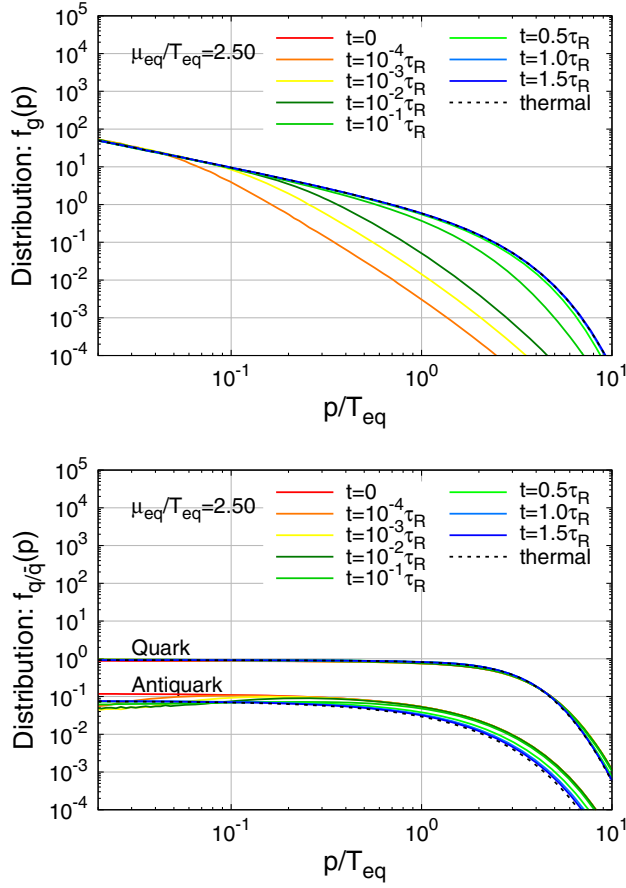


FIG. 7. Evolution of the gluon $f_g(t, p)$, quark $f_q(t, p)$, and antiquark $f_{\bar{q}}(t, p)$ distributions for *quark dominated initial conditions* with large chemical potential $\mu_f/T_{\text{eq}} = 2.5$ at different times $0 \leq t \leq 2\tau_R$ expressed in units of the equilibrium relaxation time τ_R in Eq. (31) for $\lambda = 1$.

2. Collision rates

Beyond the evolution of the spectra, it again proves insightful to investigate the collision rates in Fig. 8 in order to identify the microscopic processes that drive chemical and kinetic equilibration of gluons, quarks, and antiquarks at different stages.

Similar to the results for the charge neutral case in Fig. 4, the initial gluon production in Fig. 8 is still dominated by soft radiation $q \rightarrow gq + \bar{q} \rightarrow \bar{q}g$ (light blue), with even more substantial contributions due to the larger abundances of quarks. Conversely, the gluon production from elastic $q\bar{q} \rightarrow gg$ (lime) and inelastic $q\bar{q} \rightarrow g$ (dark blue) quark/antiquark annihilation processes is markedly suppressed due to the shortage of antiquarks. Similar differences between the evolution at zero and finite density can also be observed in the collision rates for quarks and antiquarks, where in the case of the quark the emission of gluon radiation leads to a depletion of the hard sector $p \gtrsim 3T_{\text{eq}}$, along with an increase of the population of softer quarks with typical momenta $p \sim T_{\text{eq}}$. While elastic

$q\bar{q} \rightarrow gg$ (lime) and inelastic $q\bar{q} \rightarrow g$ (dark blue) processes initially contribute at a much smaller rate, such that the inelastic $q \rightarrow gq$ process dominates the evolution of the quarks, a manifestly different picture emerges for the collision rates of antiquarks. Due to the large abundances of quarks, elastic $q\bar{q} \rightarrow gg$ (lime) and inelastic $q\bar{q} \rightarrow g$ (dark blue) quark/antiquark annihilations initially occur at essentially the same rate as gluon radiation off antiquarks $\bar{q} \rightarrow \bar{q}g$ (light blue), resulting in a net-depletion of the antiquark sector across the entire range of momenta. Besides the aforementioned processes, the collision rates of all other processes vanish identically at the initial time for all particle species due to cancellations of the statistical factors.

Subsequently, for $t = 0.1\tau_R$ depicted in the central column of Fig. 8 a variety of different processes become relevant as soft gluons have been copiously produced during the previous evolution. Besides the processes involving quark-gluon interactions $q \rightarrow gq$ (light blue), $qg \rightarrow qg$ (orange), inelastic absorptions of soft gluons $gq \rightarrow g$ (black) also have an important effect for the thermalization of the gluon sector, whereas elastic scattering of gluons $gg \rightarrow gg$ (red) as well as elastic $q\bar{q} \rightarrow gg$ (lime) and inelastic $q\bar{q} \rightarrow g$ (dark blue) quark/antiquark annihilation processes are clearly subleading. By comparing the results at zero and finite density in Figs. 4 and 8, one further notices an increment of the $gq \rightarrow g$ collision rates, indicating a more rapid gluon production from quarks at finite density, consistent with the observations of the spectra in Figs. 2 and 7. Due to the fact that at finite density there are more quarks present in the system, the collision rates for quarks are generally larger compared to the zero density case. Nevertheless, the underlying dynamics remains essentially the same as compared to the zero density case, with gluon radiation $q \rightarrow gq$ (light blue) and quark-gluon scattering $qg \rightarrow qg$ providing the dominant mechanisms to transfer energy from hard quarks to softer gluons. Due to the larger abundance of quarks at finite density, elastic scattering processes $qq \rightarrow qq$ involving quarks of the same (green) and different flavors (pink), also play a more prominent role in restoring kinetic equilibrium in the quark sector, while they were more or less negligible at zero density. Surprisingly small changes appear in the collision rates for antiquarks between the initial time $t = 0$ and $t = 0.1\tau_R$, where at later times the inelastic $\bar{q} \rightarrow \bar{q}g$ process becomes suppressed due to the fact the inverse process of absorbing a soft gluon $\bar{q}g \rightarrow \bar{q}$ becomes increasingly likely. Similarly, elastic scattering processes $\bar{q}g \rightarrow \bar{q}$ (orange) between antiquarks and gluons also contribute to the energy transfer from the antiquark to the gluon sector.

Eventually for $t = 0.5\tau_R$, the energy transfer from quarks to gluons due to elastic $qg \rightarrow qg$ (orange) and inelastic $q \rightarrow gq$ (light blue) becomes smaller and smaller, and so do the collision rates for inelastic gluon absorptions $g \rightarrow gq$

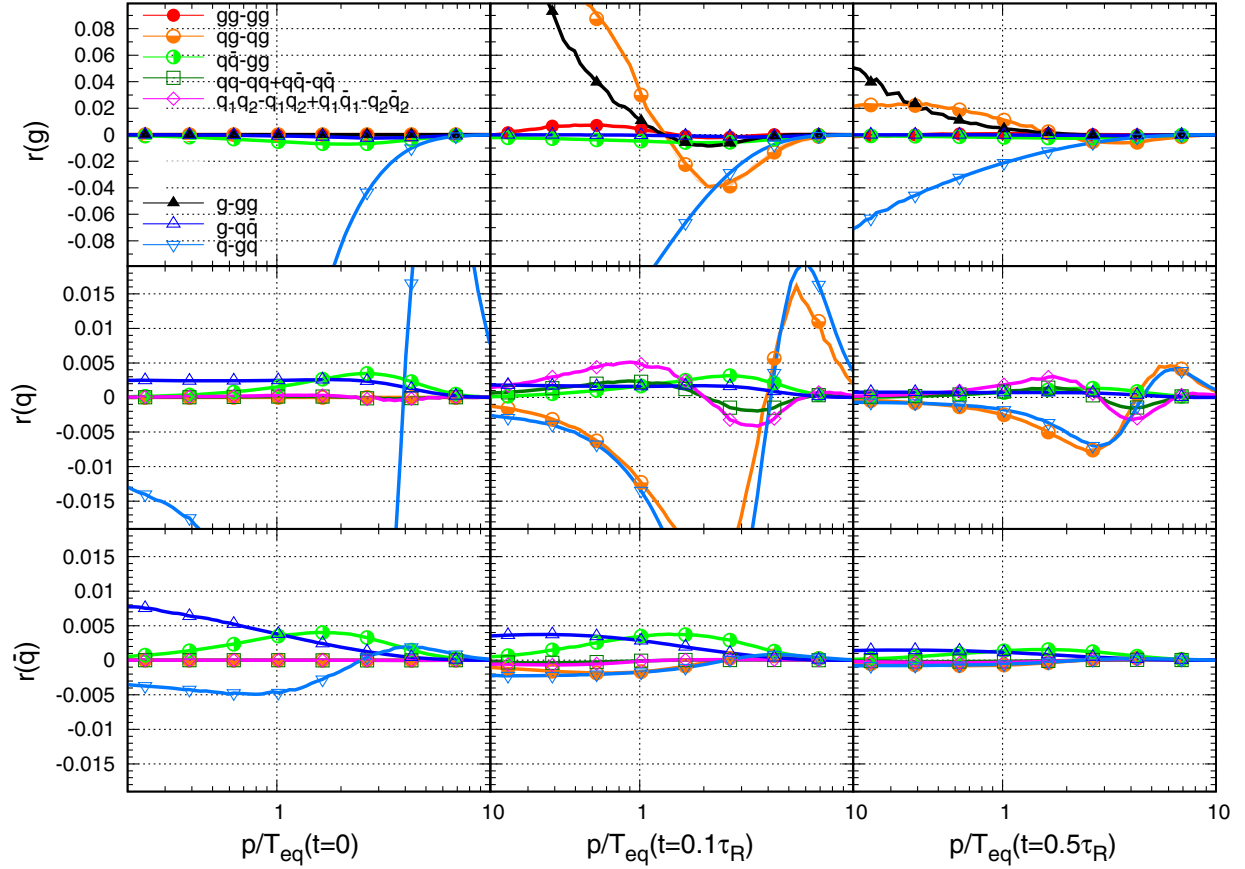


FIG. 8. Collision rates r for gluons (upper), quarks (middle), and antiquarks (lower) defined in Eq. (28) for *quark dominated initial conditions* with large chemical potential $\mu_f/T_{\text{eq}} = 2.5$ at initial time $t = 0$ (left), intermediate time $t = 0.1\tau_R$ (middle), and during the approach toward equilibrium $t = 0.5\tau_R$ (right).

(black) and elastic scatterings between quarks/antiquarks (pink and green), which are primarily responsible for restoring kinetic equilibrium in the gluon and quark sectors. Beyond the timescales shown in Fig. 8, the evolution of the system continues in essentially the same way, with continuously collision rates decreasing until eventually gluons, quarks and antiquarks all approach their respective equilibrium distribution.

3. Scale evolution

Now that we have established the microscopic processes underlying the chemical equilibration of finite density, we again turn to the evolution of the dynamical scales m_D^2 , m_Q^2 , and T^* , which serve as a reference to determine the progress of kinetic and chemical equilibration. We present our results in Fig. 9, where we compare the evolution of the dynamical scales in systems with a different amount of net-charge density, as characterized by the ratio $\mu_{\text{eq}}/T_{\text{eq}} = 0, 0.14, 1.34, 2.5$ of the equilibrium chemical potential over the equilibrium temperature. By comparing the evolution of the various quantities in Fig. 9, one observes that for larger chemical potentials m_D^2 , m_Q^2 as well as T^* are generally

closer to their final equilibrium values over the course of the entire evolution. While the smaller deviations of m_D^2 , m_Q^2 , and T^* can partly be attributed to the fact that in the finite density system the initial values for these quantities are already closer to the final equilibrium value, it also appears that the ultimate approach toward equilibrium occurs on a slightly shorter timescale.

Similar phenomena can also be observed in Fig. 10, where we present the evolution of the energy and number density of gluons, quarks, and antiquarks over the course of the chemical equilibration process at different densities $\mu_{\text{eq}}/T_{\text{eq}} = 0, 0.14, 1.34, 2.5$. While initially there is always a rapid production and energy transfer to the gluon sector, the flattening of the curve at later times shows the relaxation toward chemical equilibrium, which occurs roughly on the same timescale as the kinetic equilibration of the dynamical scales m_D^2 , m_Q^2 , and T^* . By comparing the results for different $\mu_{\text{eq}}/T_{\text{eq}}$, one again observes that the chemical equilibration happens slightly earlier for larger chemical potential, consistent with the observations from spectra in Figs. 2 and 7, from collision rates in Figs. 4 and 8, and from the scale evolution in Fig. 9. Nevertheless,

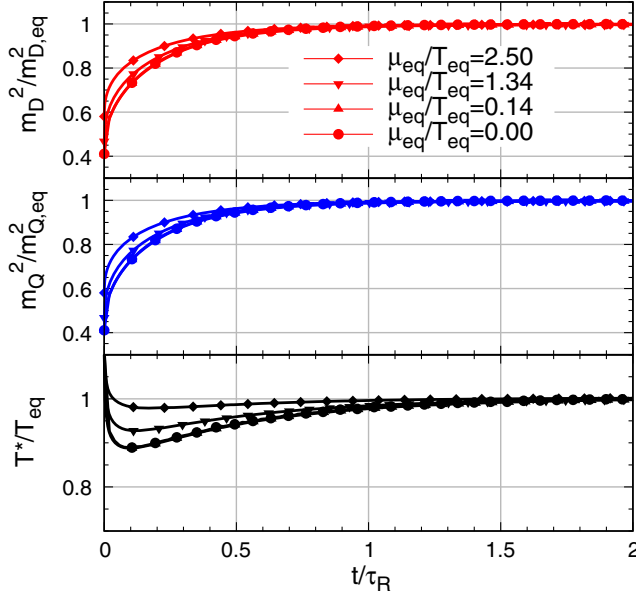


FIG. 9. Evolution of the characteristic scales $m_D^2(t)$ (red), $m_Q^2(t)$ (blue), and $T^*(t)$ (black) during the chemical equilibration process for different chemical potentials $\mu_{\text{eq}}/T_{\text{eq}} = 0, 0.14, 1.34, 2.5$ (circle, triangle, inverted triangle, diamond). Scales are normalized to their respective equilibrium values, while the evolution time t is normalized to the equilibrium relaxation time τ_R in Eq. (31) for $\lambda = 1$.

we believe that at least for the range of $\mu_{\text{eq}}/T_{\text{eq}}$ considered in Fig. 9, our estimate of the kinetic and chemical equilibration timescales in Eq. (29), remains valid also at finite density.

IV. EQUILIBRATION OF FAR-FROM EQUILIBRIUM SYSTEMS

We will now analyze the equilibration process of QCD systems which are initially far-from equilibrium. By focusing on systems which are spatially homogeneous and isotropic in momentum space, we can distinguish two broad classes of far-from equilibrium initial states which following [32,36] can be conveniently characterized by considering the initial average energy per particle $\langle p \rangle_0$ in relation to the equilibrium temperature T_{eq} of the system. Specifically, for far-from equilibrium initial states, we can consider a situation where the average energy per particle is initially much smaller than the equilibrium temperature, i.e., $\langle p \rangle_0 \ll T_{\text{eq}}$, such that the energy is initially carried by a large number $f_0 \gg 1$ of low momentum gluons. Such *overoccupied* initial states typically appear as a consequence of plasma instabilities [36,41,66], and they also bear some resemblance with the saturated “glasma” initial state created in high-energy collisions of heavy nuclei [40,67–72], although the detailed properties of this state are quite different as the system is highly anisotropic and rapidly expanding in the longitudinal direction as

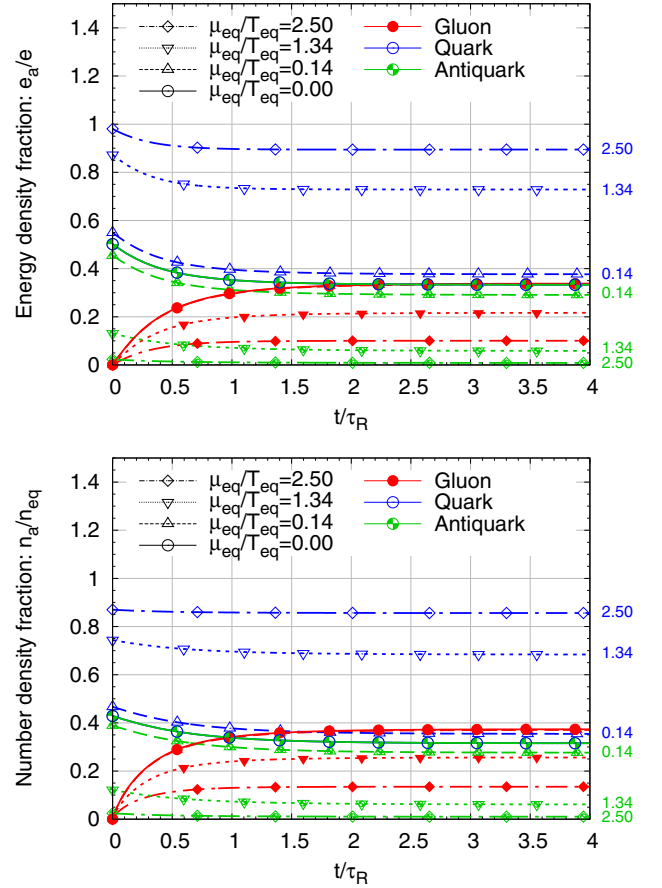


FIG. 10. Evolution of the energy (top) and particle number (bottom) densities of gluons (red/closed symbols), quarks (blue/open symbols), and antiquarks (green/crossed symbols) for various chemical potentials $\mu_{\text{eq}}/T_{\text{eq}} = 0, 0.14, 1.34, 2.5$ (solid/circles, dashed/triangles, dotted/inverted triangles, dotted dashed/diamonds). Energy and particle number densities are normalized to the total equilibrium values e_{eq} and n_{eq} of all species, while the evolution time t is normalized to the equilibrium relaxation time τ_R in Eq. (31) for $\lambda = 1$.

discussed in more detail in Sec. V. While for $\langle p \rangle_0 \sim T_{\text{eq}}$, the system is in some sense close to equilibrium and one would naturally expect kinetic and chemical equilibration to occur on the timescales of the equilibrium relaxation time $\sim \tau_R$, there is a second important class of far-from equilibrium initial states corresponding to *underoccupied* states. In *underoccupied* systems the average energy per particle is initially much larger than the equilibrium temperature $\langle p \rangle_0 \gg T_{\text{eq}}$, such that the energy is initially carried by a small number $f_0 \ll 1$ of highly energetic particles, as is for instance the case for an ensemble of high-energy jets. While earlier works [40,46] have established the equilibration patterns of such systems for pure glue QCD, we provide an extension of these studies to full QCD with three light flavors, as previously done for overoccupied systems in [50].

A. Equilibration of overoccupied systems

We first consider overoccupied systems characterized by a large occupation number $f_0 \gg 1$ of low-energy $\langle p \rangle_0 \ll T_{\text{eq}}$ gluons,⁴ and we may estimate the energy density of the overoccupied system as $e_0 \sim f_0 \langle p \rangle_0^4$. Since the total energy density is conserved, we have $e_{\text{eq}} = e_0$, such that with $e_{\text{eq}} \sim T_{\text{eq}}^4$ the final equilibrium temperature $T_{\text{eq}} \sim f_0^{1/4} \langle p \rangle_0 \gg \langle p \rangle_0$ is much larger than the average initial momentum $\langle p \rangle_0$. Due to this separation of scales, energy needs to be re-distributed from low momentum to high momentum degrees of freedom, which as will be discussed shortly is achieved via a direct energy cascade from the infrared to ultraviolet in momentum space.

1. Theoretical aspects

Due to the large population of low momentum gluons, interaction rates for elastic and inelastic processes are initially strongly enhanced, such that the large angle elastic scattering rate $\Gamma_{\text{el}} \sim g^2 T^* \frac{m_D^2}{\langle p \rangle^2}$ is initially much larger than in equilibrium $\Gamma_{\text{el}}^0 \sim g^4 f_0^2 \langle p \rangle \gg \Gamma_{\text{el}}^{\text{eq}} \sim g^4 T_{\text{eq}}$. Even though the timescale for the actual equilibration process is eventually controlled by the equilibrium rate $\sim 1/\Gamma_{\text{el}}^{\text{eq}}$, the system will therefore encounter a rapid memory loss of the details of the initial conditions on a timescale $\sim 1/\Gamma_{\text{el}}^0$, and subsequently spend a significant amount of time in a transient nonequilibrium state, where the energy transfer from the infrared toward the ultraviolet is accomplished.

Since the dynamics remains gluon dominated with $f_g \gg 1 \geq f_{q,\bar{q}}$ all the way until the system eventually approaches equilibrium, one should expect that the evolution of the overoccupied quark-gluon plasma follows that of pure-gluon QCD, where it has been established [38,39,41,45,54] that for intermediate times $1/\Gamma_{\text{el}}^0 \ll t \ll 1/\Gamma_{\text{el}}^{\text{eq}}$, the evolution of the gluon spectrum follows a self-similar scaling behavior of the form

$$f_g(p, t) = (t/t_0)^\alpha f_0 f_S \left((t/t_0)^\beta \frac{p}{\langle p \rangle_0} \right), \quad (32)$$

where $t_0 \simeq 1/\Gamma_{\text{el}}^0$, $\langle p \rangle_0$ are the characteristic time and momentum scales, f_0 is the initial occupancy, and $f_S(x)$ is a universal scaling function up to amplitude normalization, and we adopt the normalization conditions $f_S(x=1) = f_S'(x=1) = 1$. We note that the emergence of self-similar behavior as in Eq. (32) is by no means unique to QCD, and in fact it constitutes a rather generic pattern in the equilibration of far-from equilibrium quantum systems, with similar observations reported in the context of relativistic and nonrelativistic scalar field theories [42,73].

⁴Due to the fact that the phase-space occupancies of quark/antiquarks are limited to $f_{q/\bar{q}} \leq 1$ due to Fermi statistics, such overoccupied systems are inevitably gluon dominated.

Specifically, the scaling exponents $\alpha = -4/7$, $\beta = -1/7$ follow directly from a dimensional analysis of the underlying kinetic equations [36–38,41], and describe the energy transport from the infrared toward the ultraviolet due to a direct energy cascade [74].

Based on Eq. (32), we can further estimate the evolution of some physical quantities knowing that gluons are dominant $f_g \gg 1 \geq f_{q,\bar{q}}$ in the self-similar scaling regime. In particular, the average momentum $\langle p \rangle$ increases as a function of time according to

$$\langle p \rangle(t) \simeq \frac{\int \frac{d^3 p}{(2\pi)^3} p f_g(p, t)}{\int \frac{d^3 p}{(2\pi)^3} f_g(p, t)} \sim \langle p \rangle_0 \left(\frac{t}{t_0} \right)^{1/7}, \quad (33)$$

while the typical occupancies of hard gluons decrease as

$$f(t, \langle p \rangle(t)) \simeq f_0 \left(\frac{t}{t_0} \right)^\alpha \sim f_0 \left(\frac{t}{t_0} \right)^{-4/7}. \quad (34)$$

Similarly, one finds that the screening mass

$$m_D^2(t) \simeq g^2 \int \frac{d^3 p}{(2\pi)^3} \frac{1}{2p} f_g(p, t) \sim g^2 f_0 \langle p \rangle_0^2 \left(\frac{t}{t_0} \right)^{-2/7} \quad (35)$$

decreases, such that the system dynamically establishes a separation between the soft ($\sim m_D$) and hard ($\sim \langle p \rangle$) scales over the course of the self-similar evolution [36,45]. Since the effective temperature also decreases according to [$f_g(p, t) \gg 1$]

$$T^*(t) \simeq \frac{\nu_g C_A}{d_A m_D^2} \int \frac{d^3 p}{(2\pi)^3} f_g^2(p, t) \sim g^2 f_0 \langle p \rangle_0 \left(\frac{t}{t_0} \right)^{-3/7}, \quad (36)$$

the large-angle elastic scattering rate $\Gamma_{\text{el}}(t) \sim g^2 T^* \frac{m_D^2}{\langle p \rangle^2} \sim g^4 f_0^2 \langle p \rangle_0 (t/t_0)^{-1}$ decreases over the course of the self-similar evolution and eventually becomes on the order of the equilibrium rate $\Gamma_{\text{el}}(t) \sim g^4 T_{\text{eq}}$ at the same time $t/t_0 \sim f_0^{7/4}$ when the occupancies of hard gluons $f(t, \langle p \rangle(t))$ become of order unity, and the average momentum $\langle p \rangle(t)$ becomes on the order of the equilibrium temperature $T_{\text{eq}} \sim \langle p \rangle_0 f_0^{1/4}$, indicating that the energy transfer toward the ultraviolet has been accomplished and gluons are no longer dominant for $t \gtrsim t_0 f_0^{7/4} \sim g^{-4} f_0^{-1/4} \langle p \rangle_0^{-1} \sim g^{-4} T_{\text{eq}}^{-1}$.

Beyond this timescale, the system can be considered as close to equilibrium, and should be expected to relax toward equilibrium on a timescale on the order of the kinetic relaxation time $\tau_R \sim g^{-4} T_{\text{eq}}^{-1}$, which is parametrically of the same order as the time it takes to accomplish the energy transfer toward the ultraviolet.

2. Numerical results

We now turn to the results of effective kinetic theory simulation of the equilibration process in overoccupied QCD plasmas, extending earlier results in [50]. We initialize the phase-space distributions as

$$\begin{aligned} f_g(p, t=0) &= e_0 \frac{\pi^2}{4Q^4} e^{-\frac{p^2}{Q^2}}, \\ f_q(p, t=0) &= 0, \\ f_{\bar{q}}(p, t=0) &= 0, \end{aligned} \quad (37)$$

such that for $Q^4 \ll e_0$ the system features a large occupancy $f_0 \simeq e_0 \frac{\pi^2}{4Q^4}$ of low-momentum gluons, with average momentum $\langle p \rangle_0 = \frac{2Q}{\sqrt{\pi}}$. Since the system in Eq. (37) is charge neutral, all species of quarks/antiquarks will be produced democratically over the course of the evolution.

We first consider an overoccupied system with a relatively large scale separation $\langle p \rangle_0 / T_{\text{eq}} = 0.2$ at weak coupling $\lambda = 0.1$, and investigate the evolution of the spectra of quarks and gluons depicted in the top panel of Fig. 11. Starting from a large phase-space occupancy of soft gluons, the initial spectra undergo a quick memory loss at very early times and then gradually evolve into harder spectra through a direct energy cascade, pushing the low momentum gluons toward higher momenta. In order to illustrate the self-similarity of this process, we follow previous works [32,38] and show rescaled versions of the gluon spectra in the bottom panel of Fig. 11. By rescaling the phase-space distribution as $f_S(x) \simeq (t/t_0)^{-\alpha} f_g(\langle p \rangle_0 (t/t_0)^{-\beta} x, t)$, and plotting it against the rescaled momentum variable $x = (t/t_0)^\beta p / \langle p \rangle_0$, one indeed finds that in the relevant scaling window, which corresponds approximately to times $10^{-6} \leq t \lambda^2 T_{\text{eq}} \leq 10^1$ for this particular set of parameters, the spectra at different times overlap with each other to rather good accuracy, clearly indicating the self-similarity of the underlying process. Beside the gluons, all species of quarks/antiquarks are produced democratically over the course of the evolution from elastic $gg \rightarrow q\bar{q}$ conversions and inelastic splitting $g \rightarrow q\bar{q}$ processes. Generally, one finds that the quark/antiquark spectra follow the evolution of the gluon spectra, albeit due to their Fermi statistics the number of quarks/antiquarks in the system remains negligibly small compared to the overall abundance of gluons during the self-similar stage of the equilibration process.

Eventually for times $t \gtrsim 10^2 / \lambda^2 T_{\text{eq}}$ the self-similar cascade in Fig. 11 stops as the occupancies of hard gluons fall below unity and the system subsequently approaches thermal equilibrium on timescales $\sim 10^3 / \lambda^2 T_{\text{eq}}$ for the parameters chosen in Fig. 11. It is interesting to point out that due to the negligible abundance of quarks and antiquarks in the system, the evolution of the gluon spectra slightly overshoots the equilibrium temperature at times

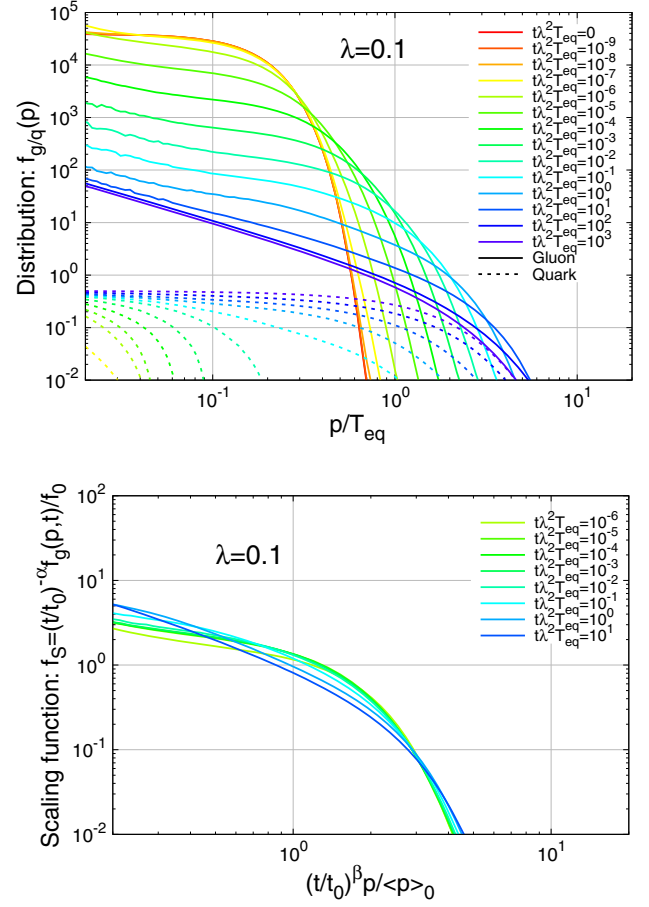


FIG. 11. (Top) Evolution of the phase-space distributions of gluons (solid lines) and quarks/antiquarks (dashed lines) in an overoccupied QCD plasma with $\langle p \rangle_0 / T_{\text{eq}} = 0.2$ at weak coupling $\lambda = 0.1$. (bottom) Scaling function f_S obtained by rescaling the gluon spectra in the top panel, with the exponents $\alpha = -4/7$, $\beta = -1/7$, and scale factors $t_0 = 0.005 T_{\text{eq}}^{-1}$ and $f_0 = 1500$.

$t \gtrsim 10^2 / \lambda^2 T_{\text{eq}}$, and subsequently relaxes back toward equilibrium as the correct equilibrium abundance of quarks and antiquarks is produced along the lines of our previous discussion of gluon dominated systems in Sec. III.

Next we will discuss the evolution of the average momentum $\langle p \rangle(t)$, the screening mass square $m_D^2(t)$, and the effective temperature $T^*(t)$ summarized in Fig. 12, where the upper panel shows the results for $\langle p \rangle_0 / T_{\text{eq}} = 0.2$, $\lambda = 0.1$, i.e., the same parameters as in Fig. 11, while the middle and bottom panels show the results for a smaller scale separation $\langle p \rangle_0 / T_{\text{eq}} = 1$, at larger values of coupling $\lambda = 1, 10$. By comparing the evolution of the various scales with the theoretical predicted power-law scaling (dashed line) in the turbulent regime [cf. Eqs. (33), (35), (36)], one finds that the scaling behavior $\langle p \rangle \propto t^{1/7}$, $T^* \propto t^{-3/7}$, and $m_D^2 \propto t^{-2/7}$ associated with the turbulent energy transport toward the ultraviolet is indeed realized during intermediate times. Due to the large separation of scales for $\langle p \rangle_0 / T_{\text{eq}} = 0.2$, $\lambda = 0.1$, the

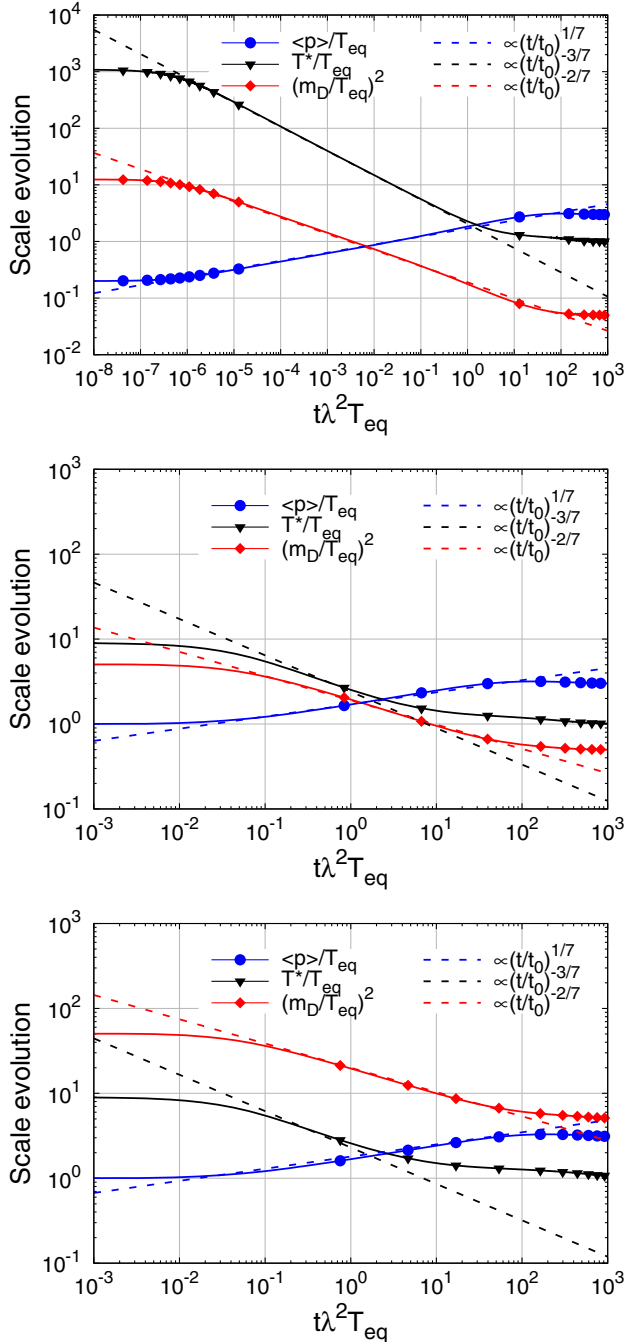


FIG. 12. Evolution of the average momentum per particle $\langle p \rangle$ (blue/circle), effective temperature T^* (black/inverted triangle), and screening mass m_D^2 (red/diamond) in an overoccupied QCD plasma at weak coupling $\langle p \rangle_0/T_{\text{eq}} = 0.2$, $\lambda = 0.1$ (top), intermediate coupling $\langle p \rangle_0/T_{\text{eq}} = 1$, $\lambda = 1$ (middle), and at strong coupling $\langle p \rangle_0/T_{\text{eq}} = 1$, $\lambda = 10$ (bottom). Dashed lines show the characteristic power-law behavior in the self-similar turbulent regime.

scaling window in the top panel of Fig. 12 extends over a significant period of time $10^{-6} \leq t\lambda^2 T_{\text{eq}} \leq 10^1$, consistent with the scaling of the gluon distribution observed in Fig. 11. Even though the scaling window shrinks

significantly for the smaller scale separations $\langle p \rangle_0/T_{\text{eq}} = 1$ shown in the middle and bottom panels of Fig. 12, it is remarkable that the same turbulent mechanism appears to be responsible for the energy transfer even for such moderately strongly coupled systems.

Even though a significant amount of time is spent to accomplish the turbulent energy transfer, the logarithmic representation in Fig. 12 spoils the fact that it is the ultimate approach toward equilibrium which requires the largest amount of time. Beyond the investigation of the dynamical evolution of various scales, it is therefore useful to consider the evolution of the ratios of different scales compared to their equilibrium values, as indicators of the equilibration progress. We present our results in Fig. 13, where the upper panel shows the evolution of the energy densities of gluons and quarks, approaching their equilibrium limits around $t \simeq 1.5-2\tau_R$, similar to near-equilibrium systems shown in Fig. 6. The next two panels of Fig. 13 show the screening mass square evolution of $m_D^2(t)$ and $m_Q^2(t)$, which rapidly decrease at early times, and eventually approach their equilibrium values at $t \simeq 1-1.5\tau_R$. Similar observations also hold for the effective temperature $T^*(t)$ shown in the fourth panel of Fig. 13. Due to the delayed chemical equilibration of the system, the average momentum $\langle p \rangle(t)$ shown in the bottom panel has a nonmonotonic behavior, where the rapid increase at early times due to the direct energy cascade overshoots the equilibrium value, before $\langle p \rangle(t)$'s gradual decrease at later times as energy is redistributed between quarks and gluons, eventually approaching the equilibrium limit around $t \simeq 1.5-2\tau_R$.

Since in Fig. 13 the ultimate approach toward equilibrium is mostly insensitive to the initial scale separations $\langle p \rangle_0/T_{\text{eq}}$ and coupling strength λ in Fig. 12 when expressed in units of the kinetic relaxation time τ_R , we can estimate the equilibration time of an overoccupied system as

$$t_{\text{eq}} \simeq 1 - 2\tau_R, \quad (38)$$

where, as usual, the exact numerical value depends on the detailed criteria chosen to define the equilibration time.

B. Equilibration of underoccupied systems

Next we consider the opposite limit of an underoccupied system, where the energy density is initially carried by a small number $f_0 \ll 1$ of high energetic particles, with average momentum $\langle p \rangle_0 \gg T_{\text{eq}}$. While there can be a large separation of scales, one finds that in contrast to overoccupied systems the final equilibrium temperature $T_{\text{eq}} \sim f_0^{1/4} \langle p \rangle_0 \ll \langle p \rangle_0$ is much smaller than the average initial momentum for underoccupied systems. Since the scale hierarchy is reversed, the thermalization process for an underoccupied system requires an energy transport from the ultraviolet to the infrared, which as we will discuss

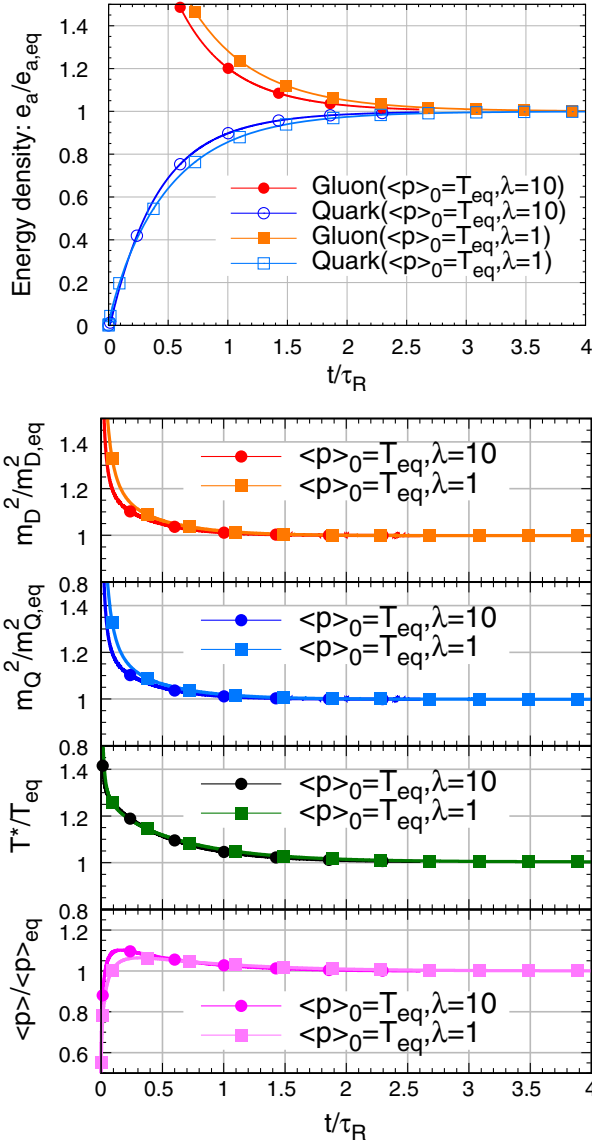


FIG. 13. Evolution of the energy densities of quarks and gluons (top), the characteristic scales (bottom) $m_D^2(t)$ (red), $m_Q^2(t)$ (blue), $T^*(t)$ (green), and $\langle p \rangle$ (pink) in an overoccupied QCD plasma at two different coupling strengths $\lambda = 1$ (lighter color/square) and $\lambda = 10$ (darker color/circle). Scales are normalized to their respective equilibrium values, while the evolution time t is normalized to the equilibrium relaxation time τ_R in Eq. (27) in order to take into account the leading coupling dependence.

shortly will be accomplished via an inverse turbulent cascade of successive radiative emissions. While the qualitative features of this bottom-up thermalization mechanism have been established a long time ago [34], recent works in the context of thermalization and jet quenching studies [75–77] have provided a more quantitative description of the different stages and clarified the relation to turbulence. Based on our effective kinetic description of QCD, we will extend previous findings in pure glue QCD [46] to full QCD at zero and nonzero densities.

1. Theoretical aspects

Before we turn to our numerical results, we briefly recall the basic features of the bottom-up thermalization in QCD plasmas following the discussion in [32]. Starting from a dilute population of $f_0 \ll 1$ highly energetic particles with $\langle p \rangle_0 \gg T_{\text{eq}}$, elastic interactions between primary hard particles induce the emission of soft gluon radiation, which accumulates at low momenta. Due to the fact that elastic and inelastic interactions are more efficient at low momentum, the initially overpopulated soft sector eventually thermalizes on a timescale $t \sim g^{-4} f_0^{-1/3} \langle p \rangle_0^{-1}$, before the highly energetic primary particles have had sufficient time to decay. Even though at this time most of the energy is still carried by the hard primaries, the soft thermal bath begins to dominate screening and scattering, such that in the final stages of bottom-up equilibration, the few remaining hard particles lose their energy to the soft thermal bath, much as a jet losing energy to a thermal medium [32,34,46,77].

Based on recent studies [75–77], the energy loss of hard primaries is accomplished by a turbulent inverse energy cascade, where the hard primary quarks/gluons, undergo successive splittings until the momenta of the radiated quanta becomes on the order of the temperature $T_{\text{soft}}(t)$ of the soft thermal bath. Specifically, at intermediate scales $T_{\text{soft}}(t) \ll p \ll \langle p \rangle_0$, the distributions of quarks/antiquarks and gluons can be expected to feature the Kolmogorov-Zakharov spectra of weak-wave turbulence [76,77]

$$f_{\text{KZ}}(\vec{p}, t) \propto \left(\frac{\langle p \rangle_0}{p} \right)^{\frac{7}{2}}, \quad (39)$$

which describe a scale-invariant energy flux from the ultraviolet $\sim \langle p \rangle_0$ to the infrared $\sim T_{\text{soft}}(t)$, ensuring that the energy of the hard particles is deposited in the thermal medium without an accumulation of energy at intermediate scales.

Due to the energy loss of the hard primary particles, the temperature of the soft thermal bath increases until eventually the hard primaries have lost most of their energy to the thermal bath and the system approaches equilibrium. We note that due to the parametric suppression of inelastic rates for high-energy particles⁵ $\Gamma_{\text{inel}}^{\text{eq}}(\langle p \rangle_0) \sim g^4 T_{\text{eq}} \sqrt{\frac{T_{\text{eq}}}{\langle p \rangle_0}}$, the energy loss of the hard primaries is slow compared to the equilibration of the soft sector, such that for sufficiently large scale separations $\frac{\langle p \rangle_0}{T_{\text{eq}}} \gg 1$ the thermalization of the system occurs on timescales $t \sim g^{-4} T_{\text{eq}}^{-1} \sqrt{\frac{\langle p \rangle_0}{T_{\text{eq}}}}$, which can be significantly larger than the kinetic relaxation time $\tau_R \sim g^{-4} T_{\text{eq}}^{-1}$.

⁵Since quasidemocratic $z \sim 1/2$ splittings dominate the turbulent energy transfer [32,76], this can be seen by evaluating Eq. (24) for $z \sim 1/2$.

2. Bottom-up thermalization of quark-gluon plasma

When considering the dynamics of underoccupied QCD plasmas, we need to specify the initial conditions for the momentum distribution, and we can further distinguish different chemical compositions of the plasma. We will limit our investigation to the following three cases, corresponding to (1) an initially underoccupied plasma of gluons, (2) an initially underoccupied plasma of quarks/antiquarks, and (3) an initially underoccupied plasma of quarks.

We will employ the following initial conditions for an underoccupied plasma of gluons:

$$\begin{aligned} f_g(p, t=0) &= \left(\frac{2\nu_q N_f}{\nu_g} \right) f_0 e^{-\frac{(p-p_0)^2}{Q^2}}, \\ f_q(p, t=0) &= 0, \\ f_{\bar{q}}(p, t=0) &= 0, \end{aligned} \quad (40)$$

while for an underoccupied plasma of quarks/antiquarks

$$\begin{aligned} f_g(p, t=0) &= 0, \\ f_q(p, t=0) &= f_0 e^{-\frac{(p-p_0)^2}{Q^2}}, \\ f_{\bar{q}}(p, t=0) &= f_0 e^{-\frac{(p-p_0)^2}{Q^2}}, \end{aligned} \quad (41)$$

and for an underoccupied plasma of quarks, the system is initialized as

$$\begin{aligned} f_g(p, t=0) &= 0, \\ f_q(p, t=0) &= 2f_0 e^{-\frac{(p-p_0)^2}{Q^2}}, \\ f_{\bar{q}}(p, t=0) &= 0, \end{aligned} \quad (42)$$

where in all of the above relations the normalization

$$f_0 = \frac{2\pi^2 e_{\text{eq}}(T_{\text{eq}}, \mu_{\text{eq}})}{9Q \left[\frac{2(p_0^2 + Q^2)Q}{e^{p_0^2/Q^2}} + p_0 \sqrt{\pi} (2p_0^2 + 3Q^2) (1 + \text{erf}(\frac{p_0}{Q})) \right]} \quad (43)$$

is chosen, such that all the systems have exactly the same energy density $e_{\text{eq}}(T_{\text{eq}}, \mu_{\text{eq}})$. By varying the parameter $p_0 \simeq \langle p \rangle_0$, we can then adjust the separation of scales between the initial energy of the hard particles and the final equilibrium temperature. Since for $Q \ll p_0$, we do not expect a significant sensitivity of our results to the parameter Q that controls the initial width of the momentum distribution, we will employ $Q = T_{\text{eff}}$ in the following.

We note that the underoccupied QCD plasmas of gluons in Eq. (40) and quarks/antiquarks in Eq. (41) are charge neutral such that quarks and antiquarks of all light flavors “ u , d , s ” will be produced with equal abundancies. Notably

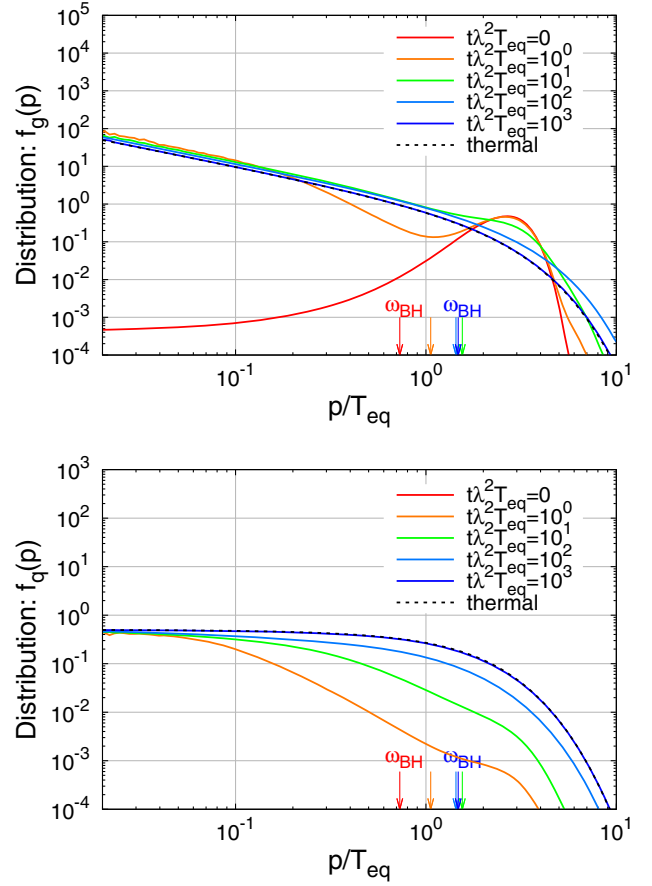


FIG. 14. Evolution of the phase-space distributions of gluons (top) and quarks/antiquarks (bottom) in an *underoccupied gluon system* with $\langle p \rangle_0/T_{\text{eq}} = 3$ at coupling $\lambda = 1$. Dotted lines show the thermal equilibrium distributions. Vertical arrows mark the Bethe-Heitler frequencies ω_{BH} .

this is not the case for the initial conditions in Eq. (42), where the imbalance of quarks and antiquarks describes a system with a finite net-charge density, and we will for simplicity assume a degeneracy among “ u , d , s ” flavors.

a. Underoccupied gluons.—We start by analyzing the evolution of underoccupied gluon systems in order to provide a direct and intuitive understanding of the bottom-up thermalization scenario. The evolution of the momentum spectra of quarks and gluons during the thermalization process is presented in Figs. 14, 15, 16, and 17 for weakly coupled plasmas $\lambda = 1$ with different average initial momenta $\langle p \rangle_0/T_{\text{eq}} = 3$ in Fig. 14, $\langle p \rangle_0/T_{\text{eq}} = 10$ in Fig. 15, $\langle p \rangle_0/T_{\text{eq}} = 30$ in Fig. 16, and $\langle p \rangle_0/T_{\text{eq}} = 100$ in Fig. 17. Different panels show the evolution of the gluon distributions $f_g(p)$ and quark/antiquark distributions $f_q(p)$, while different curves in each panel correspond to different evolution times $t\lambda^2 T_{\text{eq}}$ with vertical arrows marking the characteristic Bethe-Heitler frequency at each stage of the evolution.

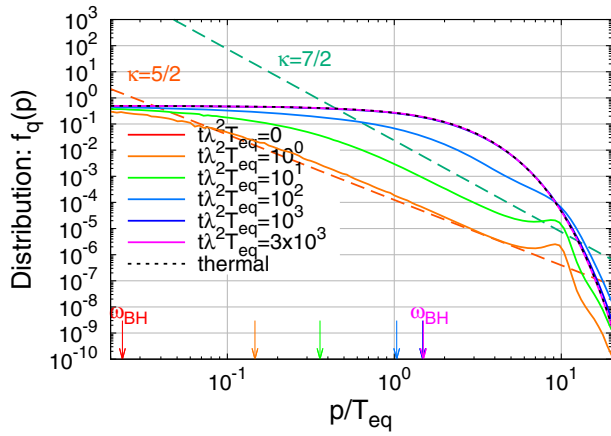
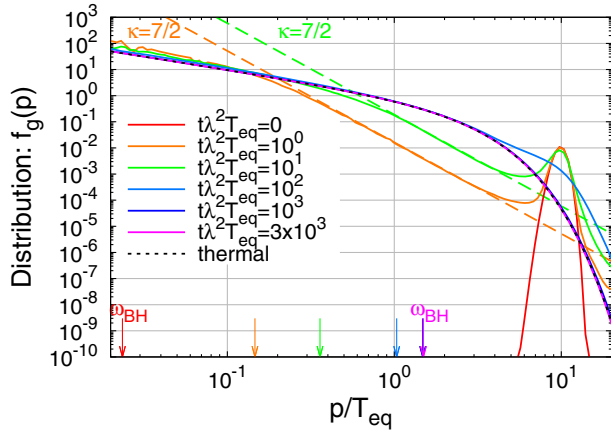


FIG. 15. Evolution of the phase-space distributions of gluons (top) and quarks/antiquarks (bottom) in an *underoccupied gluon system* with $\langle p \rangle_0/T_{eq} = 10$ at coupling $\lambda = 1$. Dashed lines show the characteristic power-law dependence of the single emission LPM spectra (orange) and the Kolmogorov Zakharov spectra (green). Dotted lines show the thermal equilibrium distributions. Vertical arrows mark the Bethe-Heitler frequencies ω_{BH} .

By investigating the results for the larger scale separations $\langle p \rangle_0/T_{eq} = 10$ in Fig. 15, $\langle p \rangle_0/T_{eq} = 30$ in Fig. 16, and $\langle p \rangle_0/T_{eq} = 100$ in Fig. 17, one clearly observes that soft radiation processes $g \rightarrow gg$ and $g \rightarrow q\bar{q}$ rapidly build up a large population of soft quarks and gluons with typical momenta $p \lesssim \omega_{BH}$. Even though at early times, such as e.g., $t\lambda^2 T_{eq} \ll 1$ in Fig. 17, the soft sector is overoccupied and thus highly gluon dominated, one finds that for sufficiently large scale separations, the overoccupation is depleted and the soft sector thermalizes before the hard primaries lose most of their energy to the soft thermal bath. Since at intermediate scales $\omega_{BH} \ll p \ll \langle p \rangle_0$ the emission is in the LPM regime, the spectra of gluons and quarks initially feature a characteristic power-law behavior $f_g \sim p^{-7/2}$, $f_q \sim p^{-5/2}$ for momenta $\omega_{BH} \ll p \ll \langle p \rangle_0$, associated with the single emission spectra of the $g \rightarrow gg$ and $g \rightarrow q\bar{q}$ processes. Subsequently, the energy of the hard primaries is transferred to the soft thermal bath, via an inverse turbulent cascade due to multiple successive

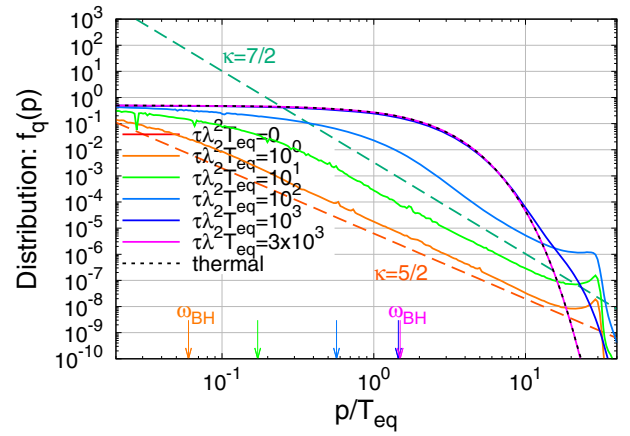
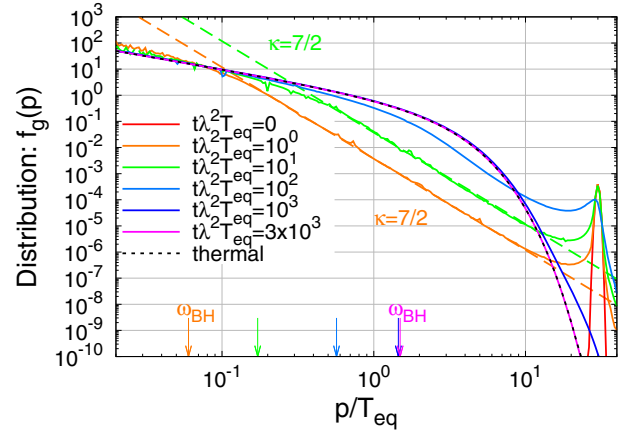


FIG. 16. Evolution of the phase-space distributions of gluons (top) and quarks/antiquarks (bottom) in an *underoccupied gluon system* with $\langle p \rangle_0/T_{eq} = 30$ at coupling $\lambda = 1$. Dashed lines show the characteristic power-law dependence of the single emission LPM spectra (orange) and the Kolmogorov Zakharov spectra (green). Dotted lines show the thermal equilibrium distributions. Vertical arrows mark the Bethe-Heitler frequencies ω_{BH} .

$g \rightarrow gg$, $g \rightarrow q\bar{q}$, and $q \rightarrow qg$ branchings, giving rise to the characteristic Kolmogorov-Zakharov spectrum $f_{g/q} \sim p^{-7/2}$ in both the gluon and quark sectors. Since the energy injected into this cascade by the hard primaries at the scale $\sim \langle p \rangle_0$ is transmitted all the way to the soft bath $\sim \omega_{BH}$ the temperature of the soft bath increases monotonically, as seen e.g., in Fig. 17, until eventually the hard primaries have lost nearly all of their energy and the system thermalizes. During the final stages of the approach toward equilibrium, a small number of hard primaries continues to lose energy giving rise to high momentum tails of the quark and gluon spectra seen for $t\lambda^2 T_{eq} = 10^3$ in Figs. 15, 16, 17. Notably, the underoccupied system initially maintains a memory of the momentum distribution of hard primaries until the final stages of the thermalization process, which then closely resembles the mechanism of jet energy loss in a thermal medium [77].

Even for the smallest separation of scales $\langle p \rangle_0/T_{eq} = 3$ shown in Fig. 14, some of the characteristic patterns of

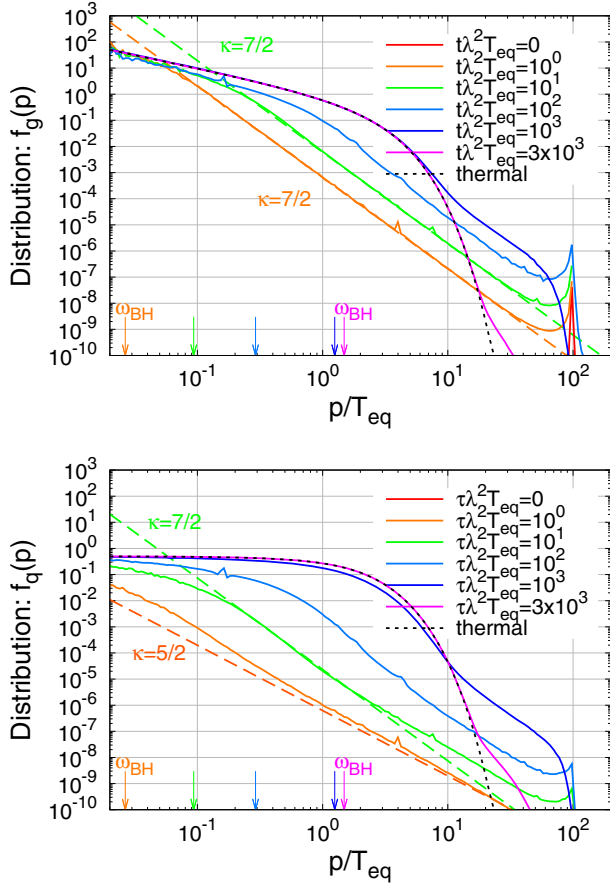


FIG. 17. Evolution of the phase-space distributions of gluons (top) and quarks/antiquarks (bottom) in an *underoccupied gluon system* with $\langle p \rangle_0/T_{\text{eq}} = 100$ at coupling $\lambda = 1$. Dashed lines show the characteristic power-law dependence of the single emission LPM spectra (orange) and the Kolmogorov Zakharov spectra (green). Dotted lines show the thermal equilibrium distributions. Vertical arrows mark the Bethe-Heitler frequencies ω_{BH} .

bottom-up thermalization are still clearly visible, although in this case radiative emissions occur in the Bethe-Heitler regime. Nevertheless, hard gluons with momenta $p \sim \langle p \rangle_0$ still radiate soft gluons via $g \rightarrow gg$, leading to the formation of a soft thermal spectrum of gluons at low momenta. Even though quarks/antiquarks are also produced via $g \rightarrow q\bar{q}$ branching, one observes that the evolution in the quark sector is slightly slower than in the gluon sector, indicating once again that the energy transfer from gluons to quarks associated with the chemical equilibration of the system can cause a delay in the equilibration of the system.

Now in order to compare the evolution of the different systems, we again consider the evolution of the characteristic dynamical scales m_D^2 , m_Q^2 , T^* , and $\langle p \rangle$. Since in accordance with the discussion in Sec. III we anticipate that, for sufficiently large scale separations, the equilibration time of the system will be delayed by a factor $\sqrt{\langle p \rangle_0/T_{\text{eq}}}$, relative to the equilibrium relaxation time

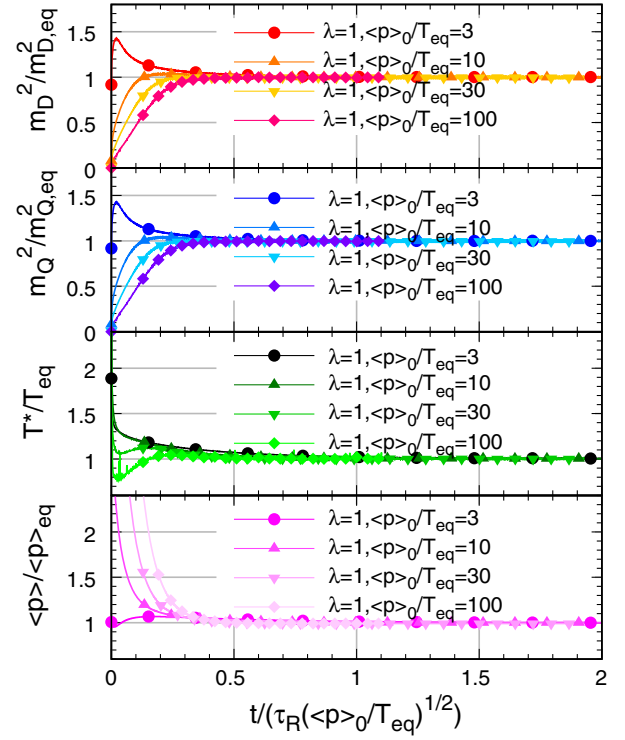


FIG. 18. Evolution of the characteristic scales $m_D^2(t)$ (red), $m_Q^2(t)$ (blue), $T^*(t)$ (green), and $\langle p \rangle$ (pink) in an *underoccupied gluon system* at coupling strengths $\lambda = 1$ for different scale separations $\langle p \rangle_0/T_{\text{eq}} = 3, 10, 30, 100$ (darker to lighter colors/circle, triangle, inverted triangle, diamond). Scales are normalized to their respective equilibrium values, while the evolution time t is normalized to $\tau_R \sqrt{\frac{p_0}{T_{\text{eq}}}}$ in order to take into account the leading dependence on the initial energy $\langle p \rangle_0$.

τ_R , we will consider normalizing the evolution time to $\tau_R \sqrt{\langle p \rangle_0/T_{\text{eq}}}$ when comparing the results for different average initial momenta $\langle p \rangle_0/T_{\text{eq}}$ in Figs. 18 and 19. Since the different scales m_D^2 , m_Q^2 , T^* , and $\langle p \rangle$ exhibit different sensitivities to the hard and soft components of the plasma, their time evolutions are actually quite different. While for scale separations $\langle p \rangle_0 \gtrsim 10T_{\text{eq}}$, screening masses m_D^2 and m_Q^2 are very quickly dominated by the soft thermal bath and subsequently experience a strong rise as the soft bath heats up, the scale T^* characterizing the strength of elastic interactions receives significant contributions from the hard primaries at early times, before it is eventually dominated by the soft bath. Since the hard primaries carry most of the energy of the system until they eventually equilibrate, the average energy per particle $\langle p \rangle$ is always dominated by the hard sector, and decreases monotonically over the course of the evolution. Besides the equilibration of the various scales, it is also interesting to consider the chemical equilibration of the system in Fig. 19, where we present the energy fractions and average momenta separately for quarks and gluons. While for large scale separations chemical equilibration in

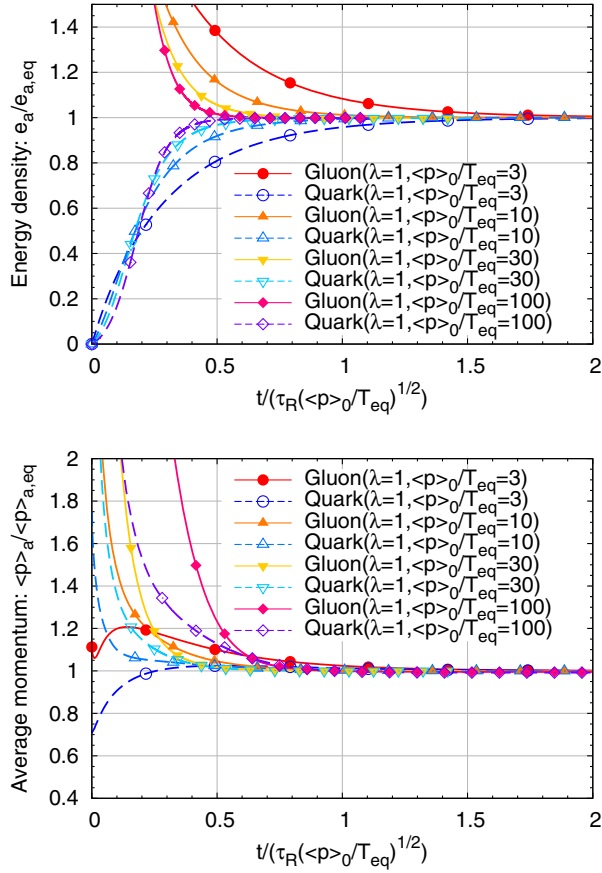


FIG. 19. Evolution of the energy densities (top) and average momenta (bottom) of quarks (dashed line/open symbol) and gluons (solid line/closed symbol) in an *underoccupied gluon system* at coupling strengths $\lambda = 1$ for different scale separation $\langle p \rangle_0/T_{\text{eq}} = 3, 10, 30, 100$ (circle, triangle, inverted triangle, diamond). Energy densities and average momenta are normalized to their respective equilibrium values, while the evolution time t is normalized to $\tau_R \sqrt{\frac{p_0}{T_{\text{eq}}}}$ in order to take into account the leading dependence on the initial energy $\langle p \rangle_0$.

Fig. 19 occurs on the same timescales as kinetic equilibration in Fig. 18, one finds that for smaller scale separations the energy transfer from gluons to quarks requires additional time, delaying the equilibration of the system.

Generally, for scale separations $\langle p \rangle_0/T_{\text{eq}} \gtrsim 10$, one finds that the scaling of the evolution time with $\sqrt{\langle p \rangle_0/T_{\text{eq}}}$ leads to comparable results for the equilibration time

$$t_{\text{eq}} \simeq 0.5 - 1.0 \tau_R \sqrt{\frac{\langle p \rangle_0}{T_{\text{eq}}}}, \quad (44)$$

albeit the curves for different $\langle p \rangle_0/T_{\text{eq}}$ in Figs. 18 and 19 do not overlap completely, indicating that subleading corrections to this estimate still seem to be important for the scale separations considered in our study.

b. Underoccupied quarks and antiquarks.—Similar to the underoccupied gluon systems, we will now consider charge neutral systems of underoccupied quarks/antiquarks. We proceed along the same lines and first investigate the evolution of the spectra for $\langle p \rangle_0/T_{\text{eq}} = 3, 10, 30$ which are depicted in Figs. 20, 21, and 22. Generally, one finds that the thermalization processes follow essentially the same patterns as for the underoccupied gluon systems, with the inelastic production of soft quarks and gluons $q \rightarrow gq$ leading to the rapid buildup of the soft sector, before the hard primary quarks and antiquarks lose their energy via multiple successive branchings giving rise to the familiar Kolmogorov-Zakharov spectra $f_{g/q} \sim p^{-7/2}$ at intermediate momentum scales $\omega_{\text{BH}} \ll p \ll \langle p \rangle_0$. Due to the radiative breakup of the hard primaries, the soft sector heats up, until the system eventually equilibrates when all of the hard primaries have had sufficient time to decay. While at early times the hard components of the spectra ($p \sim \langle p \rangle_0$) closely reflect the initial conditions, it is interesting to observe that during the final approach toward equilibrium, e.g., for $t\lambda^2 T_{\text{eq}} = 10^3$ in Figs. 16 and 22, the momentum distribution and chemistry of the remaining hard particles are significantly modified, and there is no longer a significant difference between underoccupied gluon systems and underoccupied quark/antiquark systems.

By comparing the results for the evolution of the dynamical scales m_D^2, m_Q^2, T^* , and $\langle p \rangle$ in Fig. 23 for the underoccupied quark/antiquark systems to the corresponding results for underoccupied gluons, one again observes essentially the same qualitative patterns. However, it is interesting to see that for underoccupied systems of quarks and antiquarks, the approach toward equilibrium appears to occur on a somewhat larger timescale $\gtrsim 0.5 \tau_R \sqrt{\langle p \rangle_0/T_{\text{eq}}}$ as compared to underoccupied gluon systems, where by $0.5 \tau_R \sqrt{\langle p \rangle_0/T_{\text{eq}}}$ all the scales m_D^2, m_Q^2, T^* , and $\langle p \rangle$ are already close to their respective equilibrium values. Based on our discussion in Sec. II B 2 b, we believe that this discrepancy at intermediate times can be attributed to the different color factors in the inelastic interaction rates for the hard primary quarks/antiquarks and gluons, as discussed in detail in the context of jet quenching in [77]. However, if one is concerned with the ultimate approach toward equilibrium, one should take into account the fact that at late times asymmetric $g \rightarrow q\bar{q}$ and $q \rightarrow gq$ splittings can significantly modify the quark/gluon composition of hard fragments [76], such that underoccupied systems of quarks and gluons can ultimately be expected to equilibrate at the same rate.

Next, in order to investigate the chemical equilibration of the underoccupied quark/antiquark systems, we present our simulation results for the evolution of the energy fraction of quarks and gluons, and their average

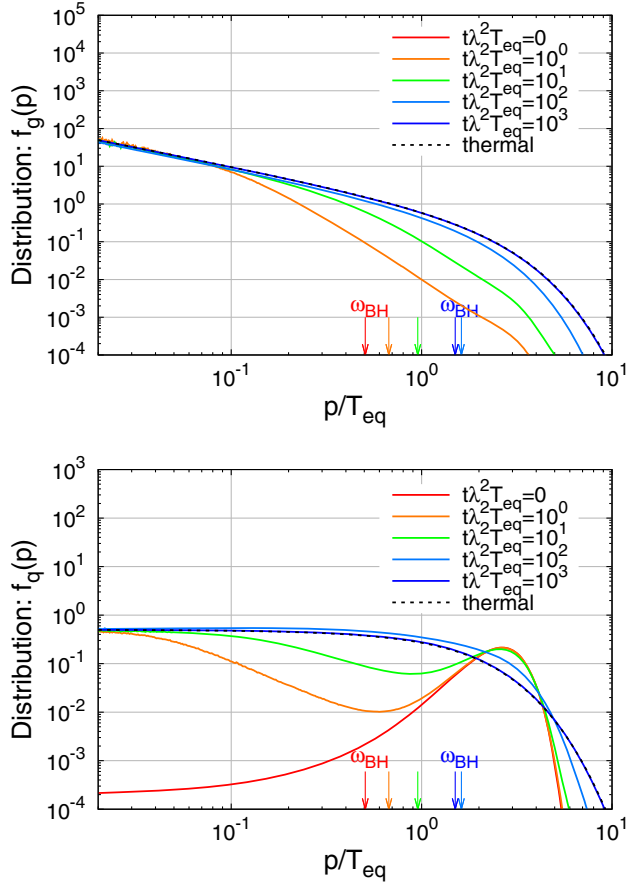


FIG. 20. Evolution of the phase-space distributions of gluons (top) and quarks/antiquarks (bottom) in an *underoccupied quark/antiquark system* with $\langle p \rangle_0/T_{\text{eq}} = 3$ at coupling $\lambda = 1$. Dotted lines show the thermal equilibrium distributions. Vertical arrows mark the Bethe-Heitler frequencies ω_{BH} .

momenta in Fig. 24. Interestingly, one finds that in contrast to the behavior for underoccupied gluon systems in Fig. 19, the energy fractions of quarks and gluons in the system exhibit a nonmonotonic behavior. Even though initially all the energy is carried by the hard primary quarks and antiquarks, it turns out that for larger scale separations $\langle p \rangle_0/T_{\text{eq}} = 10, 30$, gluons dominate the energy budget before the chemical equilibration of the system. By inspecting also the behaviors of the average momenta in the lower panel of Fig. 24, one finds that these gluons are typically soft, with the average momenta $\langle p \rangle$ close to the equilibrium value. We believe that this behavior can be attributed to the fact that gluon radiation dominates the energy transfer from the hard to the soft sector, such that the soft thermal bath absorbs the energy predominantly in the form of gluons, before the energy is eventually redistributed among quarks and gluons.

c. Underoccupied quarks.—So far we have investigated the equilibration of charge neutral systems of

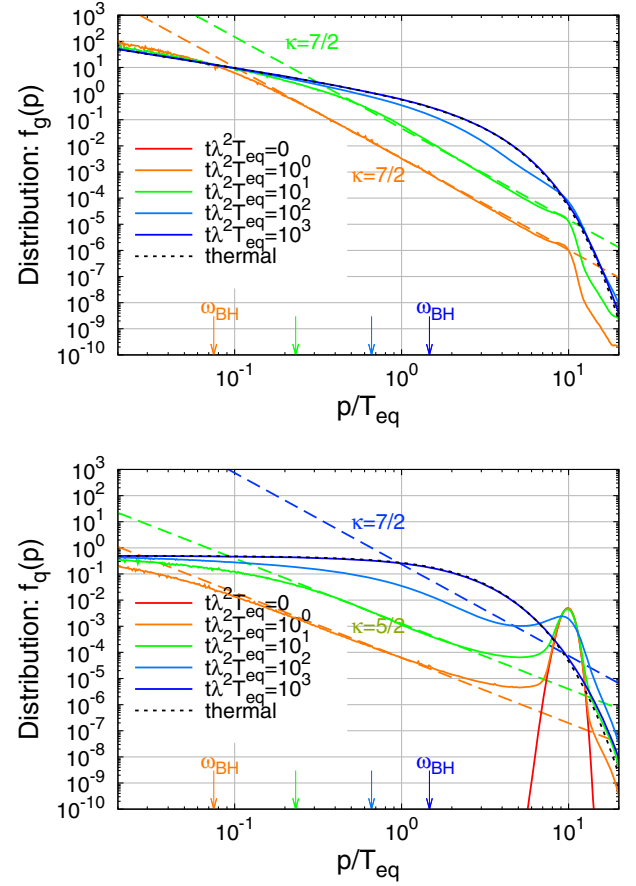


FIG. 21. Evolution of the phase-space distributions of gluons (top) and quarks/antiquarks (bottom) in an *underoccupied quark/antiquark system* with $\langle p \rangle_0/T_{\text{eq}} = 10$ at coupling $\lambda = 1$. Dashed lines show the characteristic power-law dependence of the single emission LPM spectra ($\kappa = 5/2, 7/2$) and the Kolmogorov Zhabarov spectra ($\kappa = 7/2$). Dotted lines show the thermal equilibrium distributions. Vertical arrows mark the Bethe-Heitler frequencies ω_{BH} .

underoccupied gluons, quarks/antiquarks. Next we consider the equilibration of underoccupied systems of quarks, which in accordance with Eq. (42) carry nonzero densities of the conserved u, d, s charges. Since in the presence of finite charge densities, the evolution of quarks and antiquarks will be different, we first study the evolution of spectra of gluons, quarks, and antiquarks, which are depicted in Fig. 25 for $\langle p \rangle_0/T_{\text{eff}} = 3$ and in Fig. 26 for $\langle p \rangle_0/T_{\text{eff}} = 10$. Evidently, the evolution of the quark and gluon spectra in Figs. 25 and 26 are very similar to the quark/antiquark spectra in Figs. 20 and 21 obtained in the zero density cases. However, significant differences can be observed for the evolution of the antiquarks, as for the underoccupied systems of quarks there are no antiquarks present in the initial conditions. Instead, the population of antiquarks observed at later times is produced via gluon splittings $g \rightarrow q\bar{q}$ and elastic $gg \rightarrow q\bar{q}$ conversions. Hence, the evolution of

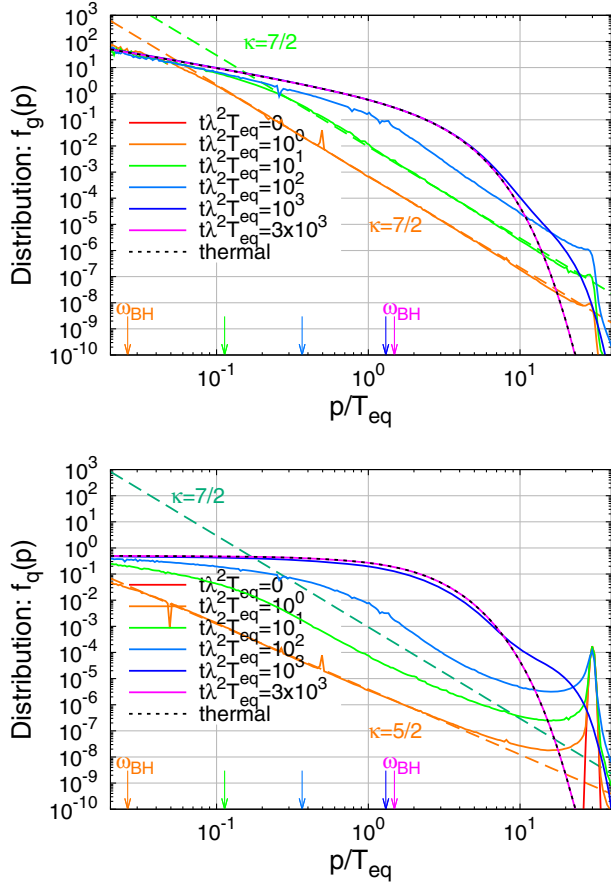


FIG. 22. Evolution of the phase-space distributions of gluons (top) and quarks/antiquarks (bottom) in an *underoccupied quark/antiquark system* with $\langle p \rangle_0/T_{\text{eq}} = 30$ at coupling $\lambda = 1$. Dashed lines show the characteristic power-law dependence of the single emission LPM spectra ($\kappa = 5/2, 7/2$) and the Kolmogorov Zakharov spectra ($\kappa = 7/2$). Dotted lines show the thermal equilibrium distributions. Vertical arrows mark the Bethe-Heitler frequencies ω_{BH} .

the antiquark spectra closely follow the gluon spectra, as can be seen by comparing the upper and lower panels in Figs. 25 and 26.

By comparing the evolution of the characteristic scales for the zero and finite density systems in Figs. 23 and 27, one finds that the presence of the additional conserved charges does not significantly affect the kinetic equilibration of the system, in accordance with the finding that the evolution of quark and gluon spectra is essentially unchanged. However, when considering the evolution of the individual contributions of gluons, quarks, and antiquarks to the energy densities in Figs. 24 and 28, one clearly observes that the chemical equilibration associated with the production of antiquarks requires a significant amount of time, with energy densities of gluons and antiquarks only approaching their equilibrium ratios for times $\gtrsim \tau_R \sqrt{\langle p \rangle_0/T_{\text{eq}}}$.

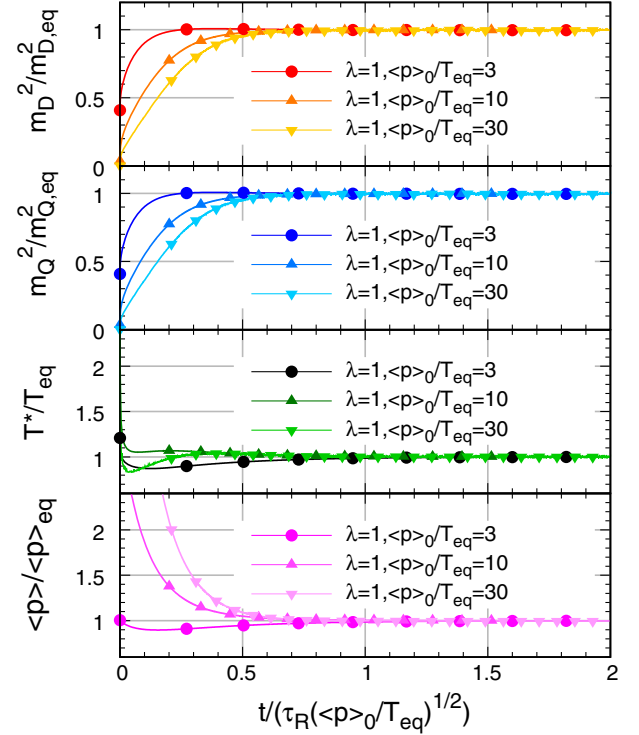


FIG. 23. Evolution of the characteristic scales $m_D^2(t)$ (red), $m_Q^2(t)$ (blue), $T^*(t)$ (green), and $\langle p \rangle$ (pink) in an *underoccupied quark/antiquark system* at coupling strengths $\lambda = 1$ for different scale separations $\langle p \rangle_0/T_{\text{eq}} = 3, 10, 30, 100$ (darker to lighter colors/circle, triangle, inverted triangle). Scales are normalized to their respective equilibrium values, while the evolution time t is normalized to $\tau_R \sqrt{\frac{\langle p \rangle_0}{T_{\text{eq}}}}$ in order to take into account the leading dependence on the initial energy $\langle p \rangle_0$.

V. EQUILIBRATION OF LONGITUDINALLY EXPANDING PLASMAS

So far we have discussed kinetic and chemical equilibration for homogeneous and isotropic systems. Now in order to address the early time dynamics of high-energy heavy-ion collisions, we will focus on systems which are transversely homogeneous and longitudinally invariant under a Lorentz boost, but can feature an anisotropy between longitudinal and transverse momenta. Denoting

$$x^\mu = \tau(\cosh(\eta), u_T^1, u_T^2, \sinh(\eta)) = (t, x_T^1, x_T^2, z),$$

$$p^\mu = p_T(\cosh(y), v_T^1, v_T^2, \sinh(y)) = (E, p_T^1, p_T^2, p_z),$$

where

$$\tau = \sqrt{t^2 - z^2}, \quad \eta = \frac{1}{2} \ln \left(\frac{t+z}{t-z} \right),$$

$$p_T = \sqrt{E^2 - p_z^2}, \quad y = \frac{1}{2} \ln \left(\frac{E+p_z}{E-p_z} \right), \quad (45)$$

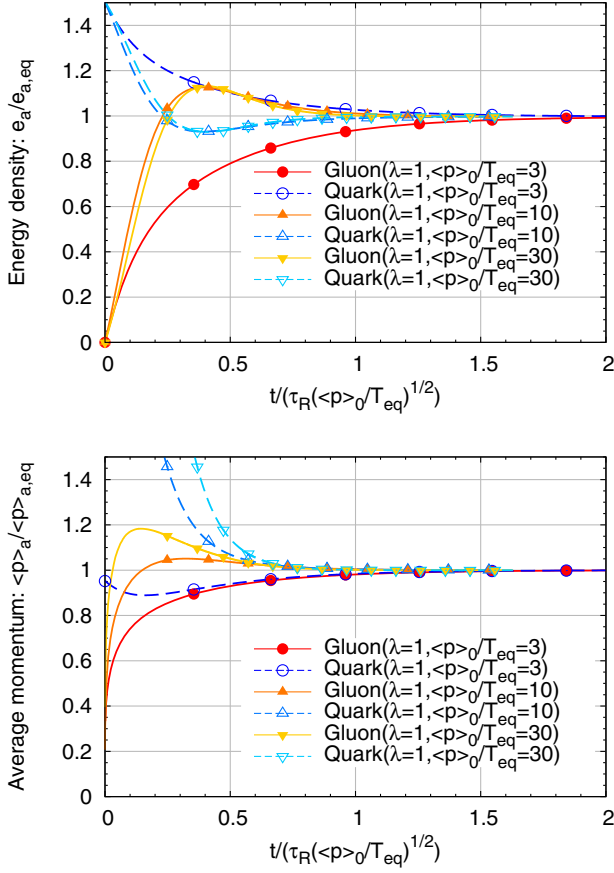


FIG. 24. Evolution of the energy densities (top) and average momenta (bottom) of quarks (dashed line/open symbol) and gluons (solid line/closed symbol) in an *underoccupied quark/antiquark* system at coupling strengths $\lambda = 1$ for different scale separations $\langle p \rangle_0/T_{\text{eq}} = 3, 10, 30$ (circle, triangle, inverted triangle). Energy densities and average momenta are normalized to their respective equilibrium values, while the evolution time t is normalized to $\tau_R \sqrt{\frac{p_0}{T_{\text{eq}}}}$ in order to take into account the leading dependence on the initial energy $\langle p \rangle_0$.

the phase-space distribution $f(x, p)$ for a longitudinally boost invariant and transversely homogeneous system can be conveniently expressed in the form $f(x, p) = f(\tau, p_T, p_{\parallel})$, where the variable p_{\parallel} denotes the longitudinal momentum $p_{\parallel} = p_T \sinh(y - \eta)$ in the local rest frame $u^\mu = (\cosh(\eta), 0, 0, \sinh(\eta))$ of the nonequilibrium plasma.

Since the system is homogeneous in transverse coordinates \mathbf{x}_T and the longitudinal rapidity η , the resulting Boltzmann equation [78]

$$\left[\frac{\partial}{\partial \tau} - \frac{p_{\parallel}}{\tau} \frac{\partial}{\partial p_{\parallel}} \right] f_a(\tau, p_T, p_{\parallel}) = -C_a^{2 \leftrightarrow 2}[f](\tau, p_T, p_{\parallel}) - C_a^{1 \leftrightarrow 2}[f](\tau, p_T, p_{\parallel}) \quad (46)$$

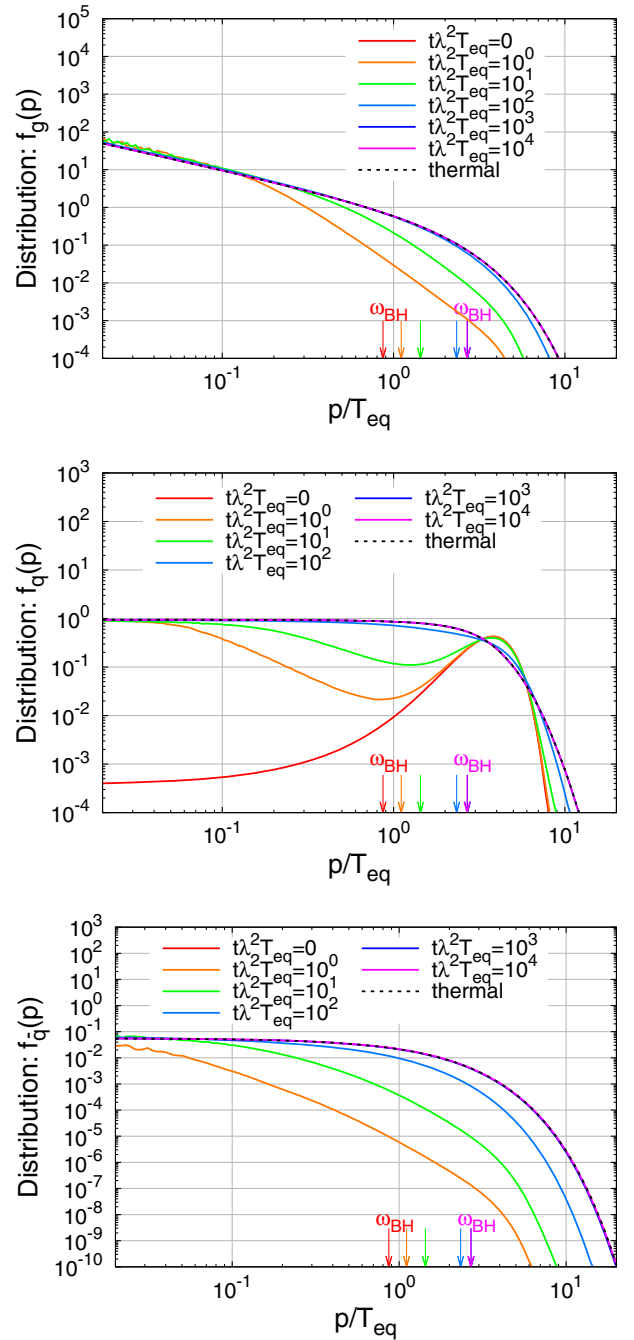


FIG. 25. Evolution of the phase-space distributions of gluons (top), quarks (middle), and antiquarks (bottom) in an *underoccupied quark* system with $\langle p \rangle_0/T_{\text{eq}} = 3$ at coupling $\lambda = 1$. Different flavors of quarks/antiquarks are assumed to be identical and the equilibrium temperature is $T_{\text{eq}} \simeq 0.70 T_{\text{eff}}$. Dotted lines show the thermal equilibrium distributions. Vertical arrows mark the Bethe-Heitler frequencies ω_{BH} .

takes essentially the same form as in Eq. (6) with one additional term that can be reexpressed in the form of an additional collision integral $-C_a^{\text{exp}}[f] = \frac{p_{\parallel}}{\tau} \frac{\partial f_a(\tau, p_T, p_{\parallel})}{\partial p_{\parallel}}$ which characterizes the redshift of the longitudinal

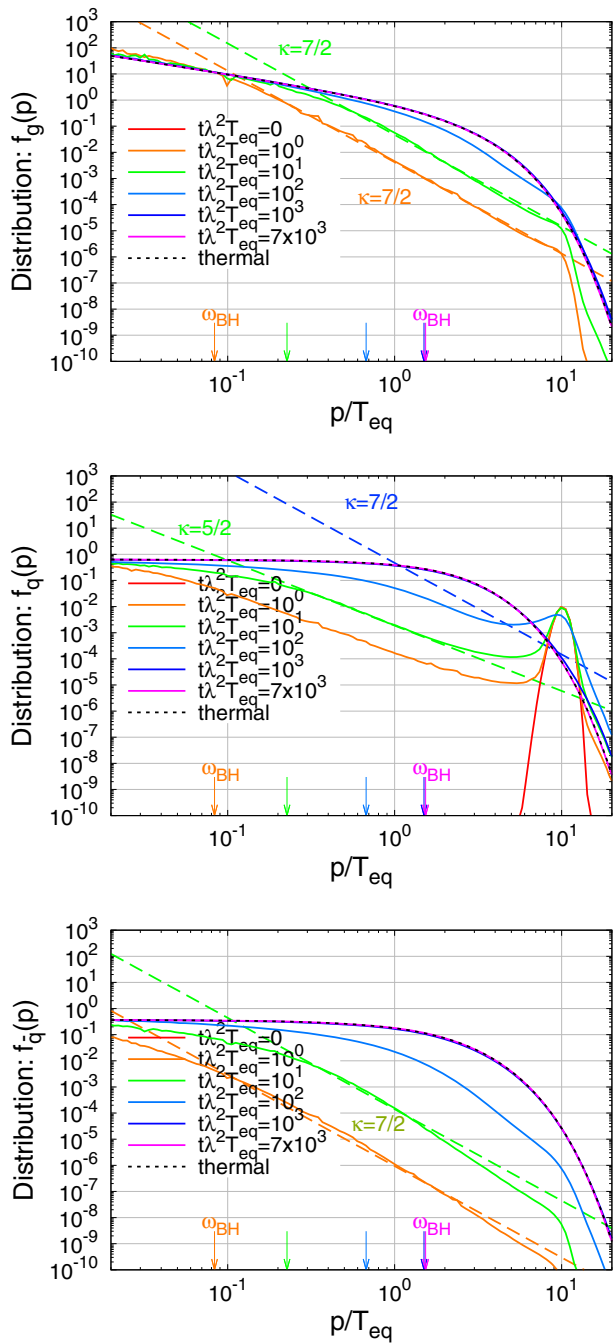


FIG. 26. Evolution of the phase-space distributions of gluons (top), quarks (middle), and antiquarks (bottom) in an *underoccupied quark system* with $\langle p \rangle_0/T_{\text{eq}} = 10$ at coupling $\lambda = 1$. Different flavors of quarks/antiquarks are assumed to be identical and the equilibrium temperature is $T_{\text{eq}} \simeq 0.98T_{\text{eff}}$. Dashed lines show the characteristic power-law dependence of the single emission LPM spectra ($\kappa = 5/2, 7/2$) and the Kolmogorov Zakharov spectra ($\kappa = 7/2$). Dotted lines show the thermal equilibrium distributions. Vertical arrows mark the Bethe-Heitler frequencies ω_{BH} .

momentum p_{\parallel} due to the longitudinal expansion, and the discretized form of the expansion term can be found in Sec. B 3.

We note that in comparison to the previous discussion of homogenous and isotropic systems, there are two important physical differences when considering plasmas which are subject to a rapid longitudinal expansion. Due to the expansion, the system will, on the one hand, become more and more dilute over the course of the evolution; on the other hand, the longitudinal expansion tends to reduce the longitudinal momenta in the local rest frame, thereby introducing an anisotropy which can persist on large timescales. We further note that momentum space anisotropic QCD plasmas are generally expected to be unstable [79–82] due to the non-Abelian analog of the Weibel instability in electrodynamics [83]. While perturbative calculations of the one-loop self-energies in momentum space anisotropic plasmas suggest the presence of instabilities, and modifications to the thermalization scenario have been worked out [35,36], sophisticated classical field simulations [40,41] point to the fact that plasma instabilities do not appear to play a

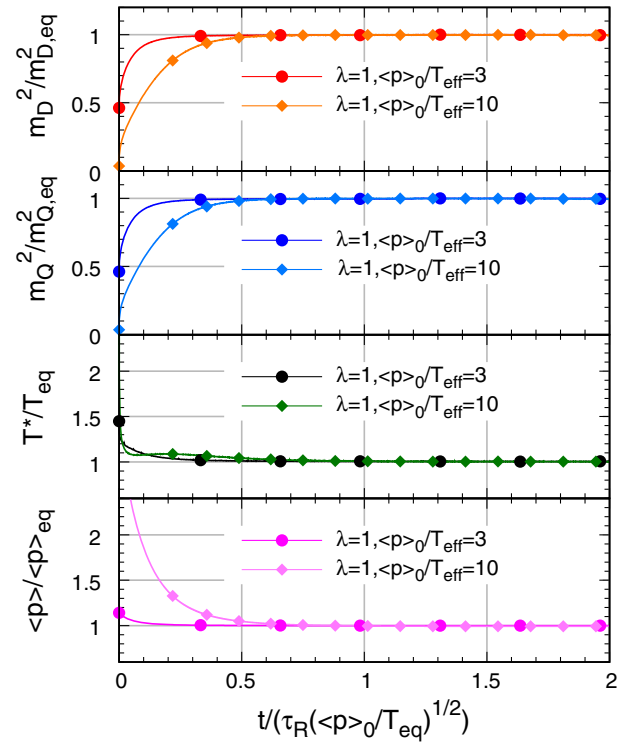


FIG. 27. Evolution of the characteristic scales $m_D^2(t)$ (red), $m_Q^2(t)$ (blue), $T^*(t)$ (green), and $\langle p \rangle$ (pink) in an *underoccupied quark system* at coupling strengths $\lambda = 1$ for different scale separations $\langle p \rangle_0/T_{\text{eq}} = 3, 10$ (darker to lighter colors/circle, diamond). Scales are normalized to their respective equilibrium values, while the evolution time t is normalized to $\tau_R \sqrt{\frac{p_0}{T_{\text{eq}}}}$ in order to take into account the leading dependence on the initial energy $\langle p \rangle_0$.

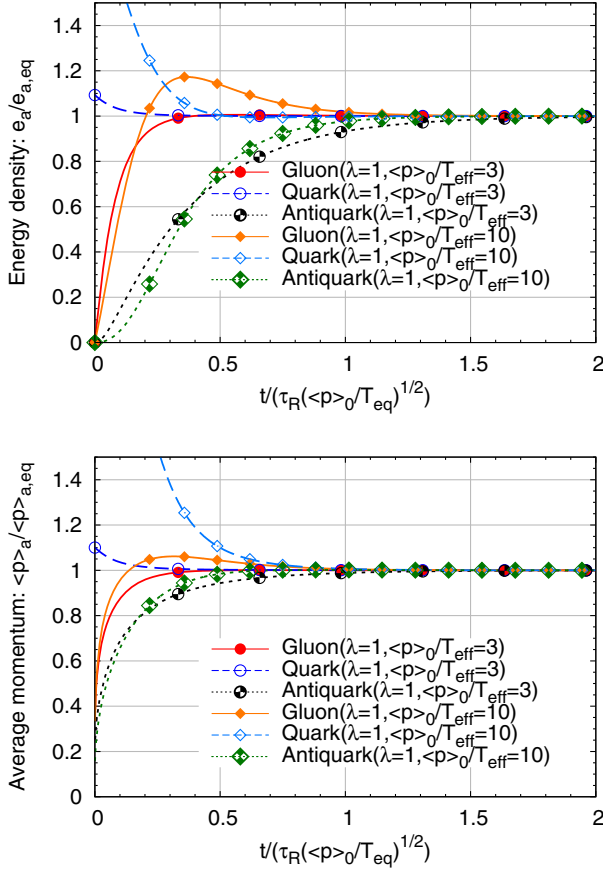


FIG. 28. Evolution of the energy densities (top) and average momenta (bottom) of quarks (dashed line/open symbol), antiquarks (dotted line/crossed symbol), and gluons (solid line/closed symbol) in an *underoccupied quark system* at coupling strengths $\lambda = 1$ for different scale separations $\langle p \rangle_0/T_{\text{eq}} = 3, 10$ (circle, diamond). In the figure, energy densities and average momenta are normalized to their respective equilibrium values, while the evolution time t is normalized to $\tau_R \sqrt{\frac{p_0}{T_{\text{eq}}}}$ in order to take into account the leading dependence on the initial energy $\langle p \rangle_0$.

dominant role in the nonequilibrium evolution of the system beyond very early times. Despite some recent progress [84], it is currently not established how to properly include these effects into an effective kinetic description, and we will therefore follow previous works [6,50,85] and neglect the effects of plasma instabilities, by resorting to the isotropic description of screening discussed in Sec. II B 1.

While the kinetic evolution of homogeneous and isotropic systems is governed by the collision rates $\sim g^4 T^*$ of elastic and inelastic collisions, the longitudinal expansion rate $\sim 1/\tau$ provides an additional timescale which dominates the kinetic evolution at early times. Even though the expansion rate is naively divergent in the limit $\tau \rightarrow 0$, it is important to point out that the effective kinetic description only becomes applicable on a time-scale $\tau_0 \sim 1/Q_s$ corresponding to the formation time of

hard particles in the system, where Q_s is the typical momentum of quarks and gluons in the initial state. When describing the nonequilibrium evolution of long-expanding systems, we will therefore initialize the QCD kinetic simulations at a finite proper time $\tau_0 \sim 1/Q_s$ and consider the subsequent nonequilibrium evolution toward equilibrium.

With regards to the initial conditions for the phase-space distributions of quarks and gluons at initial time τ_0 , we follow previous works [50] and consider the following initial conditions:

$$f_g(\tau_0, p_T, p_{\parallel}) = f_g^0 \frac{Q_0}{\sqrt{p_T^2 + \xi_0^2 p_{\parallel}^2}} e^{-\frac{2(p_T^2 + \xi_0^2 p_{\parallel}^2)}{3Q_0^2}},$$

$$f_{q_f/\bar{q}_f}(\tau_0, p_T, p_{\parallel}) = f_{q_f/\bar{q}_f}^0 \frac{\sqrt{p_T^2 + p_{\parallel}^2}}{\sqrt{p_T^2 + \xi_0^2 p_{\parallel}^2}} e^{-\frac{2(p_T^2 + \xi_0^2 p_{\parallel}^2)}{3Q_0^2}}, \quad (47)$$

inspired by color-glass condensate calculations of the gluon spectra, where $Q_0 = 1.8Q_s$ denotes the initial energy scale, $\xi_0 = 10$ characterizes the initial momentum space anisotropy and f_i^0 denotes the typical phase-space occupancy for the different particle species $i = g, u, \bar{u}, d, \bar{d}, s, \bar{s}$. Since parton distributions at small x are highly gluon dominated, gluons are copiously produced in high-energy collisions, and we will typically consider $f_g^0 \sim 1/\alpha_s$. Since initial quarks can be produced either from the stopping of valence quarks or via the production of quark-antiquark pairs, we consider

$$f_u^0 = \frac{7}{15} f_{\text{val}}^0 + \frac{1}{6} f_{\text{split}}^0, \quad f_{\bar{u}}^0 = \frac{1}{6} f_{\text{split}}^0,$$

$$f_d^0 = \frac{8}{15} f_{\text{val}}^0 + \frac{1}{6} f_{\text{split}}^0, \quad f_{\bar{d}}^0 = \frac{1}{6} f_{\text{split}}^0,$$

$$f_s^0 = \frac{1}{6} f_{\text{split}}^0, \quad f_{\bar{s}}^0 = \frac{1}{6} f_{\text{split}}^0, \quad (48)$$

where f_{val}^0 and f_{split}^0 represent the contributions from valence stopping and quark-antiquark pair production, and we have implemented $(f_u - f_{\bar{u}})/(f_d - f_{\bar{d}}) = 7/8$ in Eq. (48) to represent the different valence quark fractions taking into account a proton to neutron fraction $n_p/(n_p + n_n) \approx 0.4$ in a heavy nuclei. We present a compact summary of all the simulations performed in Table II, where we list the corresponding initial conditions, and coupling strength λ , along with extracted values of the ratio $(\mu_B/T)_{\text{eq}}$ at late times and the shear-viscosity $\eta T_{\text{eff}}/(e + p)$ as discussed below.

A. Early and late time behavior of e and Δn_f

Before we present the results of our QCD kinetic theory simulations, it is insightful to analyze the evolution

TABLE II. Summary of the parametrization τ_0 , f_g^0 , f_{val}^0 , f_{split}^0 , ξ_0 , coupling λ , extracted dimensionless coefficients $\eta T_{\text{eff}}/(e+p)$, and baryon chemical potentials $(\mu_B/T)_{\text{eq}}$.

| $Q_s \tau_0$ | f_g^0 | f_{val}^0 | f_{split}^0 | ξ_0 | λ | $(\frac{\eta T_{\text{eff}}}{e+p})$ | $(\frac{\mu_B}{T})_{\text{eq}}$ | Figures |
|--------------|---------|--------------------|----------------------|---------|-----------|-------------------------------------|---------------------------------|----------------|
| 5.5 | 1.068 | 0 | 0 | 10 | 10 | 1.00 | 0 | 29, 30, 31, 32 |
| 5.5 | 0.598 | 1.068 | 0 | 10 | 10 | 1.03 | 1.31 | 29, 30, 31, 32 |
| 12.5 | 0.363 | 1.602 | 0 | 10 | 10 | 1.08 | 2.38 | 29, 30, 31, 32 |
| 15.0 | 1.068 | 0 | 0 | 10 | 5 | 2.73 | 0 | 29, 32 |
| 15.0 | 0.598 | 1.068 | 0 | 10 | 5 | 2.80 | 1.31 | 29, 32 |
| 34.5 | 0.363 | 1.602 | 0 | 10 | 5 | 2.96 | 2.38 | 29, 32 |
| 2.0 | 1.068 | 0 | 0 | 10 | 20 | 0.39 | 0 | 29, 32 |
| 2.0 | 0.598 | 1.068 | 0 | 10 | 20 | 0.40 | 1.31 | 29, 32 |
| 4.5 | 0.363 | 1.602 | 0 | 10 | 20 | 0.42 | 2.38 | 29, 32 |
| 5.5 | 0.950 | 0 | 0.269 | 10 | 10 | 1.00 | 0 | 31 |
| 5.5 | 0.833 | 0 | 0.534 | 10 | 10 | 1.00 | 0 | 31 |
| 5.5 | 0.598 | 0 | 1.068 | 10 | 10 | 1.00 | 0 | 31 |
| 5.5 | 0.363 | 0 | 1.602 | 10 | 10 | 1.00 | 0 | 31 |
| 5.5 | 0 | 0 | 2.427 | 10 | 10 | 1.00 | 0 | 31 |
| 5.5 | 0.598 | 1.068 | 0.359 | 10 | 10 | 1.03 | 1.19 | 31 |
| 5.5 | 0.598 | 1.068 | 1.077 | 10 | 10 | 1.02 | 1.01 | 31 |

of the energy-momentum tensor and conserved currents at early and late times. Due to the longitudinal expansion, the net-charge Δn_f densities of all flavors are diluted according to

$$\partial_\tau \Delta n_f = -\frac{\Delta n_f}{\tau}, \quad (49)$$

indicating that throughout the evolution the net-charge density per unit rapidity $\tau \Delta n_f(\tau) = (\tau \Delta n_f)_0$ remains constant. Similarly, the energy density of a homogenous system undergoing a boost-invariant longitudinal expansion decreases according to

$$\partial_\tau e = -\frac{e + p_L}{\tau}, \quad (50)$$

where in addition to the trivial dilution, the second term on the right-hand side characterizes the work performed against the longitudinal expansion [86,87], which is proportional to the longitudinal pressure $p_L = \tau^2 T^{\eta\eta}$ given by

$$p_L = \int \frac{d^2 p_T}{(2\pi)^2} \frac{dp_\parallel}{2\pi} \frac{p_\parallel^2}{\sqrt{p_T^2 + p_\parallel^2}} \sum_i \nu_i f_i(\tau, p_T, p_\parallel), \quad (51)$$

in QCD kinetic theory. Since at early times the system is rapidly expanding in the longitudinal direction, it is unable to maintain a sizable longitudinal pressure. Early on, one therefore has $p_L \ll e$, such that initially the energy per unit rapidity $\tau e(\tau) = (\tau e)_0$ remains approximately constant. Since initially $\tau \Delta n_f(\tau) = (\tau \Delta n_f)_0$ and $\tau e(\tau) = (\tau e)_0$ are both constant, this further implies that,

for finite density systems, the energy per baryon remains approximately constant at early times.

Evidently, this is sharp contrast to the behavior at asymptotically late times, where for an equilibrated QCD plasma the longitudinal pressure becomes $p_L = e/3$ such that $\tau^{4/3} e(\tau) = (\tau^{4/3} e(\tau))_\infty$ approaches a constant and the energy per baryon decreases $\propto \tau^{-1/3}$. By considering the evolution of $e(\tau)$ along with the ratios of $\Delta n_f(\tau)/(e(\tau))^{3/4}$ one then finds that the quantity $\tau^{1/3} T_{\text{eff}}(\tau) = (\tau^{1/3} T_{\text{eff}})_\infty$ and the ratios of the various chemical potentials to the temperature $\mu_{f,ldm}(\tau)/T_{ldm}(\tau) = (\mu_f/T)_\infty$ become constant at asymptotically late times.

B. Pressure isotropization and kinetic equilibration

We now turn to the presentation of our QCD kinetic theory results and first analyze the evolution of the bulk anisotropy, characterized by the ratio of the longitudinal pressure p_L to the energy density e shown in Fig. 29. Different curves in Fig. 29 show the results for p_L/e at zero and finite net-baryon density⁶ as a function of the scaling variable $\tilde{\omega} = (e+p)\tau/(4\pi\eta)$, which at zero net-baryon density ($\mu_B/T = 0$) corresponds to the familiar expression $\tilde{\omega} = T\tau/(4\pi\eta/s)$ employed in previous works [12,28].

Starting from early times, where the system is dominated by the rapid longitudinal expansion and highly anisotropic ($p_L \ll e$), the longitudinal pressure

⁶Note that instead of characterizing the amount of net-baryon density in terms of the initial energy per baryon $(e\tau)_0/(\Delta n_B \tau)_0$, the curves at different densities are labeled in terms of the asymptotic ratio of $(\mu_B/T)_{\text{eq}}$ extracted from our simulations, and we refer to Table II for the corresponding initial state parameters.

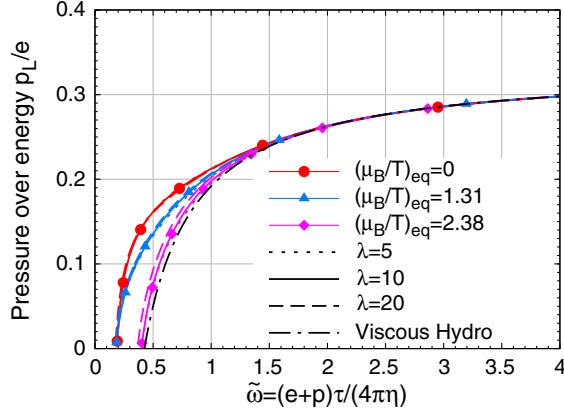


FIG. 29. Nonequilibrium evolution of longitudinal pressure p_L over energy density e for different chemical potentials $(\mu_B/T)_{\text{eq}} \approx 0, 1.31, 2.38$ (red/circle, blue/triangle, pink/diamond) and coupling strength $\lambda = 5, 10, 20$ (dotted, solid, dashed lines) as a function of the scaled time variable $\tilde{\omega} = (e+p)\tau/(4\pi\eta)$. The dash-dotted curve shows the asymptotic behavior of p_L/e in viscous hydrodynamic.

continuously rises as kinetic interactions become increasingly important. Despite the rapid increase of p_L/e at early times, the system remains significantly anisotropic throughout the entire evolution shown in Fig. 29 and only approaches an isotropic equilibrium state on much larger timescales.

Nevertheless, starting around $\tilde{\omega} \gtrsim 1$ the approach toward equilibrium is described by viscous hydrodynamics, where to leading order in the gradient expansion, the longitudinal pressure is given by

$$\frac{p_L}{e} = \frac{1}{3} - \frac{16}{9} \frac{\eta}{(e+p)\tau}. \quad (52)$$

Expressing the nonequilibrium correction in terms of the dimensionless ratio $\eta T_{\text{eff}}/(e+p)$ which at zero density reduces to the familiar η/s , the pressure evolution in hydrodynamics is determined by

$$\frac{p_L}{e} = \frac{1}{3} - \frac{4}{9\pi} \left(\frac{\eta T_{\text{eff}}}{e+p} \right) \frac{4\pi}{\tau T_{\text{eff}}}. \quad (53)$$

By analyzing the late time behavior of the different curves, we can then extract the transport coefficient $\eta T_{\text{eff}}/(e+p)$, whose values are indicated in Table II. We note that although in principle $\eta T_{\text{eff}}/(e+p)$ can exhibit a dependence on the chemical potentials μ_f/T , we find that in the relevant range of μ_B/T for our simulations, the extracted values only differ by about ten percent, which *a posteriori* justifies its treatment as a constant when defining the scaling variable $\tilde{\omega}$ and extracting the values of $\eta T_{\text{eff}}/(e+p)$ based on the late

time behavior in Eq. (53).⁷ When expressed in terms of the macroscopic scaling variable $\tilde{\omega}$, one also observes that the evolution of p_L/e is rather insensitive to the microscopic coupling strength $\lambda = 5, 10, 20$ in Fig. 29, as discussed in detail in [50] for charge neutral plasmas.

By taking into account the (small) $\frac{\mu_B}{T}$ dependence of the transport coefficient $\eta T_{\text{eff}}/(e+p)$, the results for p_L/e in Fig. 29 are presented such that they all exhibit the same hydrodynamic behavior in Eq. (53) at late times $\tilde{\omega} \gtrsim 1$ which is indicated by a black dashed line. However, by comparing the results for different net-baryon densities $(\mu_B/T)_{\text{eq}}$, one clearly observes that at early times $\tilde{\omega} \lesssim 1$ the isotropization of the pressure proceeds more slowly for systems with a larger net-baryon density. We will show shortly that this feature can be understood by considering the fact that more baryon rich systems necessarily feature a larger abundance of quarks as compared to the initially gluon dominated zero density systems, which along with the less efficient isotropization of quark and antiquark distributions leads to a slower buildup of the longitudinal pressure in the system.

C. Kinetic and chemical equilibration of light flavors

Beyond the evolution of the pressure anisotropy, which provides an estimate of the range of applicability of a hydrodynamic description of the QGP, it is also insightful to consider the evolution of the phase-space densities of gluons, quarks, and antiquarks to scrutinize the underlying microscopic dynamics. Our results are compactly summarized in Fig. 30, where we present the evolution of the various distributions for three different values of the net-baryon density $(\mu_B/T)_{\text{eq}} = 0$ (upper panel), $(\mu_B/T)_{\text{eq}} = 1.31$ (middle panel), and $(\mu_B/T)_{\text{eq}} = 2.38$ (lower panel). Different rows in each panel correspond to the distributions for different particle species, while different columns show the distributions at four different times, corresponding to the initial conditions in the first column, and $\tilde{\omega} = 0.5, 1.0,$ and 1.5 in the second, third, and fourth columns. We focus on the evolution of the phase-space distributions of gluons (g), up-quarks (u), up-antiquarks (\bar{u}), and strange quarks (s), noting that the distributions of strange and antistrange quarks are identical $f_s = f_{\bar{s}}$, and that up- and down-quark distributions exhibit essentially the same features.

⁷We employ the values of $\eta T/(e+p)$ extracted at the final equilibrium ratio of $(\mu_B/T)_{\text{eq}}$. Since e and n exhibit a different time dependence, the value of μ_B/T , defined by the Landau matching conditions, changes during the evolution of the system, such that in principle one assesses slightly different values of $\eta T/(e+p)$ as a function of μ_B/T at different times. Evidently, this is a much smaller effect and is also significantly more complicated to take into account in the analysis, which is the reason that we opted for the simpler choice of considering $\eta T/(e+p)$ as a function of $(\mu_B/T)_{\text{eq}}$.

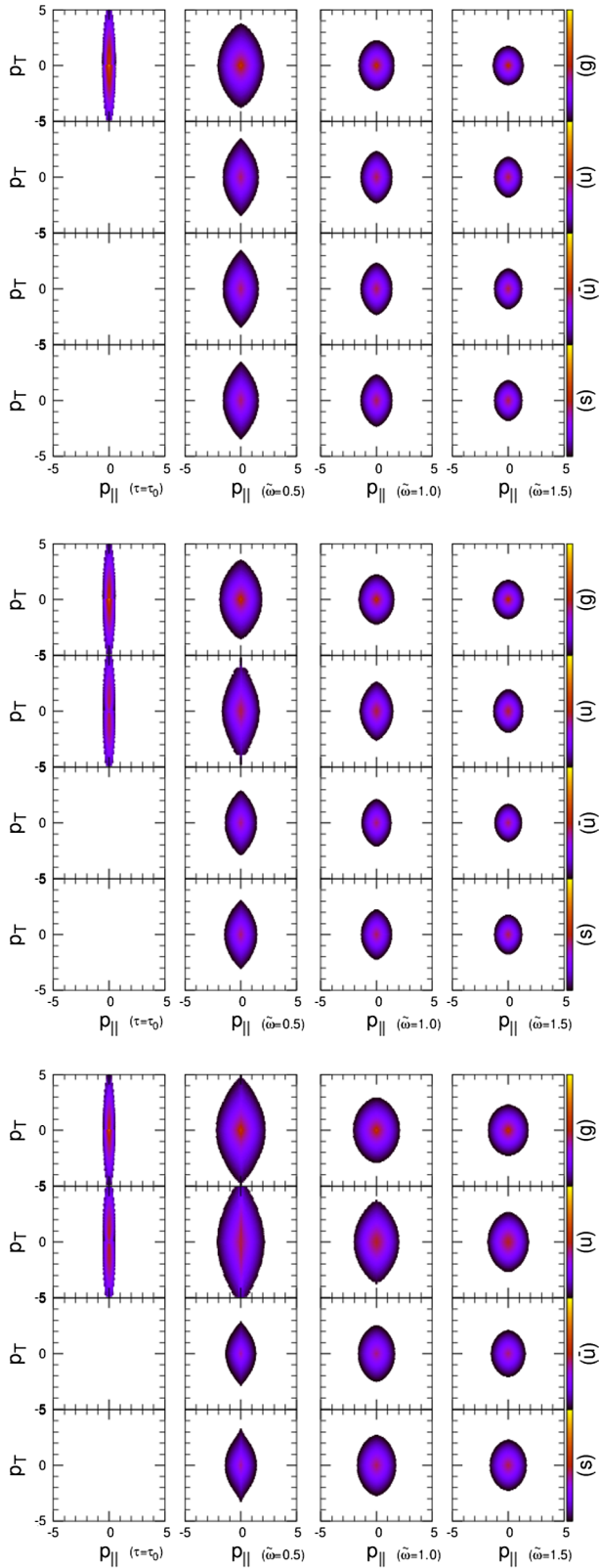


FIG. 30. Evolution of the two-dimensional phase-space distributions $f(\tau, p_T, p_{||})$ of gluons (g), up quarks (u), antiup quarks (\bar{u}) at times $\tau = \tau_0$, $\bar{\omega} = 0.5$, $\bar{\omega} = 1.0$, $\bar{\omega} = 1.5$ for different chemical potentials $(\mu_B/T)_{\text{eq}} = 0$ (top), 1.31 (middle), 2.38 (bottom) at coupling strength $\lambda = 10$.

Starting from the behavior at zero net-baryon density $(\mu_B/T)_{\text{eq}} = 0$ depicted in the top panel, where we assume that there are initially no quarks present in the system, one finds that quark/antiquarks of all flavors are democratically produced and naturally inherit the anisotropy of the gluon distribution. However, the quark/antiquark distributions at intermediate stages of the evolution $\bar{\omega} = 0.5, 1.0$ exhibit a larger degree of anisotropy as compared to the gluon distribution, indicating the slower isotropization of quarks/antiquarks. By considering the underlying microscopic processes in the bottom-up scenario [34], one expects the isotropization of the gluon distribution to be driven by the radiative decay of hard gluons due to collinear $g \rightarrow gg$ and $g \rightarrow q\bar{q}$ processes, followed by $gg \rightarrow gg$, $gq \rightarrow gq$, and $g\bar{q} \rightarrow g\bar{q}$ elastic scatterings which isotropize the momentum distribution of soft gluons, whereas quarks/antiquarks are predominantly produced via collinear $g \rightarrow q\bar{q}$ splittings and to a lesser extent by $gg \rightarrow q\bar{q}$ elastic conversions, with the subsequent isotropization of soft quarks/antiquarks due to $qq \rightarrow qq$, $\bar{q}q \rightarrow \bar{q}q$, $q\bar{q} \rightarrow q\bar{q}$, $\bar{q}\bar{q} \rightarrow \bar{q}\bar{q}$, and $q\bar{q} \rightarrow q\bar{q}$ elastic scattering processes. Based on the different color factors for the elastic scattering processes involving quarks and gluons, e.g., $|M_{gg}^{gg}|^2 \propto C_A^2$ and $|M_{gq}^{gq}|^2 \propto C_F C_A$ (see Table I), it is then natural to expect a faster isotropization of the gluon distribution. Since Bose enhancement and Fermi blocking also play a role for the population of the soft sector, one also notices clear differences between quark/antiquark and gluon distributions at very low momenta.

When considering the evolution of the phase-space distributions at finite net-baryon density, shown in the central and bottom panels of Fig. 30 for $(\mu_B/T)_{\text{eq}} = 1.31$ and 2.38, one finds that the overall behavior of the phase-space distributions at different times is rather similar to the zero density case. However, at finite density, the nonzero values of the conserved u and d charges lead to an overabundance of up- and down-quarks as compared to antiquarks of the same flavor. Since at larger net-baryon density, u and d quarks carry a significant fraction of the initial energy, the larger degree of anisotropy of the quark distribution then manifests itself at the level of the bulk anisotropy p_L/e , seen in Fig. 29.

Besides the dynamics of the up and down flavors, it is also interesting to compare the evolution of the strange quark distribution (f_s) at zero and finite density. While at zero density strange quarks can be efficiently produced via inelastic $g \rightarrow q\bar{q}$ and elastic $gg \rightarrow q\bar{q}$ conversions, the direct production of $s\bar{s}$ -pairs from u and d quarks is only possible through quark/antiquark annihilation $q\bar{q} \rightarrow s\bar{s}$, which at finite density is suppressed due to the lack of antiquarks. By comparing the results for f_s in the upper and lower panels of Fig. 30, one therefore finds that the strangeness production at finite density is delayed until $\bar{\omega} \sim 1$, when strangeness is efficiently produced from inelastic $g \rightarrow q\bar{q}$ and elastic $gg \rightarrow q\bar{q}$ conversions.

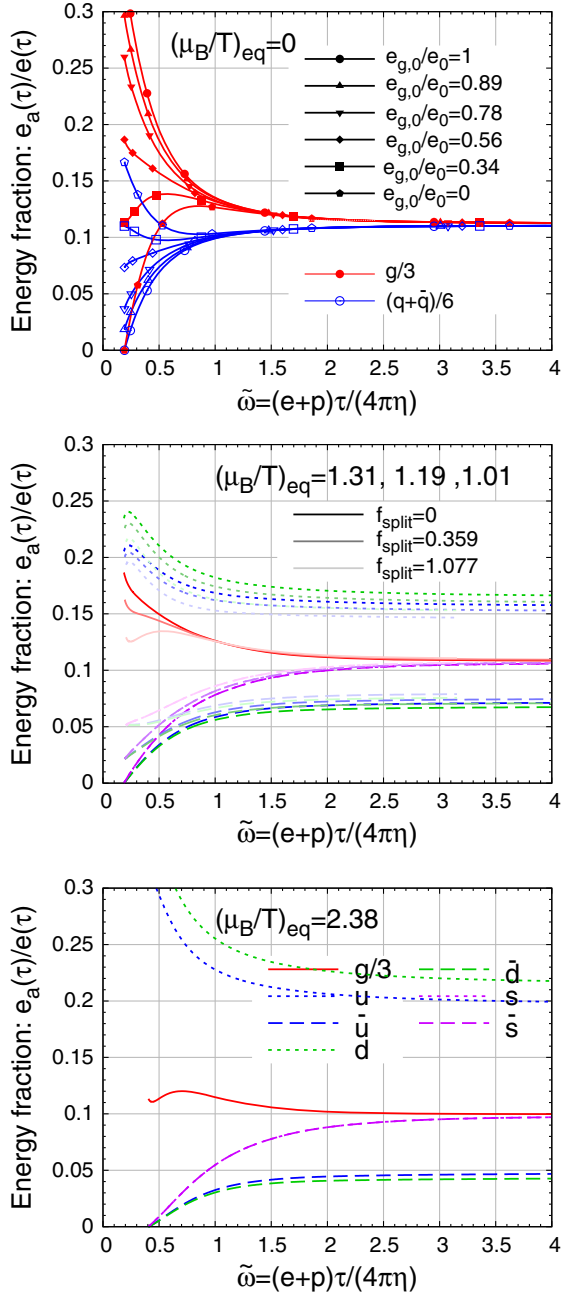


FIG. 31. Evolution of fraction of energy carried by gluons (g), up (u), antiup (\bar{u}), down (d), antidown (\bar{d}), strange (s), and antistrange (\bar{s}) quarks as a function of the scaled time variable $\tilde{w} = (e+p)\tau/(4\pi\eta)$. The top panel shows evolution of $(\mu_B/T)_{\text{eq}} = 0$ systems with initially different gluon fractions. The middle panel shows evolution of $(\mu_B/T)_{\text{eq}} \neq 0$ systems with different splitting contributions f_{split} . The bottom panel shows evolution of the energy fraction of each species for large density system $(\mu_B/T)_{\text{eq}} = 2.38$ (cf. Table II).

Next in order to further analyze the chemical composition of the QGP, we follow [6] and investigate the fraction of energy $e_a(\tau)/e(\tau)$ carried by each individual species a during the nonequilibrium evolution. Our results for this

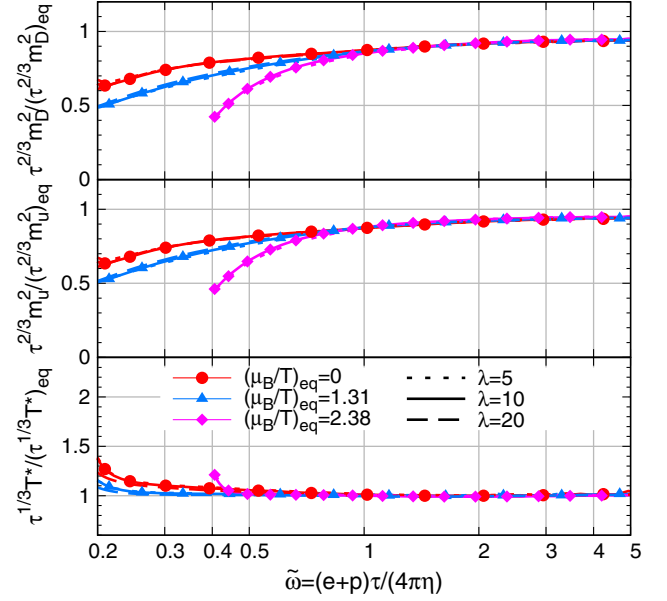


FIG. 32. Evolution of the characteristic scales $\tau^{2/3} m_D^2(\tau)$ (top), $\tau^{2/3} m_u^2(\tau)$ (middle), and $\tau^{1/3} T^*(\tau)$ (bottom) normalized to their asymptotic equilibrium values, as a function of the scaled time variable $\tilde{w} = \frac{(e+p)\tau}{4\pi\eta}$ for different chemical potentials $(\mu_B/T)_{\text{eq}} = 0, 1.31, 2.38$ (red circle, blue triangle, pink diamond) for $\lambda = 5, 10, 20$ (dotted, solid, dashed curves).

quantity, $e_a(\tau)/e_{\text{total}}(\tau)$, are presented in Fig. 31 as a function of the scaling variable \tilde{w} . Different panels in Fig. 31 show the results for different net-baryon densities, with $(\mu_B/T)_{\text{eq}} = 0$ in the top panel, $(\mu_B/T)_{\text{eq}} = 1.31, 1.19, 1.01$ in the central panel, and $(\mu_B/T)_{\text{eq}} = 2.38$ in the bottom panel, while different solid, dashed, and dotted curves in each panel correspond to the result obtained by varying the chemical composition of the initial state (see Table II). Starting with the evolution at zero net-baryon density, we find that for gluon dominated initial conditions ($e_{g,0}/e_0 = 1$) a large part of the initial energy of gluons is rapidly transferred to quarks and antiquarks of all flavors. Similarly for quark/antiquark dominated initial conditions at zero density ($e_{g,0}/e_0 = 0$), a rapid energy transfer from the quark to the gluon sector occurs, effectively resulting in a memory loss of the initial QGP chemistry on timescales $\tilde{w} \sim 1$. Eventually, for $\tilde{w} \gtrsim 0.5$ the zero density plasma becomes gluon dominated, before relaxing toward chemical equilibrium on timescales $\tilde{w} \sim 1-2$. Clearly, the situation is different at moderate or large net-baryon density shown in the bottom panel of Fig. 31, where u and d quarks carry the dominant fraction of the energy density throughout the evolution. Due to the fact that multiple quark/antiquark species contribute different amounts, one observes that the evolution of the chemistry of the QGP at moderate and large net-baryon density is significantly more complicated, and the approach toward equilibrium occurs on somewhat larger timescales $\tilde{w} \sim 1.5-2.5$, due to

the less efficient production of antiquarks (\bar{u}, \bar{d}) and strangeness (s, \bar{s}).

We conclude our discussion of equilibration in longitudinally expanding QCD plasmas by considering once again the evolution of the characteristic scales m_D^2 , $m_{Q,u}^2$, and T^* that govern the rates of elastic and inelastic interactions in the plasma. The time evolution of these quantities is presented in Fig. 32, where in order to account for the continuous expansion of the system we have normalized the respective quantities as $\tau^{\frac{2}{3}}m_D^2/(\tau^{\frac{2}{3}}m_D^2)_{\text{eq}}$, $\tau^{\frac{2}{3}}m_{Q,u}^2/(\tau^{\frac{2}{3}}m_{Q,u}^2)_{\text{eq}}$, and $\tau^{\frac{1}{3}}T^*/(\tau^{\frac{1}{3}}T^*)_{\text{eq}}$ such that for $\tilde{\omega} \gg 1$ all ratios approach unity. By comparing the evolution of the different curves, we find that simulation results at different coupling strengths $\lambda = 5, 10, 20$ are in good overall agreement when expressing the evolution in terms of the scaling variable $\tilde{\omega}$. While the effective temperature T^* relaxes toward its equilibrium value on timescales $\tilde{\omega} \sim 1$, the screening masses m_D^2 and m_u^2 for gluons and (up-) quarks only approach their equilibrium values at asymptotically late times, indicating residual deviations from local thermal equilibrium on the order of 10%.

VI. CONCLUSIONS

We provided a numerical implementation of the QCD kinetic description of the light flavor QCD degrees of freedom [52] to study near and far-from equilibrium dynamics of the QGP at zero and finite density of the conserved baryon number, electric charge, and strangeness. Based on the numerical solution of the kinetic equations, including all leading order elastic and inelastic interactions between gluons, quarks, and antiquarks, we exposed the general features of kinetic and chemical equilibration of nonequilibrium QCD plasmas in the perturbative regime at (asymptotically) high energies.

Generally, we find that, albeit the energy transfer between quark and gluon degrees of freedom can take a significant time, kinetic and chemical equilibration of QCD plasmas occur roughly on the same timescale. By performing detailed investigations of the evolution of the spectra and collision rates in Sec. III, we further established a microscopic understanding of different equilibration processes in QCD plasmas, which generalizes earlier results obtained in pure glue QCD [4,7,46] and QCD at zero density [8,50,85].

Specifically, for overoccupied systems, which initially feature a large number of low-energy gluons, we showed in Sec. IV A that the thermalization process proceeds via a self-similar turbulent cascade, before eventually reaching equilibrium on a timescale $\sim 4\pi\eta/s/T_{\text{eq}}$. Conversely, for underoccupied systems, which initially feature a small number of high-energy quarks or gluons, thermalization is achieved via the bottom-up scenario [34], with a number of interesting features regarding the role of quark and gluon degrees of freedom as discussed in Sec. IV B.

Studies of the equilibration of the QGP in a longitudinally expanding system provide the basis for a realistic matching of the initial state in heavy-ion collisions to initial conditions for the subsequent hydrodynamic evolution [32,33]. By analyzing the macroscopic evolution of the energy momentum tensor and the microscopic evolution of the phase-space distributions of quarks and gluons in Sec. V, we found that in accordance with earlier studies [6,7] viscous hydrodynamics typically becomes applicable on timescales where $(e+p)\tau/(4\pi\eta) \sim 1$; however, isotropization and strangeness production proceed more slowly for finite density systems, and we refer to [8] and our companion paper [53] for further discussions of phenomenological consequences.

We finally note that the numerical framework to solve the QCD kinetic equations presented in this paper could be extended in several regards, e.g., by including heavy flavor degrees of freedom or electroweak interactions, to study a variety of aspects regarding the early time dynamics of high-energy heavy-ion collisions and the thermalization of the early universe. Since in many applications, the relevant coupling strength can be sizable, it would also be important to extend the kinetic approach beyond leading order accuracy, as recently discussed in [88,89] for jet-medium interactions and [24,25] for transport coefficients.

ACKNOWLEDGMENTS

We thank Giuliano Giacalone, Alekski Kurkela, Aleksas Mazeliauskas, Jean-Francois Paquet, Ismail Soudi, and Derek Teaney for discussions and collaboration on related projects. We are especially grateful to Aleksas Mazeliauskas for fruitful exchanges on the numerical implementation of QCD kinetic theory. This work is supported by the Deutsche Forschungsgemeinschaft (DFG, German Research Foundation) through the Collaborative Research Center CRC-TR-2111 ‘‘Strong-Interaction matter under Extreme Conditions’’ under Project No. 315477589 TRR 211. The authors also gratefully acknowledge computing time provided by the Paderborn Center for Parallel Computing (PC2) and the National Energy Research Scientific Computing Center (NERSC), a U.S. Department of Energy Office of Science User Facility located at Lawrence Berkeley National Laboratory, operated under Contract No. DE-AC02-05CH11231.

APPENDIX A: WEIGHT FUNCTION DISCRETIZATION

1. Weighted integral: Discretization

We discretize the Boltzmann equation Eq. (6) with the *weighted integral* of a function $\mathcal{F}(\vec{p})$ [particle phase-space distribution $\mathcal{F}(\vec{p}) = f(\vec{p})$ or collision integral $\mathcal{F}(\vec{p}) = C[f](\vec{p})$] transforming from the continuous domain $\Omega_{p,\theta,\phi} = \{(p, \theta, \phi) | p \in \mathbb{R}^+; \theta \in [0, \pi]; \phi \in [0, 2\pi)\}$ to a

discretized domain $\mathbb{N}_{p,\theta,\phi}^3 = \{(i_p, j_\theta, k_\phi) | i_p = 0, \dots, N_p - 1; j_\theta = 0, \dots, N_\theta - 1; k_\phi = 0, \dots, N_\phi - 1\}$.

The weighted integral of distribution function $f(\vec{p})$ reads

$$n(i_p, j_\theta, k_\phi) = \int \frac{d^3 p}{(2\pi)^3} w_i^{(p)}(p) w_j^{(\theta)}(\theta) w_k^{(\phi)}(\phi) f(\vec{p}), \quad (\text{A1})$$

where $w_i^{(p)}(p)$, $w_j^{(\theta)}(\theta)$, and $w_k^{(\phi)}(\phi)$ are weight functions satisfying a *completeness relation*

$$\sum_{i \in \mathbb{N}_x} w_i^{(x)}(x) = \chi_{\Omega_x}(x) = \begin{cases} 1, & x \in \Omega_x \\ 0, & x \notin \Omega_x \end{cases} \quad (\text{A2})$$

with $\chi_{\Omega_x}(x) : \Omega_x \rightarrow \mathbb{Z}_2$ the indicator function on domain Ω_x . The completeness relation ensures the summation of weighted integral $n(i_p, j_\theta, k_\phi)$ to be the total number of specific particle

$$\sum_{(i_p, j_\theta, k_\phi)} n(i_p, j_\theta, k_\phi) = \int \frac{d^3 p}{(2\pi)^3} f(\vec{p}). \quad (\text{A3})$$

The weight functions satisfying completeness relation Eq. (A2) can be achieved by decomposing into two parts

$$w_i^{(p)}(p) = w_i^L(p) + w_i^R(p) \quad (\text{A4})$$

with left- and right-side weights

$$w_i^L(p) = \begin{cases} S_{(p)}(p) |_{p_i}^{p_{i+1}} \chi_{[p_i, p_{i+1}]}(p), & 0 \leq i \leq N_p - 2 \\ 0, & i = N_p - 1 \end{cases},$$

$$w_i^R(p) = \begin{cases} (1 - S_{(p)}(p)) |_{p_{i-1}}^{p_i} \chi_{[p_{i-1}, p_i]}(p), & 1 \leq i \leq N_p - 1 \\ 0, & i = 0 \end{cases}. \quad (\text{A5})$$

The *spectral weight* $S_{(p)}(p) |_{p_i}^{p_{i+1}}$ needs to be constructed in a form

$$S_{(p)}(p) |_{p_i}^{p_{i+1}} = \frac{y(p_{i+1}) - y(p)}{y(p_{i+1}) - y(p_i)}, \quad (\text{A6})$$

with $y(p)$ an arbitrary function of p so that $S_{(p)}(p_i) |_{p_i}^{p_{i+1}} = 1$, $S_{(p)}(p_{i+1}) |_{p_i}^{p_{i+1}} = 0$, and Eq. (A2) are satisfied.

2. Sum rules

Indeed, the above function $y(p \in [p_i, p_{i+1}])$ can be reversely expressed with the left and right weights

$$y(p \in [p_i, p_{i+1}]) = w_i^L(p) y(p_i) + w_{i+1}^R(p) y(p_{i+1}), \quad (\text{A7})$$

which yields a *sum rule*

$$\sum_{i=0}^{N_p-1} w_i^{(p)}(p) y(p_i) = y(p) \quad (\text{A8})$$

for $p \in [p_{\min}, p_{\max}]$.

Specifically, we work with a proper choice of the functions for p , $\cos(\theta)$, and ϕ ,

$$y_p(p) = p, \quad y_\theta(\theta) = \cos(\theta), \quad y_\phi(\phi) = 1 \quad (\text{A9})$$

that provides the way to evaluate energy and longitudinal momentum of the particle in discretized form, following the definition of weighted integral Eq. (A1), completeness relation Eq. (A2), and sum rule Eq. (A8),

$$\sum_{(i_p, j_\theta, k_\phi)} p_i n(i_p, j_\theta, k_\phi) = \int \frac{d^3 p}{(2\pi)^3} p f(\vec{p}),$$

$$\sum_{(i_p, j_\theta, k_\phi)} p_i \cos(\theta_j) n(i_p, j_\theta, k_\phi) = \int \frac{d^3 p}{(2\pi)^3} p \cos(\theta) f(\vec{p}) \quad (\text{A10})$$

with $(p, \theta, \phi) \in \Omega_{p,\theta,\phi}$. Their weighted functions are

$$w_i^{(p)}(p) = \left[\frac{p_{i+1} - p}{p_{i+1} - p_i} \chi_{[p_i, p_{i+1}]}(p) + \frac{p - p_{i-1}}{p_i - p_{i-1}} \chi_{[p_{i-1}, p_i]}(p) \right],$$

$$w_j^{(\theta)}(\theta) = \left[\frac{\cos(\theta_{j+1}) - \cos(\theta)}{\cos(\theta_{j+1}) - \cos(\theta_j)} \chi_{[\theta_j, \theta_{j+1}]}(\theta) + \frac{\cos(\theta) - \cos(\theta_{j-1})}{\cos(\theta_j) - \cos(\theta_{j-1})} \chi_{[\theta_{j-1}, \theta_j]}(\theta) \right],$$

$$w_k^{(\phi)}(\phi) = \chi_{[\phi_k, \phi_{k+1}]}(\phi). \quad (\text{A11})$$

3. Weighted sum: Continuation

We Taylor expand $f(\vec{p})$ around the points (p_i, θ_j, ϕ_k) and use the nearest grid points to reconstruct the phase-space distribution at any specific coordinates (p, θ, ϕ) from its discretized form. Assuming

$$p^l f(\vec{p}) \approx \text{const} = \langle p^l f(\vec{p}) \rangle_{(i_p, j_\theta, k_\phi)} \quad (\text{A12})$$

holds for a neighborhood $\vec{p} \in U_{(i_p, j_\theta, k_\phi)}$ around (p_i, θ_j, ϕ_k) , the weighted integral Eq. (A1) reads

$$n(i_p, j_\theta, k_\phi) \approx \langle p^l f(\vec{p}) \rangle_{(i_p, j_\theta, k_\phi)} \int \frac{d^3 p}{(2\pi)^3} \frac{1}{p^l} W_{(i_p, j_\theta, k_\phi)}(\vec{p}) \quad (\text{A13})$$

with $W_{(i_p, j_\theta, k_\phi)}(\vec{p}) = w_i^{(p)}(p) w_j^{(\theta)}(\theta) w_k^{(\phi)}(\phi)$. Defining the *modified weighted volume* (MWV)

TABLE III. Modified weighted volume (MWV) with choice of weight functions from Eq. (A11).

| MWV | Formula | Index range |
|-------------------|--|--|
| $A_{(i_p)}^{(2)}$ | $(p_{i+1} - p_i)(3p_i^2 + 2p_i p_{i+1} + p_{i+1}^2)/12$ $(p_i - p_{i-1})(3p_i^2 + 2p_i p_{i-1} + p_{i-1}^2)/12$ $[(p_{i+1} - p_i)(3p_i^2 + 2p_i p_{i+1} + p_{i+1}^2) + (p_i - p_{i-1})(3p_i^2 + 2p_i p_{i-1} + p_{i-1}^2)]/12$ | $i = 0$ $i = N_p - 1$ $i \in [1, N_p - 2]$ |
| $A_{(i_p)}^{(1)}$ | $(p_{i+1} - p_i)(2p_i + p_{i+1})/6$ $(p_i - p_{i-1})(2p_i + p_{i-1})/6$ $(p_{i+1} - p_{i-1})(p_{i+1} + p_i + p_{i-1})/6$ | $i = 0$ $i = N_p - 1$ $i \in [1, N_p - 2]$ |
| $A_{(i_p)}^{(0)}$ | $(p_{i+1} - p_i)/2$ $(p_i - p_{i-1})/2$ $(p_{i+1} - p_{i-1})/2$ | $i = 0$ $i = N_p - 1$ $i \in [1, N_p - 2]$ |
| $A_{(j_\theta)}$ | $[\cos(\theta_{j+1}) - \cos(\theta_j)]/2$ $[\cos(\theta_j) - \cos(\theta_{j-1})]/2$ $[\cos(\theta_{j+1}) - \cos(\theta_{j-1})]/2$ | $i = 0$ $i = N_p - 1$ $i \in [1, N_p - 2]$ |

$$A_{(i_p, j_\theta, k_\phi)}^{(2-l)} = \int \frac{d^3 p}{p^l} W_{(i_p, j_\theta, k_\phi)}(\vec{p}) \quad (\text{A14})$$

we may evaluate the constant for $\vec{p} \in U_{(i_p, j_\theta, k_\phi)}$ via

$$\langle p^l f(\vec{p}) \rangle_{(i_p, j_\theta, k_\phi)} \approx \frac{(2\pi)^3 n(i_p, j_\theta, k_\phi)}{A_{(i_p, j_\theta, k_\phi)}^{(2-l)}}. \quad (\text{A15})$$

The azimuthal symmetric weight functions in Eq. (A11) gives $A_{(i_p, j_\theta, k_\phi)}^{(2-l)} = 2\pi A_{(i_p)}^{(2-l)} A_{(j_\theta)}$, and the modified weighted volumes are listed in Table III.

In order to evaluate the distribution between points in the grids, we perform an interpolation similar to Eq. (A7) for an azimuthal symmetric case so that

$$f(\vec{p} \in \Omega_p) = \sum_{(\alpha, \beta) \in \mathbb{N}_p^2} w_\alpha^{(p)}(\rho) w_\beta^{(\theta)}(\theta) \frac{(2\pi)^2 n(\alpha, \beta)}{p^l A_{(\alpha)}^{(2-l)} A_{(\beta)}}, \quad (\text{A16})$$

where the subdomain cubic $\Omega_{\vec{p}} = [p_L, p_R] \times [\theta_L, \theta_R] \times [\phi_L, \phi_R] \subset \Omega$ and the corresponding nearest grids in discretized subdomain $\mathbb{N}_{\vec{p}}^2 = \{(i_p, j_\theta) | P = p_L, p_R; \Theta = \theta_L, \theta_R; i_{p_R} - i_{p_L} = j_{\theta_R} - j_{\theta_L} = 1\}$.

APPENDIX B: DISCRETIZATION OF COLLISION INTEGRALS

1. Elastic collision integrals

a. Discretization and efficient samplings

The elastic collision integral for particle “a” with momentum \vec{p}_1 in process $a, b \rightarrow c, d$ ($p_1, p_2 \leftrightarrow p_3, p_4$) reads

$$C_a^{2 \leftrightarrow 2}[f](\vec{p}_1) = \frac{1}{2\nu_a} \frac{1}{2E_{p_1}} \sum_{cd} \int d\Pi_{2 \leftrightarrow 2} \times |\mathcal{M}_{cd}^{ab}(\vec{p}_1, \vec{p}_2 | \vec{p}_3, \vec{p}_4)|^2 F_{cd}^{ab}(\vec{p}_1, \vec{p}_2 | \vec{p}_3, \vec{p}_4), \quad (\text{B1})$$

with measure

$$d\Pi_{2 \leftrightarrow 2} = \frac{d^3 p_2}{(2\pi)^3} \frac{1}{2E_{p_2}} \frac{d^3 p_3}{(2\pi)^3} \frac{1}{2E_{p_3}} \frac{d^3 p_4}{(2\pi)^3} \frac{1}{2E_{p_4}} \times (2\pi)^4 \delta^{(4)}(p_1 + p_2 - p_3 - p_4), \quad (\text{B2})$$

$|\mathcal{M}_{cd}^{ab}(\vec{p}_1, \vec{p}_2 | \vec{p}_3, \vec{p}_4)|^2$ is the matrix element square for process “ $a, b \leftrightarrow c, d$ ” summed over spin and color for all particles, and $F_{cd}^{ab}(\vec{p}_1, \vec{p}_2 | \vec{p}_3, \vec{p}_4)$ describes the statistical factor for $a, b \leftrightarrow c, d$.

The discretized form of collision integral Eq. (B1) follows the transformation according to Eq. (A1),

$$C_a^{2 \leftrightarrow 2}[n](i_p, j_\theta, k_\phi) = \int \frac{d^2 p_1}{(2\pi)^3} W_{(i_p, j_\theta, k_\phi)}(\vec{p}_1) C_a^{2 \leftrightarrow 2}[f](\vec{p}_1) = \frac{1}{2\nu_a} \sum_{cd} \int d\Omega_{2 \leftrightarrow 2} W_{(i_p, j_\theta, k_\phi)}(\vec{p}_1) Q_{cd}^{ab}(\vec{p}_1, \vec{p}_2 | \vec{p}_3, \vec{p}_4) \quad (\text{B3})$$

with measure

$$d\Omega_{2 \leftrightarrow 2} = \frac{d^3 p_1}{(2\pi)^3} \frac{1}{2E_{p_1}} \frac{d^3 p_2}{(2\pi)^3} \frac{1}{2E_{p_2}} \frac{d^3 p_3}{(2\pi)^3} \frac{1}{2E_{p_3}} \frac{d^3 p_4}{(2\pi)^3} \frac{1}{2E_{p_4}} \times (2\pi)^4 \delta^{(4)}(p_1 + p_2 - p_3 - p_4). \quad (\text{B4})$$

and a Q -factor

$$Q_{cd}^{ab}(\vec{p}_1, \vec{p}_2 | \vec{p}_3, \vec{p}_4) = |\mathcal{M}_{cd}^{ab}(\vec{p}_1, \vec{p}_2 | \vec{p}_3, \vec{p}_4)|^2 F_{cd}^{ab}(\vec{p}_1, \vec{p}_2 | \vec{p}_3, \vec{p}_4), \quad (\text{B5})$$

which has the following symmetries:

$$Q_{dc}^{ba}(\vec{p}_2, \vec{p}_1 | \vec{p}_4, \vec{p}_3) = Q_{cd}^{ba}(\vec{p}_2, \vec{p}_1 | \vec{p}_3, \vec{p}_4) = Q_{cd}^{ab}(\vec{p}_1, \vec{p}_2 | \vec{p}_3, \vec{p}_4) = -Q_{ab}^{cd}(\vec{p}_3, \vec{p}_4 | \vec{p}_1, \vec{p}_2). \quad (\text{B6})$$

One good feature of utilizing the weight function algorithm is that the phase-space measure $d\Omega_{2\leftrightarrow 2}$ in Eq. (B4) is invariant under arbitrary exchanges between $\vec{p}_1, \vec{p}_2, \vec{p}_3, \vec{p}_4$, meaning we can maximize Monte Carlo samplings expanding the terms with those exchanges. One sampling of $\vec{p}_1, \vec{p}_2, \vec{p}_3, \vec{p}_4$ can be freely used by all

combinations, increasing the efficiency of numerical calculation and statistical accuracy. Indeed, denoting $W_1 = W_{(i_p, j_\theta, k_\phi)}(\vec{p}_1)$, $Q_{cd}^{ab}(12|34) = Q_{dc}^{ba}(\vec{p}_2, \vec{p}_1 | \vec{p}_4, \vec{p}_3)$, the discretized form of collision integral Eq. (B3) can be expanded according to the symmetry as

$$\begin{aligned} C_a^{2\leftrightarrow 2}[n](i_p, j_\theta, k_\phi) &= \frac{1}{2\nu_a} \sum_{cd} \int d\Omega_{2\leftrightarrow 2} W_1 Q_{cd}^{ab}(12|34) \\ &= \frac{1}{2\nu_a} \sum_{cd} \int d\Omega_{2\leftrightarrow 2} \frac{1}{8} [W_1(Q_{cd}^{ab}(12|34) + Q_{cd}^{ab}(12|43)) + W_2(Q_{cd}^{ab}(21|43) + Q_{cd}^{ab}(21|34)) \\ &\quad + W_3(Q_{cd}^{ab}(34|12) + Q_{cd}^{ab}(34|21)) + W_4(Q_{cd}^{ab}(43|21) + Q_{cd}^{ab}(43|12))]. \end{aligned} \quad (\text{B7})$$

As the energy density and longitudinal momentum flux can be directly evaluated from the discretized form in Eq. (A10), energy and longitudinal momentum conservation can be exactly fulfilled by the discretized form of the collision integral, as a derivative of distributions.

We take the most complicated process $q_1 \bar{q}_1 \leftrightarrow q_2 \bar{q}_2$ as an example, with other processes to follow. According to Eq. (B7), the discretization forms read:

- (1) For quark q_1 , note that $Q_{\bar{q}_2 q_2}^{q_1 \bar{q}_1}(12|34) = Q_{\bar{q}_2 q_2}^{q_1 \bar{q}_1}(12|43)$,

$$\begin{aligned} C_{q_1}^{2\leftrightarrow 2}[n](i_p, j_\theta, k_\phi) &= \frac{1}{2\nu_{q_1}} \int d\Omega_{2\leftrightarrow 2} W_1 (Q_{\bar{q}_2 q_2}^{q_1 \bar{q}_1}(12|34) + Q_{\bar{q}_2 q_2}^{q_1 \bar{q}_1}(12|34)) \\ &= \frac{1}{\nu_{q_1}} \int d\Omega_{2\leftrightarrow 2} \frac{1}{8} [W_1 (Q_{\bar{q}_2 q_2}^{q_1 \bar{q}_1}(12|34) + Q_{\bar{q}_2 q_2}^{q_1 \bar{q}_1}(12|43)) + W_2 (Q_{\bar{q}_2 q_2}^{q_1 \bar{q}_1}(21|43) + Q_{\bar{q}_2 q_2}^{q_1 \bar{q}_1}(21|34)) \\ &\quad + W_3 (Q_{\bar{q}_2 q_2}^{q_1 \bar{q}_1}(34|12) + Q_{\bar{q}_2 q_2}^{q_1 \bar{q}_1}(34|21)) + W_4 (Q_{\bar{q}_2 q_2}^{q_1 \bar{q}_1}(43|21) + Q_{\bar{q}_2 q_2}^{q_1 \bar{q}_1}(43|12))]. \end{aligned} \quad (\text{B8})$$

- (2) For antiquark \bar{q}_1 , note that $Q_{\bar{q}_2 q_2}^{\bar{q}_1 q_1}(12|34) = Q_{\bar{q}_2 q_2}^{\bar{q}_1 q_1}(21|43)$, $Q_{\bar{q}_2 q_2}^{\bar{q}_1 q_1}(12|34) = Q_{\bar{q}_2 q_2}^{\bar{q}_1 q_1}(21|34)$,

$$\begin{aligned} C_{\bar{q}_1}^{2\leftrightarrow 2}[n](i_p, j_\theta, k_\phi) &= \frac{1}{2\nu_{\bar{q}_1}} \int d\Omega_{2\leftrightarrow 2} W_1 (Q_{\bar{q}_2 q_2}^{\bar{q}_1 q_1}(12|34) + Q_{\bar{q}_2 q_2}^{\bar{q}_1 q_1}(12|34)) \\ &= \frac{1}{\nu_{\bar{q}_1}} \int d\Omega_{2\leftrightarrow 2} \frac{1}{8} [W_1 (Q_{\bar{q}_2 q_2}^{\bar{q}_1 q_1}(21|43) + Q_{\bar{q}_2 q_2}^{\bar{q}_1 q_1}(21|34)) + W_2 (Q_{\bar{q}_2 q_2}^{\bar{q}_1 q_1}(12|34) + Q_{\bar{q}_2 q_2}^{\bar{q}_1 q_1}(12|43)) \\ &\quad + W_3 (Q_{\bar{q}_2 q_2}^{\bar{q}_1 q_1}(43|21) + Q_{\bar{q}_2 q_2}^{\bar{q}_1 q_1}(43|12)) + W_4 (Q_{\bar{q}_2 q_2}^{\bar{q}_1 q_1}(34|12) + Q_{\bar{q}_2 q_2}^{\bar{q}_1 q_1}(34|21))]. \end{aligned} \quad (\text{B9})$$

- (3) For quark q_2 , note that $Q_{\bar{q}_1 q_1}^{q_2 \bar{q}_2}(12|34) = -Q_{\bar{q}_1 q_1}^{q_2 \bar{q}_2}(34|12)$, $Q_{\bar{q}_1 q_1}^{q_2 \bar{q}_2}(12|34) = -Q_{\bar{q}_1 q_1}^{q_2 \bar{q}_2}(43|12)$,

$$\begin{aligned} C_{q_2}^{2\leftrightarrow 2}[n](i_p, j_\theta, k_\phi) &= \frac{1}{2\nu_{q_2}} \int d\Omega_{2\leftrightarrow 2} W_1 (Q_{\bar{q}_1 q_1}^{q_2 \bar{q}_2}(12|34) + Q_{\bar{q}_1 q_1}^{q_2 \bar{q}_2}(12|34)) \\ &= \frac{1}{\nu_{q_2}} \int d\Omega_{2\leftrightarrow 2} \frac{1}{8} [-W_1 (Q_{\bar{q}_1 q_1}^{q_2 \bar{q}_2}(34|12) + Q_{\bar{q}_1 q_1}^{q_2 \bar{q}_2}(43|12)) - W_2 (Q_{\bar{q}_1 q_1}^{q_2 \bar{q}_2}(43|21) + Q_{\bar{q}_1 q_1}^{q_2 \bar{q}_2}(34|21)) \\ &\quad - W_3 (Q_{\bar{q}_1 q_1}^{q_2 \bar{q}_2}(12|34) + Q_{\bar{q}_1 q_1}^{q_2 \bar{q}_2}(21|34)) - W_4 (Q_{\bar{q}_1 q_1}^{q_2 \bar{q}_2}(21|43) + Q_{\bar{q}_1 q_1}^{q_2 \bar{q}_2}(12|43))]. \end{aligned} \quad (\text{B10})$$

(4) For antiquark \bar{q}_2 , note that $Q_{\bar{q}_1\bar{q}_1}^{\bar{q}_2q_2}(12|34) = -Q_{q_2\bar{q}_2}^{q_1\bar{q}_1}(43|21)$, $Q_{\bar{q}_1\bar{q}_1}^{\bar{q}_2q_2}(12|34) = -Q_{q_2\bar{q}_2}^{q_1\bar{q}_1}(34|21)$,

$$\begin{aligned} C_{\bar{q}_2}^{2\leftrightarrow 2}[n](i_p, j_\theta, k_\phi) &= \frac{1}{2\nu_q} \int d\Omega_{2\leftrightarrow 2} W_1(Q_{\bar{q}_1\bar{q}_1}^{\bar{q}_2q_2}(12|34) + Q_{\bar{q}_1\bar{q}_1}^{\bar{q}_2q_2}(12|34)) \\ &= \frac{1}{\nu_q} \int d\Omega_{2\leftrightarrow 2} \frac{1}{8} [-W_1(Q_{q_2\bar{q}_2}^{q_1\bar{q}_1}(43|21) + Q_{q_2\bar{q}_2}^{q_1\bar{q}_1}(34|21)) - W_2(Q_{q_2\bar{q}_2}^{q_1\bar{q}_1}(34|12) + Q_{q_2\bar{q}_2}^{q_1\bar{q}_1}(43|12)) \\ &\quad - W_3(Q_{q_2\bar{q}_2}^{q_1\bar{q}_1}(21|43) + Q_{q_2\bar{q}_2}^{q_1\bar{q}_1}(12|43)) - W_4(Q_{q_2\bar{q}_2}^{q_1\bar{q}_1}(12|34) + Q_{q_2\bar{q}_2}^{q_1\bar{q}_1}(21|34))]. \end{aligned} \quad (\text{B11})$$

We have the following conservation laws automatically proved by the discretized collision integral from the completeness relation Eq. (A2) and sum rule Eq. (A8):

(1) Charge conservation from completeness relation:

$$\begin{aligned} &\sum_{(i_p, j_\theta, k_\phi)} [\nu_q C_{\bar{q}_1}^{2\leftrightarrow 2}[n](i_p, j_\theta, k_\phi) - \nu_q C_{\bar{q}_1}^{2\leftrightarrow 2}[n](i_p, j_\theta, k_\phi)] \\ &= \sum_{(i_p, j_\theta, k_\phi)} \int d\Omega_{2\leftrightarrow 2} \frac{1}{8} [(W_1 - W_2)(Q_{q_2\bar{q}_2}^{q_1\bar{q}_1}(12|34) + Q_{q_2\bar{q}_2}^{q_1\bar{q}_1}(12|43) - Q_{q_2\bar{q}_2}^{q_1\bar{q}_1}(21|34) - Q_{q_2\bar{q}_2}^{q_1\bar{q}_1}(21|43)) \\ &\quad + (W_3 - W_4)(Q_{q_2\bar{q}_2}^{q_1\bar{q}_1}(34|12) + Q_{q_2\bar{q}_2}^{q_1\bar{q}_1}(34|21) - Q_{q_2\bar{q}_2}^{q_1\bar{q}_1}(43|12) - Q_{q_2\bar{q}_2}^{q_1\bar{q}_1}(43|21))] \\ &= \int d\Omega_{2\leftrightarrow 2} \frac{1}{8} [(1-1)(Q_{q_2\bar{q}_2}^{q_1\bar{q}_1}(12|34) + Q_{q_2\bar{q}_2}^{q_1\bar{q}_1}(12|43) - Q_{q_2\bar{q}_2}^{q_1\bar{q}_1}(21|34) - Q_{q_2\bar{q}_2}^{q_1\bar{q}_1}(21|43)) \\ &\quad + (1-1)(Q_{q_2\bar{q}_2}^{q_1\bar{q}_1}(34|12) + Q_{q_2\bar{q}_2}^{q_1\bar{q}_1}(34|21) - Q_{q_2\bar{q}_2}^{q_1\bar{q}_1}(43|12) - Q_{q_2\bar{q}_2}^{q_1\bar{q}_1}(43|21))] = 0. \end{aligned} \quad (\text{B12})$$

(2) Total number conservation from completeness relation:

$$\begin{aligned} &\sum_{(i_p, j_\theta, k_\phi)} [\nu_q C_{\bar{q}_1}^{2\leftrightarrow 2}[n](i_p, j_\theta, k_\phi) + \nu_q C_{\bar{q}_1}^{2\leftrightarrow 2}[n](i_p, j_\theta, k_\phi) + \nu_q C_{q_2}^{2\leftrightarrow 2}[n](i_p, j_\theta, k_\phi) + \nu_q C_{q_2}^{2\leftrightarrow 2}[n](i_p, j_\theta, k_\phi)] \\ &= \sum_{(i_p, j_\theta, k_\phi)} \int d\Omega_{2\leftrightarrow 2} \frac{1}{8} (W_1 + W_2 - W_3 - W_4)(Q_{q_2\bar{q}_2}^{q_1\bar{q}_1}(12|34) + Q_{q_2\bar{q}_2}^{q_1\bar{q}_1}(12|43) + Q_{q_2\bar{q}_2}^{q_1\bar{q}_1}(21|43) + Q_{q_2\bar{q}_2}^{q_1\bar{q}_1}(21|34) \\ &\quad - Q_{q_2\bar{q}_2}^{q_1\bar{q}_1}(34|12) - Q_{q_2\bar{q}_2}^{q_1\bar{q}_1}(43|12) - Q_{q_2\bar{q}_2}^{q_1\bar{q}_1}(43|21) - Q_{q_2\bar{q}_2}^{q_1\bar{q}_1}(34|21)) \\ &= \int d\Omega_{2\leftrightarrow 2} \frac{1}{8} (1+1-1-1)(Q_{q_2\bar{q}_2}^{q_1\bar{q}_1}(12|34) + Q_{q_2\bar{q}_2}^{q_1\bar{q}_1}(12|43) + Q_{q_2\bar{q}_2}^{q_1\bar{q}_1}(21|43) + Q_{q_2\bar{q}_2}^{q_1\bar{q}_1}(21|34) - Q_{q_2\bar{q}_2}^{q_1\bar{q}_1}(34|12) \\ &\quad - Q_{q_2\bar{q}_2}^{q_1\bar{q}_1}(43|12) - Q_{q_2\bar{q}_2}^{q_1\bar{q}_1}(43|21) - Q_{q_2\bar{q}_2}^{q_1\bar{q}_1}(34|21)) = 0. \end{aligned} \quad (\text{B13})$$

(3) Energy momentum conservation from sum rule, denoting $P_{ij} = (p_i, p_i \cos(\theta_j))$ with $(i, j) \in \mathbb{N}_{p, \theta}^2$, $P_s = (p_s, p_s \cos(\theta_s))$ with $s = 1, 2, 3, 4$, and notice that $W_s = W_{(i_p, j_\theta, k_\phi)}(\vec{P}_s)$:

$$\begin{aligned} &\sum_{(i_p, j_\theta, k_\phi)} P_{ij} [\nu_q C_{\bar{q}_1}^{2\leftrightarrow 2}[n](i_p, j_\theta, k_\phi) + \nu_q C_{\bar{q}_1}^{2\leftrightarrow 2}[n](i_p, j_\theta, k_\phi) + \nu_q C_{q_2}^{2\leftrightarrow 2}[n](i_p, j_\theta, k_\phi) + \nu_q C_{q_2}^{2\leftrightarrow 2}[n](i_p, j_\theta, k_\phi)] \\ &= \sum_{(i_p, j_\theta, k_\phi)} P_{ij} \int d\Omega_{2\leftrightarrow 2} \frac{1}{8} (W_1 + W_2 - W_3 - W_4)(Q_{q_2\bar{q}_2}^{q_1\bar{q}_1}(12|34) + Q_{q_2\bar{q}_2}^{q_1\bar{q}_1}(12|43) + Q_{q_2\bar{q}_2}^{q_1\bar{q}_1}(21|43) + Q_{q_2\bar{q}_2}^{q_1\bar{q}_1}(21|34) \\ &\quad - Q_{q_2\bar{q}_2}^{q_1\bar{q}_1}(34|12) - Q_{q_2\bar{q}_2}^{q_1\bar{q}_1}(43|12) - Q_{q_2\bar{q}_2}^{q_1\bar{q}_1}(43|21) - Q_{q_2\bar{q}_2}^{q_1\bar{q}_1}(34|21)) \\ &= \int d\Omega_{2\leftrightarrow 2} \frac{1}{8} (P_1 + P_2 - P_3 - P_4)(Q_{q_2\bar{q}_2}^{q_1\bar{q}_1}(12|34) + Q_{q_2\bar{q}_2}^{q_1\bar{q}_1}(12|43) + Q_{q_2\bar{q}_2}^{q_1\bar{q}_1}(21|43) + Q_{q_2\bar{q}_2}^{q_1\bar{q}_1}(21|34) - Q_{q_2\bar{q}_2}^{q_1\bar{q}_1}(34|12) \\ &\quad - Q_{q_2\bar{q}_2}^{q_1\bar{q}_1}(43|12) - Q_{q_2\bar{q}_2}^{q_1\bar{q}_1}(43|21) - Q_{q_2\bar{q}_2}^{q_1\bar{q}_1}(34|21)) = 0. \end{aligned} \quad (\text{B14})$$

b. Phase-space integration

Evaluation of the phase-space integrals can be achieved by expressing $p_3 = p_1 + q$ and $p_4 = p_2 - q$ to eliminate the momentum conservation constraint

$$\int d\Omega_{2\leftrightarrow 2} = \int \frac{d^3 p_1}{(2\pi)^3} \int \frac{d^3 p_2}{(2\pi)^3} \int \frac{d^3 q}{(2\pi)^3} \frac{1}{16E_{p_1}E_{p_2}E_{p_3}E_{p_4}} \times (2\pi)\delta(E_{p_1} + E_{p_2} - E_{p_3} - E_{p_4}) \quad (\text{B15})$$

with

$$E_{p_1} = p_1, \quad E_{p_3} = \sqrt{p_1^2 + q^2 + 2p_1q \cos(\theta_{1q})}, \\ E_{p_2} = p_2, \quad E_{p_4} = \sqrt{p_2^2 + q^2 - 2p_2q \cos(\theta_{2q})}. \quad (\text{B16})$$

Similarly, to eliminate the energy conservation constraint we follow the standard trick to parametrize the integral in terms of the energy transfer ω ,

$$(2\pi)\delta(E_{p_1} + E_{p_2} - E_{p_3} - E_{p_4}) \\ = (2\pi) \int d\omega \delta(E_{p_1} + \omega - E_{p_3}) \delta(E_{p_2} - \omega - E_{p_4}). \quad (\text{B17})$$

By expressing the arguments of the δ functions as

$$p_1 + \omega = \sqrt{p_1^2 + q^2 + 2p_1q \cos(\theta_{1q})}, \\ p_2 - \omega = \sqrt{p_2^2 + q^2 - 2p_2q \cos(\theta_{2q})}, \quad (\text{B18})$$

this can be recast into a constraint for the angles

$$\cos(\theta_{1q}) = \frac{w}{q} + \frac{w^2 - q^2}{2p_1q}, \quad \cos(\theta_{2q}) = \frac{w}{q} - \frac{w^2 - q^2}{2p_2q}, \quad (\text{B19})$$

which has a valid solution for

$$|\omega| < q, \quad p_1 > \frac{q - \omega}{2}, \quad p_2 > \frac{q + \omega}{2}. \quad (\text{B20})$$

Evaluating the Jacobian of this transformation as

$$\frac{\partial}{\partial \cos(\theta_{1q})} \left(p_1 + \omega - \sqrt{p_1^2 + q^2 + 2p_1q \cos(\theta_{1q})} \right) = \frac{-p_1q}{E_{p_3}}, \\ \frac{\partial}{\partial \cos(\theta_{2q})} \left(p_2 - \omega - \sqrt{p_2^2 + q^2 - 2p_2q \cos(\theta_{2q})} \right) = \frac{+p_2q}{E_{p_4}}, \quad (\text{B21})$$

the phase-space integral can then be recast into the form

$$\int d\Omega_{2\leftrightarrow 2} = (2\pi) \int \frac{d^3 p_1}{(2\pi)^3} \int \frac{d^3 p_2}{(2\pi)^3} \int \frac{d^3 q}{(2\pi)^3} \\ \times \int d\omega \frac{1}{16p_1^2 p_2^2 q^2} \theta(q - |\omega|) \theta\left(p_1 - \frac{q - \omega}{2}\right) \\ \times \theta\left(p_2 - \frac{q + \omega}{2}\right) \delta\left(\frac{w}{q} + \frac{w^2 - q^2}{2p_1q} - \cos(\theta_{1q})\right) \\ \times \delta\left(\frac{w}{q} - \frac{w^2 - q^2}{2p_2q} - \cos(\theta_{2q})\right). \quad (\text{B22})$$

Clearly the most straightforward way to implement the constraints is to perform the q and ω integrations prior to the p_1 and p_2 integrations, such that the vectors p_1 and p_2 can be parametrized in terms of spherical coordinates in a right-handed orthonormal system spanned by the unit vectors

$$\vec{e}_1 = \vec{e}_q = \frac{\vec{q}}{|\vec{q}|}, \quad \vec{e}_2 = \frac{\vec{e}_n - \cos(\theta_q)\vec{e}_q}{|\vec{e}_n - \cos(\theta_q)\vec{e}_q|}, \\ \vec{e}_3 = \frac{\vec{e}_q \times (\vec{e}_n - \cos(\theta_q)\vec{e}_q)}{|\vec{e}_q \times (\vec{e}_n - \cos(\theta_q)\vec{e}_q)|}, \quad (\text{B23})$$

where \vec{e}_n denotes the preferred axis of the coordinate system, such that

$$\vec{p}_1 = p_1 \left[\cos(\theta_{1q})\vec{e}_q + \sin(\theta_{1q}) \cos(\phi_1) \frac{\vec{e}_n - \cos(\theta_q)\vec{e}_q}{|\vec{e}_n - \cos(\theta_q)\vec{e}_q|} \right. \\ \left. + \sin(\theta_{1q}) \sin(\phi_1) \frac{\vec{e}_q \times (\vec{e}_n - \cos(\theta_q)\vec{e}_q)}{|\vec{e}_q \times (\vec{e}_n - \cos(\theta_q)\vec{e}_q)|} \right], \\ \vec{p}_2 = p_2 \left[\cos(\theta_{2q})\vec{e}_q + \sin(\theta_{2q}) \cos(\phi_2) \frac{\vec{e}_n - \cos(\theta_q)\vec{e}_q}{|\vec{e}_n - \cos(\theta_q)\vec{e}_q|} \right. \\ \left. + \sin(\theta_{2q}) \sin(\phi_2) \frac{\vec{e}_q \times (\vec{e}_n - \cos(\theta_q)\vec{e}_q)}{|\vec{e}_q \times (\vec{e}_n - \cos(\theta_q)\vec{e}_q)|} \right], \quad (\text{B24})$$

which allows for a straightforward evaluation of the constraints on $\cos(\theta_{1q})$ and $\cos(\theta_{2q})$ yielding

$$\int d\Omega_{2\leftrightarrow 2} = \frac{1}{16(2\pi)^8} \int_0^\infty dq \int_{-1}^1 d\cos(\theta_q) \int_0^{2\pi} d\phi_q \int_{-q}^q d\omega \\ \times \int_{\max(\frac{q-\omega}{2}, 0)}^\infty dp_1 \int_{\max(\frac{q+\omega}{2}, 0)}^\infty dp_2 \int_0^{2\pi} d\phi_1 \int_0^{2\pi} d\phi_2. \quad (\text{B25})$$

Specifically in terms of these coordinates the angles of p_1 and p_2 with respect to the anisotropy direction are given by

$$\cos(\theta_1) = \cos(\theta_{1q}) \cos(\theta_q) + \sin(\theta_{1q}) \sin(\theta_q) \cos(\phi_1), \\ \cos(\theta_2) = \cos(\theta_{2q}) \cos(\theta_q) + \sin(\theta_{2q}) \sin(\theta_q) \cos(\phi_2). \quad (\text{B26})$$

Note that if we wish to impose constraints on the magnitudes of $p_1^{\min} < p_1 < p_1^{\max}$ and $p_2^{\min} < p_2 < p_2^{\max}$, then the corresponding phase-space constraints take the form

$$\begin{aligned} \max\left(\frac{q-\omega}{2}, p_1^{\min}\right) &< p_1 < p_1^{\max}, \\ \max\left(\frac{q+\omega}{2}, p_2^{\min}\right) &< p_2 < p_2^{\max}. \end{aligned} \quad (\text{B27})$$

2. Inelastic collision integrals

a. Collinear radiation

The inelastic collision integral for particle ‘‘a’’ with momentum \vec{p}_1 in splitting process $a \rightarrow b, c$ ($p_1 \leftrightarrow p_2, p_3$) and joining process $a, b \rightarrow c$ ($p_1, p_2 \leftrightarrow p_3$) reads

$$\begin{aligned} C_a^{1\leftrightarrow 2}[f](\vec{p}_1) &= \frac{1}{2\nu_a} \frac{1}{2E_{p_1}} \sum_{bc} \int d\Pi_{1\leftrightarrow 2}^{a\leftrightarrow bc} |\mathcal{M}_{bc}^a(\vec{p}_1|\vec{p}_2, \vec{p}_3)|^2 F_{bc}^a(\vec{p}_1|\vec{p}_2, \vec{p}_3) \\ &\quad + \frac{1}{\nu_a} \frac{1}{2E_{p_1}} \int d\Pi_{1\leftrightarrow 2}^{ab\leftrightarrow c} |\mathcal{M}_c^{ab}(\vec{p}_1, \vec{p}_2|\vec{p}_3)|^2 F_c^{ab}(\vec{p}_1, \vec{p}_2|\vec{p}_3) \\ &= \frac{1}{2\nu_a} \frac{1}{2E_{p_1}} \sum_{bc} \int d\Pi_{1\leftrightarrow 2}^{a\leftrightarrow bc} |\mathcal{M}_{bc}^a(\vec{p}_1|\vec{p}_2, \vec{p}_3)|^2 F_{bc}^a(\vec{p}_1|\vec{p}_2, \vec{p}_3) \\ &\quad - \frac{1}{\nu_a} \frac{1}{2E_{p_1}} \int d\Pi_{1\leftrightarrow 2}^{ab\leftrightarrow c} |\mathcal{M}_{ab}^c(\vec{p}_3|\vec{p}_1, \vec{p}_2)|^2 F_{ab}^c(\vec{p}_3|\vec{p}_1, \vec{p}_2) \end{aligned} \quad (\text{B28})$$

with measure

$$\begin{aligned} \int d\Pi_{1\leftrightarrow 2}^{a\leftrightarrow bc} &= \int \frac{d^3 p_2}{(2\pi)^3} \frac{1}{2E_{p_2}} \int \frac{d^3 p_3}{(2\pi)^3} \frac{1}{2E_{p_3}} \times (2\pi)^4 \delta^{(4)}(p_1 - p_2 - p_3). \\ \int d\Pi_{1\leftrightarrow 2}^{ab\leftrightarrow c} &= \int \frac{d^3 p_2}{(2\pi)^3} \frac{1}{2E_{p_2}} \int \frac{d^3 p_3}{(2\pi)^3} \frac{1}{2E_{p_3}} \times (2\pi)^4 \delta^{(4)}(p_1 + p_2 - p_3). \end{aligned} \quad (\text{B29})$$

$|\mathcal{M}_{bc}^a(\vec{p}_1|\vec{p}_2, \vec{p}_3)|^2$ and $|\mathcal{M}_c^{ab}(\vec{p}_1, \vec{p}_2|\vec{p}_3)|^2$ are the matrix element squares for process ‘‘ $a \leftrightarrow b, c$ ’’ and ‘‘ $a, b \leftrightarrow c$.’’ $F_{cd}^a(\vec{p}_1|\vec{p}_3, \vec{p}_4)$ and $F_c^{ab}(\vec{p}_1, \vec{p}_2|\vec{p}_3)$ are the statistical factors. Similarly, we define Q -factors

$$\begin{aligned} Q_{bc}^a(1|23) &= Q_{bc}^a(\vec{p}_1|\vec{p}_2, \vec{p}_3) = |\mathcal{M}_{bc}^a(\vec{p}_1|\vec{p}_2, \vec{p}_3)|^2 F_{bc}^a(\vec{p}_1|\vec{p}_2, \vec{p}_3), \\ Q_c^{ab}(12|3) &= Q_c^{ab}(\vec{p}_1, \vec{p}_2|\vec{p}_3) = |\mathcal{M}_c^{ab}(\vec{p}_1, \vec{p}_2|\vec{p}_3)|^2 F_c^{ab}(\vec{p}_1, \vec{p}_2|\vec{p}_3), \end{aligned} \quad (\text{B30})$$

which have the following symmetries:

$$Q_{bc}^a(\vec{p}_1|\vec{p}_2, \vec{p}_3) = Q_{cb}^a(\vec{p}_1|\vec{p}_3, \vec{p}_2) = -Q_a^{bc}(\vec{p}_2, \vec{p}_3|\vec{p}_1). \quad (\text{B31})$$

As was suggested by AMY [52], in a nearly collinear inelastic scattering, after integration all soft kick particles from the medium, and assuming massless kinematics, the collision integral in Eq. (B28) can be recast into 1D collinear process (we denote $p = |\vec{p}| \approx p_{\parallel}$)

$$\begin{aligned} C_a^{1\leftrightarrow 2}[f](p_1) &= \frac{(2\pi)^3}{2\nu_a p_1^2} \sum_{bc} \int_0^\infty dp_2 dp_3 \delta(p_1 - p_2 - p_3) \gamma_{bc}^a(p_1|p_2, p_3) F_{bc}^a(p_1|p_2, p_3) \\ &\quad - \frac{(2\pi)^3}{\nu_a p_1^2} \int_0^\infty dp_2 dp_3 \delta(p_1 + p_2 - p_3) \gamma_{ab}^c(p_3|p_1, p_2) F_{ab}^c(p_3|p_1, p_2), \end{aligned} \quad (\text{B32})$$

where in the statistical distribution, we only put the momentum components of $p_2 = \vec{p}_2 \cdot \vec{p}_1 / |\vec{p}_1|$ and $p_3 = \vec{p}_3 \cdot \vec{p}_1 / |\vec{p}_1|$ which is in parallel to the p_1 , while $p_1 = |\vec{p}_1|$ is its full momentum.

We parametrize the phase-space for inelastic rates by setting $p_1 = p$, $p_2 = zp$, $p_3 = \bar{z}p$ in the first term

$$\int_0^\infty dp_2 dp_3 \delta(p_1 - p_2 - p_3) \gamma_{bc}^a(p_1|p_2, p_3) = p \int_0^1 dz d\bar{z} \delta(1 - z - \bar{z}) \gamma_{bc}^a(p|zp, \bar{z}p), \quad (\text{B33})$$

and similarly by setting $p_1 = p$, $p_3 = p_1/z$, $p_2 = \bar{z}p_3$ in the second term

$$\int_0^\infty dp_2 dp_3 \delta(p_1 + p_2 - p_3) \gamma_{ab}^c(p_3 | p_1, p_2) = p \int_0^1 dz d\bar{z} \frac{1}{z^2} \delta(1 - z - \bar{z}) \gamma_{ab}^c\left(\frac{p}{z} \middle| p, \frac{\bar{z}}{z} p\right), \quad (\text{B34})$$

such that upon defining the effective rate

$$\frac{d\Gamma_{bc}^a}{dz}(p, z) = \frac{(2\pi)^3}{\nu_a p} \gamma_{bc}^a(p | zp, \bar{z}p) \quad (\text{B35})$$

we arrive at

$$\begin{aligned} C_a^{1\leftrightarrow 2}[f](p) &= \frac{(2\pi)^3}{2\nu_a p} \sum_{bc} \int_0^1 dz d\bar{z} \delta(1 - z - \bar{z}) \gamma_{bc}^a(p | zp, \bar{z}p) F_{bc}^a(p | zp, \bar{z}p) - \frac{(2\pi)^3}{\nu_a p} \int_0^1 dz d\bar{z} \frac{1}{z^2} \delta(1 - z - \bar{z}) \\ &\quad \times \gamma_{ab}^c\left(\frac{p}{z} \middle| p, \frac{\bar{z}}{z} p\right) F_{ab}^c\left(\frac{p}{z} \middle| p, \frac{\bar{z}}{z} p\right) \\ &= \frac{1}{2\nu_a} \int_0^1 dz \sum_{bc} \left[\frac{d\Gamma_{bc}^a}{dz}(p_1, z) \nu_a F_{bc}^a(p | zp, \bar{z}p) - \frac{2}{z^3} \frac{d\Gamma_{ab}^c}{dz}\left(\frac{p}{z}, z\right) \nu_c F_{ab}^c\left(\frac{p}{z} \middle| p, \frac{\bar{z}}{z} p\right) \right], \end{aligned} \quad (\text{B36})$$

where $\bar{z} = 1 - z$. We may further symmetrize this expression by splitting the second term into two terms integrating over z and $1 - z$ such that

$$\begin{aligned} C_a^{1\leftrightarrow 2}[f](p) &= \frac{1}{2\nu_a} \int_0^1 dz \left[\sum_{bc} \frac{d\Gamma_{bc}^a}{dz}(p, z) \nu_a F_{bc}^a(p | zp, \bar{z}p) \right. \\ &\quad \left. - \frac{1}{z^3} \frac{d\Gamma_{ab}^c}{dz}\left(\frac{p}{z}, z\right) \nu_c F_{ab}^c\left(\frac{p}{z} \middle| p, \frac{\bar{z}}{z} p\right) - \frac{1}{\bar{z}^3} \frac{d\Gamma_{ab}^c}{dz}\left(\frac{p}{\bar{z}}, \bar{z}\right) \nu_c F_{ab}^c\left(\frac{p}{\bar{z}} \middle| p, \frac{z}{\bar{z}} p\right) \right]. \end{aligned} \quad (\text{B37})$$

b. Discretization of collinear form

The discretized form of collinear collision integral in Eq. (B37) follows the transformation in Eq. (A1):

$$\begin{aligned} C_a^{1\leftrightarrow 2}[n](i_p, j_\theta, k_\phi) &= \int \frac{d^3 p}{(2\pi)^3} W_{(i_p, j_\theta, k_\phi)}(\vec{p}) C_a^{1\leftrightarrow 2}[f](p) \\ &= \frac{1}{4\pi^2} \int_0^\infty p^2 dp \int_{-1}^{+1} d\cos(\theta) W_{(i_p, j_\theta, k_\phi)}(\vec{p}) C_a^{1\leftrightarrow 2}[f](p) \\ &= \frac{1}{8\pi^2 \nu_a} \int_0^\infty p^2 dp \int_{-1}^{+1} d\cos(\theta) \int_0^1 dz W_{(i_p, j_\theta, k_\phi)}(\vec{p}) \times \left[\sum_{bc} \frac{d\Gamma_{bc}^a}{dz}(p, z) \nu_a F_{bc}^a(p | zp, \bar{z}p) \right. \\ &\quad \left. - \frac{1}{z^3} \frac{d\Gamma_{ab}^c}{dz}\left(\frac{p}{z}, z\right) \nu_c F_{ab}^c\left(\frac{p}{z} \middle| p, \frac{\bar{z}}{z} p\right) - \frac{1}{\bar{z}^3} \frac{d\Gamma_{ab}^c}{dz}\left(\frac{p}{\bar{z}}, \bar{z}\right) \nu_c F_{ab}^c\left(\frac{p}{\bar{z}} \middle| p, \frac{z}{\bar{z}} p\right) \right] \\ &= \frac{1}{8\pi^2 \nu_a} \int_0^\infty p^2 dp \int_{-1}^{+1} d\cos(\theta) \int_0^1 dz \left[\sum_{bc} \frac{d\Gamma_{bc}^a}{dz}(p, z) \nu_a F_{bc}^a(p | zp, \bar{z}p) W_{(i_p, j_\theta, k_\phi)}(p) \right. \\ &\quad \left. - \frac{d\Gamma_{ab}^c}{dz}(p, z) \nu_c F_{ab}^c(p | zp, \bar{z}p) W_{(i_p, j_\theta, k_\phi)}(zp) - \frac{d\Gamma_{ab}^c}{dz}(p, \bar{z}) \nu_c F_{ab}^c(p | \bar{z}p, zp) W_{(i_p, j_\theta, k_\phi)}(\bar{z}p) \right], \end{aligned} \quad (\text{B38})$$

where we used a redefinition of the integrals $\int \frac{d^3 p}{(2\pi)^3} \frac{1}{z^3} = \int \frac{d^3 p'}{(2\pi)^3}$ (and similarly for \bar{z}) to bring all terms into the same form.

Note that

$$\begin{aligned}\frac{d\Gamma_{ab}^c}{dz}(p, \bar{z}) &= \frac{d\Gamma_{ba}^c}{dz}(p, z), \\ F_{ab}^c(p|\bar{z}p, zp) &= F_{ba}^c(p|zp, \bar{z}p).\end{aligned}\quad (\text{B39})$$

which has the following symmetry:

$$\Delta_{ab}^c(p, z) = \Delta_{ba}^c(p, \bar{z}). \quad (\text{B41})$$

Define a Δ -factor for inelastic collision

$$\Delta_{ab}^c(p, z) = \frac{d\Gamma_{ab}^c}{dz}(p, z)\nu_c F_{ab}^c(p|zp, \bar{z}p), \quad (\text{B40})$$

With a refinement of the measure and weight in the integral $d\Pi = \frac{1}{8\pi^2} \int_0^\infty p^2 dp \int_{-1}^{+1} d\cos(\theta) \int_0^1 dz$ and $W(p) = W_{(i_p, j_\theta, k_\phi)}(p)$, we can rewrite the form into

$$C_a^{1\leftrightarrow 2}[n](i_p, j_\theta, k_\phi) = \frac{1}{\nu_a} \int d\Pi \left[\sum_{bc} \Delta_{bc}^a(p, z) W(p) - \Delta_{ab}^c(p, z) W(zp) - \Delta_{ba}^c(p, z) W(\bar{z}p) \right]. \quad (\text{B42})$$

For $b \neq c$, we have the following useful equivalent form of Eq. (B42) for convenience:

$$\begin{aligned}C_a^{1\leftrightarrow 2}[n](i_p, j_\theta, k_\phi) &= \frac{1}{\nu_a} \int d\Pi [(\Delta_{bc}^a(p, z) + \Delta_{cb}^a(p, \bar{z})) W(p) - \Delta_{ab}^c(p, z) W(zp) - \Delta_{ba}^c(p, z) W(\bar{z}p)] \\ &= \frac{1}{\nu_a} \int d\Pi [(\Delta_{bc}^a(p, z) + \Delta_{bc}^a(p, \bar{z})) W(p) - \Delta_{ab}^c(p, z) W(zp) - \Delta_{ab}^c(p, \bar{z}) W(\bar{z}p)].\end{aligned}\quad (\text{B43})$$

For $b = c$, we have

$$\begin{aligned}C_a^{1\leftrightarrow 2}[n](i_p, j_\theta, k_\phi) &= \frac{1}{\nu_a} \int d\Pi [\Delta_{cc}^a(p, z) W(p) - \Delta_{ac}^c(p, z) W(zp) - \Delta_{ca}^c(p, z) W(\bar{z}p)] \\ &= \frac{1}{\nu_a} \int d\Pi [\Delta_{cc}^a(p, z) W(p) - \Delta_{ac}^c(p, z) W(zp) - \Delta_{ac}^c(p, \bar{z}) W(\bar{z}p)],\end{aligned}\quad (\text{B44})$$

where we use the fact that for any function $f(p, z)$, we have

$$\int_0^1 dz f(p, z) = \int_0^1 dz f(p, 1-z). \quad (\text{B45})$$

Now we list the discretized collision integrals for all inelastic processes and prove the exact conservation taking the most complicated process $g \leftrightarrow q\bar{q}$ for example.

a. Process $g \leftrightarrow q\bar{q}$ The available collision integrals are listed below:

(1) For gluon g ($q\bar{q} = u\bar{u}, d\bar{d}, s\bar{s}$)

$$C_g^{1\leftrightarrow 2}[n](i_p, j_\theta, k_\phi) = \frac{1}{\nu_g} \int d\Pi [(\Delta_{q\bar{q}}^g(p, z) + \Delta_{\bar{q}q}^g(p, z)) W(p)]. \quad (\text{B46})$$

(2) For quark q ($q = u, d, s$)

$$C_q^{1\leftrightarrow 2}[n](i_p, j_\theta, k_\phi) = \frac{1}{\nu_q} \int d\Pi [-\Delta_{q\bar{q}}^g(p, z) W(zp) - \Delta_{\bar{q}q}^g(p, z) W(\bar{z}p)]. \quad (\text{B47})$$

(3) For antiquark \bar{q} ($\bar{q} = \bar{u}, \bar{d}, \bar{s}$)

$$C_{\bar{q}}^{1\leftrightarrow 2}[n](i_p, j_\theta, k_\phi) = \frac{1}{\nu_{\bar{q}}} \int d\Pi [-\Delta_{\bar{q}q}^g(p, z) W(zp) - \Delta_{q\bar{q}}^g(p, z) W(\bar{z}p)]. \quad (\text{B48})$$

Again, we denote $P_{ij} = (p_i, p_i \cos(\theta_j)) = p_i \Theta_j$ with $(i, j) \in \mathbb{N}_{p, \theta}^2$. Since collinear collision has the same scattering angle for in and out particles, the particles a, b, c have energy and longitudinal momentum $P = (p, p \cos(\theta))$,

$zP = (zp, zp \cos(\theta))$, $\bar{z}P = (\bar{z}p, \bar{z}p \cos(\theta))$. The collision integral has the following conservation laws automatically proved by the discretized collision integral from the completeness relation Eq. (A2) and sum rule Eq. (A8):

(1) Charge conservation for $g \rightarrow q\bar{q}$ ($q\bar{q} = u\bar{u}, d\bar{d}, s\bar{s}$)

$$\begin{aligned} \sum_{(i_p, j_\theta, k_\phi)} [\nu_q C_q^{1\leftrightarrow 2}[n] - \nu_{\bar{q}} C_{\bar{q}}^{1\leftrightarrow 2}[n]] &= \sum_{(i_p, j_\theta, k_\phi)} \int d\Pi [(\Delta_{q\bar{q}}^g(p, z) - \Delta_{\bar{q}q}^g(p, z))(W(zp) - W(\bar{z}p))] \\ &= \int d\Pi [(\Delta_{q\bar{q}}^g(p, z) - \Delta_{\bar{q}q}^g(p, z))(1 - 1)] = 0. \end{aligned} \quad (\text{B49})$$

(2) Energy momentum conservation for $g \rightarrow q\bar{q}$ ($q\bar{q} = u\bar{u}, d\bar{d}, s\bar{s}$)

$$\begin{aligned} \sum_{(i_p, j_\theta, k_\phi)} P_{ij} [\nu_g C_g^{1\leftrightarrow 2}[n] + \nu_q C_q^{1\leftrightarrow 2}[n] + \nu_{\bar{q}} C_{\bar{q}}^{1\leftrightarrow 2}[n]] &\sum_{(i_p, j_\theta, k_\phi)} P_{ij} \int d\Pi [(\Delta_{q\bar{q}}^g(p, z) + \Delta_{\bar{q}q}^g(p, z))(W(p) - W(zp) - W(\bar{z}p))] \\ &= \int d\Pi [(\Delta_{q\bar{q}}^g(p, z) + \Delta_{\bar{q}q}^g(p, z))(P - zp - \bar{z}P)] = 0. \end{aligned} \quad (\text{B50})$$

b. Process $g \leftrightarrow gg$ The gluon collision integral is

$$C_g^{1\leftrightarrow 2}[n](i_p, j_\theta, k_\phi) = \frac{1}{\nu_g} \int d\Pi [\Delta_{gg}^g(p, z)(W(p) - W(zp) - W(\bar{z}p))]. \quad (\text{B51})$$

c. Process $q \leftrightarrow gq$ The available collision integrals for partons are listed below

(1) For gluon g ($q = u, d, s, \bar{u}, \bar{d}, \bar{s}$)

$$C_g^{1\leftrightarrow 2}[n](i_p, j_\theta, k_\phi) = \frac{1}{\nu_g} \int d\Pi [-\Delta_{gq}^g(p, z)W(zp) - \Delta_{qg}^g(p, z)W(\bar{z}p)]. \quad (\text{B52})$$

(2) For quark/antiquark q ($q = u, d, s, \bar{u}, \bar{d}, \bar{s}$)

$$C_q^{1\leftrightarrow 2}[n](i_p, j_\theta, k_\phi) = \frac{1}{\nu_q} \int d\Pi [(\Delta_{qg}^g(p, z) + \Delta_{gq}^g(p, z))W(p) - \Delta_{qg}^g(p, z)W(zp) - \Delta_{gq}^g(p, z)W(\bar{z}p)]. \quad (\text{B53})$$

3. Longitudinal expansion integrals

In a longitudinally expanding system, there is an additional contribution to the collision integral which can be expressed in the form of a collision integral [see Eq. (46)]

$$C_a^{\text{z-exp}}[f](\vec{p}, t) = -\frac{p_{\parallel}}{t} \frac{\partial f_a(\vec{p}, t)}{\partial p_{\parallel}} = -\frac{p \cos(\theta)}{t} \left[\cos(\theta) \frac{\partial f_a(\vec{p}, t)}{\partial p} + \frac{\sin^2(\theta)}{p} \frac{\partial f_a(\vec{p}, t)}{\partial \cos(\theta)} \right]. \quad (\text{B54})$$

Thus the discretized form of the collision integral for the azimuthal-isotropic medium can be evaluated as

$$\begin{aligned} C_a^{\text{z-exp}}[n](i_p, j_\theta) &= -\frac{1}{(2\pi)^2} \int_0^\infty dp p^2 \int_{-1}^1 d\cos(\theta) w_i^{(p)}(p) w_j^{(\theta)}(\theta) \\ &\quad \times \frac{p \cos(\theta)}{t} \left[\cos(\theta) \frac{\partial f_a(\vec{p}, t)}{\partial p} + \frac{\sin^2(\theta)}{p} \frac{\partial f_a(\vec{p}, t)}{\partial \cos(\theta)} \right]. \end{aligned} \quad (\text{B55})$$

Note from Eq. (A16), we can reexpress the distribution $f(\vec{p}, t)$ in the continuous domain in terms of a summation of its neighboring discretized forms

$$f(\vec{p}, t) = \frac{1}{p^l} \sum_{\alpha, \beta} w_{\alpha}^{(p)}(p) w_{\beta}^{(\theta)}(\theta) \frac{(2\pi)^2}{A_{(\alpha)}^{(2-l)} A_{(\beta)}} n(\alpha, \beta), ((\alpha, \beta) \in \mathbb{N}_{p, \theta}^2). \quad (\text{B56})$$

We approximate the $f(\vec{p} \in U_{(i_p, j_\theta)})$ with $f(\vec{p} \in U_p)$ where $U_{(i_p, j_\theta)} = (p_{i-1}, p_{i+1}) \times (\theta_{j-1}, \theta_{j+1})$ and $U_p = (p_i, p_{i+1}) \times (\theta_j, \theta_{j+1})$. Then we can construct the collision term in discretized grids with a derivative of weight functions

$$\begin{aligned} C^{\text{z-exp}}[n](i_p, j_\theta) &= M^{\text{z-exp}}(i_p, j_\theta) n(\alpha, \beta) \\ &= - \sum_{(\alpha, \beta) \in \mathbb{N}_{p, \theta}^2} \int \frac{d^3 p}{(2\pi)^3} \left(\frac{(2\pi)^2 p \cos(\theta)}{t A_{(\alpha)}^{(2-l)} A_{(\beta)}} \right) w_i^{(p)}(p) w_j^{(\theta)}(\theta) \left[\cos(\theta) \frac{\partial}{\partial p} \left(\frac{w_{\alpha}^{(p)}}{p^l} \right) w_{\beta}^{(\theta)}(\theta) + \frac{\sin^2(\theta)}{p} \left(\frac{w_{\alpha}^{(p)}}{p^l} \right) \frac{\partial w_{\beta}^{(\theta)}(\theta)}{\partial \cos(\theta)} \right] n(\alpha, \beta) \\ &\text{with derivatives} \\ \frac{\partial}{\partial p} \left(\frac{w_{\alpha}^{(p)}}{p^l} \right) &= \frac{1}{p^{l+1}} \left[\frac{(l-1)p - lp_{\alpha+1}}{p_{\alpha+1} - p_{\alpha}} \chi_{[p_{\alpha}, p_{\alpha+1}]}(p) + \frac{lp_{\alpha-1} - (l-1)p}{p_{\alpha} - p_{\alpha-1}} \chi_{[p_{\alpha-1}, p_{\alpha}]}(p) \right] \\ \frac{\partial w_{\beta}^{(\theta)}(\theta)}{\partial \cos(\theta)} &= \left[\frac{-1}{\cos(\theta_{\beta+1}) - \cos(\theta_{\beta})} \chi_{[\theta_{\beta}, \theta_{\beta+1}]}(\theta) + \frac{1}{\cos(\theta_{\beta}) - \cos(\theta_{\beta-1})} \chi_{[\theta_{\beta-1}, \theta_{\beta}]}(\theta) \right]. \end{aligned} \quad (\text{B57})$$

The integrated out expression is analytic but lengthy, and we do not list it here.

APPENDIX C: EVOLUTION ALGORITHM

1. Grid setup

We discussed the discretized algorithm in Appendixes A and B without specifying the choice of grids distribution in the phase-space since the algorithm is generally independent of the choice. However, since the particle distributions are generally accumulated at low momentum and eliminated at high momentum near equilibrium, an exponential distribution of grid points along momentum p is preferred. Similarly, the system is close to isotropic near equilibrium; thus a linear distribution of grid points along angle θ is preferred. With those considerations, we set up the grids as

$$p_i = p_{\min} \left(\frac{p_{\max}}{p_{\min}} \right)^{\frac{i}{N_p - 1}}, \quad i = 0, \dots, N_p - 1; \quad (\text{C1})$$

$$\cos \theta_j = \frac{j}{N_{\theta} - 1} (\cos \theta_{\max} - \cos \theta_{\min}), \quad j = 0, \dots, N_{\theta} - 1,$$

with p_{\min} chosen as a nonzero small value to avoid singularity at the initial point and $\theta_{\min} = 0$, $\theta_{\max} = \pi$. The choice of p_{\max} and the maximal number of intervals depend on the specific systems we want to inspect. For underoccupied systems with high momentum jets, their values should increase.

We take $N_p = 64$, $N_{\theta} = 64$ for isotropic systems and $N_p = 256$, $N_{\theta} = 64$ for anisotropic systems where higher accuracy is needed.

2. Inelastic rate interpolation

The effective inelastic rates $\frac{d\Gamma_{bc}^a}{dz}(p, z)$ are also depending on screening masses m_D , m_{Qf} which are evaluated every time step during the evolution; hence we need to evaluate the effective inelastic rates dynamically. The calculation of the effective inelastic rate is numerically intensive; thus we do not calculate the rate for every time step. Instead, we first calculate the rates as functions of $\omega_{\text{BH}} = \frac{m_D^2}{g^2 T^*}$, $x_{\text{DQf}} = \frac{m_D^2}{m_{Qf}^2}$ for each inelastic process and each quark flavor. Then we set up 2D local rate grids on scales ω_{BH} , x_{DQf} with the grid boundary varied by $\pm 20\%$ of their central values. Since the scales m_D^2 , m_{Qf}^2 , T^* are changing modestly (see Sec. C4), the rates in the upcoming steps can be interpolated from the grids as long as the upcoming scales ω_{BH} , x_{DQf} are within the grid squares. Once either ω_{BH} , x_{DQf} evolves outside of the grid squares, we recalculate the inelastic rates based on the current scales.

3. Monte Carlo sampling

We perform Monte Carlo integration of collision integrals for both elastic and inelastic processes.

For the elastic samplings, we first sample q , then $-q \leq \omega \leq q$, and finally $\frac{q-\omega}{2} \leq p_1$, $\frac{q+\omega}{2} \leq p_2$ according to the discussions in Sec. B1b. The samplings of angles $\cos(\theta_q)$, ϕ_q together with ϕ_1 , ϕ_2 help us determine the values for p_3 , p_4 . With each of set of samplings for momenta p_1 , p_2 , p_3 , p_4 , we calculate the discretized collision integral according to Eq. (B7) which simultaneously updates the gain and loss terms of all the

processes, which by virtue of the sum rules ensures exact energy and particle number conservation as was discussed in Sec. B 1 a. Similarly, the evaluation of inelastic collision integrals are performed by sampling p , z and the angle with respect to the longitudinal direction $\cos(\theta)$ according to Eq. (B42) which also simultaneously updates the gain and loss terms.

The summation of all relevant processes and all samplings for collision integrals provides the total collision integral in the Boltzmann equation for the specific particle.

The sampling numbers are chosen to be $N_{\text{sample,elastic}} = 512$ for each specific elastic process and $N_{\text{sample,inelastic}} = 256$ for each specific inelastic process.

4. Adaptive time step

Evolving the particle distributions in the discretized domain, we need an adaptive time step size Δt to perform a stable increment for each distinct step

$$\begin{aligned} \Delta n_a(i_p, j_\theta, k_\phi, t) = & -[C_a^{2\leftrightarrow 2}[n](i_p, j_\theta, k_\phi, t) \\ & + C_a^{1\leftrightarrow 2}[n](i_p, j_\theta, k_\phi, t) \\ & + C_a^{z\text{-exp}}[n](i_p, j_\theta, k_\phi, t)]\Delta t. \end{aligned} \quad (\text{C2})$$

In order to do that, we need to make sure essential physics scales are not changing rapidly in each step. Common scales into considerations are total number density n , total energy density e and total longitudinal pressure p_L , Debye screening mass square m_D^2 , quark screening mass square m_{Qf}^2 , and effective temperature T^* . Some other scales may also be considered. However, more scales will not only increase the stability, but also slow down the evolution with a shorter resulting time step Δt . According to their expressions listed in Sec. II A, their relative changing rate can be approximated by

$$\begin{aligned} \frac{\partial_t n}{n} &= \frac{\int d^3 p [\nu_g C_A \partial_t f_g + \nu_q C_F \sum_f (\partial_t f_q + \partial_t f_{\bar{q}})]}{\int d^3 p [\nu_g C_A f_g + \nu_q C_F \sum_f (f_q + f_{\bar{q}})]}, \\ \frac{\partial_t e}{e} &= \frac{\int p d^3 p [\nu_g C_A \partial_t f_g + \nu_q C_F \sum_f (\partial_t f_q + \partial_t f_{\bar{q}})]}{\int p d^3 p [\nu_g C_A f_g + \nu_q C_F \sum_f (f_q + f_{\bar{q}})]}, \\ \frac{\partial_t p_L}{p_L} &= \frac{\int p \cos^2(\theta) d^3 p [\nu_g C_A \partial_t f_g + \nu_q C_F \sum_f (\partial_t f_q + \partial_t f_{\bar{q}})]}{\int p \cos^2(\theta) d^3 p [\nu_g C_A f_g + \nu_q C_F \sum_f (f_q + f_{\bar{q}})]}, \\ \frac{\partial_t m_D^2}{m_D^2} &= \frac{\int \frac{d^3 p}{2p} [\nu_g C_A \partial_t f_g + \nu_q C_F \sum_f (\partial_t f_q + \partial_t f_{\bar{q}})]}{\int \frac{d^3 p}{2p} [\nu_g C_A f_g + \nu_q C_F \sum_f (f_q + f_{\bar{q}})]}, \\ \frac{\partial_t m_{Qf}^2}{m_{Qf}^2} &= \frac{\int \frac{d^3 p}{2p} [2\partial_t f_G + (\partial_t f_{Qf} + \partial_t f_{\bar{Qf}})]}{\int \frac{d^3 p}{2p} [2f_G + (f_{Qf} + f_{\bar{Qf}})]}, \\ \frac{\partial_t m_D^2 T^*}{m_D^2 T^*} &= \frac{\int d^3 p [\nu_g C_A (\partial_t f_g + 2f_g d f_g) + \nu_q C_F \sum_f (\partial_t f_q - 2f_q \partial_t f_q + \partial_t f_{\bar{q}} - 2f_{\bar{q}} \partial_t f_{\bar{q}})]}{\int d^3 p [\nu_g C_A f_g (1 + f_g) + \nu_q C_F \sum_f ((f_q (1 - f_q) + f_{\bar{q}} (1 - f_{\bar{q}}))]} \end{aligned} \quad (\text{C3})$$

In those preceding formulas the time derivative of distribution ∂_t can be evaluated according to Eq. (A16),

$$\begin{aligned} \partial_t f(\vec{p}, t) &= \frac{1}{p^l} \sum_{\alpha, \beta} w_\alpha^{(p)}(p) w_\beta^{(\theta)}(\theta) \frac{(2\pi)^2}{A_{(\alpha)}^{(2-l)} A_{(\beta)}} \frac{\Delta n(\alpha, \beta)}{\Delta t} \\ &= -\frac{1}{p^l} \sum_{\alpha, \beta} w_\alpha^{(p)}(p) w_\beta^{(\theta)}(\theta) \frac{(2\pi)^2}{A_{(\alpha)}^{(2-l)} A_{(\beta)}} \sum C_a^{\text{process}}(\alpha, \beta), ((\alpha, \beta) \in \mathbb{N}_{p, \theta}^2). \end{aligned} \quad (\text{C4})$$

We control the change of those scales for each time step less than 5% via a primary time step size goal

$$\Delta t_{\text{goal}} = \frac{0.05}{\max\left\{\left|\frac{\partial_t n}{n}\right|, \left|\frac{\partial_t e}{e}\right|, \left|\frac{\partial_t p_L}{p_L}\right|, \left|\frac{\partial_t m_D^2}{m_D^2}\right|, \left|\frac{\partial_t m_{Qf}^2}{m_{Qf}^2}\right|, \left|\frac{\partial_t m_D^2 T^*}{m_D^2 T^*}\right|\right\}}. \quad (\text{C5})$$

In order to have a smooth change of the time step size, we ultimately choose time step size for step i as

$$\Delta t_i = (\Delta t_{i-1}^3 \Delta t_{\text{goal}})^{\frac{1}{4}}. \quad (\text{C6})$$

-
- [1] P. Romatschke and U. Romatschke, *Relativistic Fluid Dynamics In and Out of Equilibrium*, Cambridge Monographs on Mathematical Physics (Cambridge University Press, Cambridge, England, 2019), ISBN 978-1-108-48368-1, 978-1-108-75002-8, arXiv:1712.05815.
- [2] P. Romatschke, *Int. J. Mod. Phys. E* **19**, 1 (2010).
- [3] C. Shen and L. Yan, arXiv:2010.12377.
- [4] A. Kurkela and Y. Zhu, *Phys. Rev. Lett.* **115**, 182301 (2015).
- [5] P. Romatschke, *Phys. Rev. Lett.* **120**, 012301 (2018).
- [6] A. Kurkela, A. Mazeliauskas, J.-F. Paquet, S. Schlichting, and D. Teaney, *Phys. Rev. Lett.* **122**, 122302 (2019).
- [7] A. Kurkela, A. Mazeliauskas, J.-F. Paquet, S. Schlichting, and D. Teaney, *Phys. Rev. C* **99**, 034910 (2019).
- [8] A. Kurkela and A. Mazeliauskas, *Phys. Rev. Lett.* **122**, 142301 (2019).
- [9] D. Almaalol, A. Kurkela, and M. Strickland, *Phys. Rev. Lett.* **125**, 122302 (2020).
- [10] M. Strickland, J. Noronha, and G. Denicol, *Phys. Rev. D* **97**, 036020 (2018).
- [11] M. P. Heller, R. A. Janik, and P. Witaszczyk, *Phys. Rev. Lett.* **108**, 201602 (2012).
- [12] M. P. Heller, A. Kurkela, M. Spaliński, and V. Svensson, *Phys. Rev. D* **97**, 091503 (2018).
- [13] A. Kurkela, W. van der Schee, U. A. Wiedemann, and B. Wu, *Phys. Rev. Lett.* **124**, 102301 (2020).
- [14] J.-P. Blaizot and L. Yan, *Phys. Lett. B* **780**, 283 (2018).
- [15] J.-P. Blaizot and L. Yan, *Ann. Phys. (Amsterdam)* **412**, 167993 (2020).
- [16] K. Harigaya and K. Mukaida, *J. High Energy Phys.* **05** (2014) 006.
- [17] K. Mukaida and M. Yamada, *J. Cosmol. Astropart. Phys.* **02** (2016) 003.
- [18] T. Asaka, D. Grigoriev, V. Kuzmin, and M. Shaposhnikov, *Phys. Rev. Lett.* **92**, 101303 (2004).
- [19] Y. Aoki, Z. Fodor, S. Katz, and K. Szabo, *Phys. Lett. B* **643**, 46 (2006).
- [20] Y. Aoki, S. Borsanyi, S. Durr, Z. Fodor, S. D. Katz, S. Krieg, and K. K. Szabo, *J. High Energy Phys.* **06** (2009) 088.
- [21] S. Borsanyi, Z. Fodor, C. Hoelbling, S. D. Katz, S. Krieg, C. Ratti, and K. K. Szabo (Wuppertal-Budapest Collaboration), *J. High Energy Phys.* **09** (2010) 073.
- [22] A. Bazavov *et al.*, *Phys. Rev. D* **85**, 054503 (2012).
- [23] N. Haque, A. Bandyopadhyay, J. O. Andersen, M. G. Mustafa, M. Strickland, and N. Su, *J. High Energy Phys.* **05** (2014) 027.
- [24] J. Ghiglieri, G. D. Moore, and D. Teaney, *J. High Energy Phys.* **03** (2018) 179.
- [25] J. Ghiglieri, G. D. Moore, and D. Teaney, *Phys. Rev. Lett.* **121**, 052302 (2018).
- [26] P. B. Arnold, G. D. Moore, and L. G. Yaffe, *J. High Energy Phys.* **05** (2003) 051.
- [27] P. B. Arnold, G. D. Moore, and L. G. Yaffe, *J. High Energy Phys.* **11** (2000) 001.
- [28] G. Giacalone, A. Mazeliauskas, and S. Schlichting, *Phys. Rev. Lett.* **123**, 262301 (2019).
- [29] P. M. Chesler and L. G. Yaffe, *Phys. Rev. Lett.* **102**, 211601 (2009).
- [30] V. Balasubramanian, A. Bernamonti, J. de Boer, N. Copland, B. Craps, E. Keski-Vakkuri, B. Müller, A. Schafer, M. Shigemori, and W. Staessens, *Phys. Rev. Lett.* **106**, 191601 (2011).
- [31] L. Keegan, A. Kurkela, P. Romatschke, W. van der Schee, and Y. Zhu, *J. High Energy Phys.* **04** (2016) 031.
- [32] S. Schlichting and D. Teaney, *Annu. Rev. Nucl. Part. Sci.* **69**, 447 (2019).
- [33] J. Berges, M. P. Heller, A. Mazeliauskas, and R. Venugopalan, *Rev. Mod. Phys.* **93**, 35003 (2021).
- [34] R. Baier, A. H. Mueller, D. Schiff, and D. Son, *Phys. Lett. B* **502**, 51 (2001).
- [35] D. Bodeker, *J. High Energy Phys.* **10** (2005) 092.
- [36] A. Kurkela and G. D. Moore, *J. High Energy Phys.* **12** (2011) 044.
- [37] J.-P. Blaizot, F. Gelis, J.-F. Liao, L. McLerran, and R. Venugopalan, *Nucl. Phys.* **A873**, 68 (2012).
- [38] A. Kurkela and G. D. Moore, *Phys. Rev. D* **86**, 056008 (2012).
- [39] S. Schlichting, *Phys. Rev. D* **86**, 065008 (2012).
- [40] J. Berges, K. Boguslavski, S. Schlichting, and R. Venugopalan, *Phys. Rev. D* **89**, 074011 (2014).
- [41] J. Berges, K. Boguslavski, S. Schlichting, and R. Venugopalan, *Phys. Rev. D* **89**, 114007 (2014).
- [42] R. Micha and I. I. Tkachev, *Phys. Rev. D* **70**, 043538 (2004).
- [43] J. Berges, K. Boguslavski, S. Schlichting, and R. Venugopalan, *Phys. Rev. Lett.* **114**, 061601 (2015).

- [44] A. Piñeiro Orioli, K. Boguslavski, and J. Berges, *Phys. Rev. D* **92**, 025041 (2015).
- [45] J. Berges, M. Mace, and S. Schlichting, *Phys. Rev. Lett.* **118**, 192005 (2017).
- [46] A. Kurkela and E. Lu, *Phys. Rev. Lett.* **113**, 182301 (2014).
- [47] J.-P. Blaizot, B. Wu, and L. Yan, *Nucl. Phys.* **A930**, 139 (2014).
- [48] F. Scardina, D. Perricone, S. Plumari, M. Ruggieri, and V. Greco, *Phys. Rev. C* **90**, 054904 (2014).
- [49] Z. Xu, K. Zhou, P. Zhuang, and C. Greiner, *Phys. Rev. Lett.* **114**, 182301 (2015).
- [50] A. Kurkela and A. Mazeliauskas, *Phys. Rev. D* **99**, 054018 (2019).
- [51] K. Zhou, Z. Xu, P. Zhuang, and C. Greiner, *Phys. Rev. D* **96**, 014020 (2017).
- [52] P. B. Arnold, G. D. Moore, and L. G. Yaffe, *J. High Energy Phys.* **01** (2003) 030.
- [53] X. Du and S. Schlichting, Companion Letter, *Phys. Rev. Lett.* **127**, 122301 (2021).
- [54] M. C. Abraao York, A. Kurkela, E. Lu, and G. D. Moore, *Phys. Rev. D* **89**, 074036 (2014).
- [55] E. Lu, Ph.D. thesis, McGill U., 2015.
- [56] L. Landau and I. Pomeranchuk, *Dokl. Akad. Nauk Ser. Fiz.* **92**, 735 (1953).
- [57] L. Landau and I. Pomeranchuk, *Dokl. Akad. Nauk Ser. Fiz.* **92**, 535 (1953).
- [58] A. B. Migdal, *Dokl. Akad. Nauk Ser. Fiz.* **105**, 77 (1955).
- [59] P. B. Arnold, *Phys. Rev. D* **79**, 065025 (2009).
- [60] Y. L. Dokshitzer, *Sov. Phys. JETP* **46**, 641 (1977).
- [61] V. Gribov and L. Lipatov, *Sov. J. Nucl. Phys.* **15**, 438 (1972).
- [62] G. Altarelli and G. Parisi, *Nucl. Phys.* **B126**, 298 (1977).
- [63] A. Anisimov, D. Besak, and D. Bodeker, *J. Cosmol. Astropart. Phys.* **03** (2011) 042.
- [64] H. Bethe and W. Heitler, *Proc. R. Soc. A* **146**, 83 (1934).
- [65] P. B. Arnold and C. Dogan, *Phys. Rev. D* **78**, 065008 (2008).
- [66] N. Nielsen and P. Olesen, *Nucl. Phys.* **B144**, 376 (1978).
- [67] A. Krasnitz, Y. Nara, and R. Venugopalan, *Nucl. Phys.* **A717**, 268 (2003).
- [68] T. Lappi, *Phys. Rev. C* **67**, 054903 (2003).
- [69] T. Lappi and L. McLerran, *Nucl. Phys.* **A772**, 200 (2006).
- [70] J.-P. Blaizot, T. Lappi, and Y. Mehtar-Tani, *Nucl. Phys.* **A846**, 63 (2010).
- [71] J. Berges, B. Schenke, S. Schlichting, and R. Venugopalan, *Nucl. Phys.* **A931**, 348 (2014).
- [72] T. Epelbaum and F. Gelis, *Phys. Rev. Lett.* **111**, 232301 (2013).
- [73] J. Berges, K. Boguslavski, S. Schlichting, and R. Venugopalan, *J. High Energy Phys.* **05** (2014) 054.
- [74] S. Nazarenko, *Lecture Notes in Physics (825): Wave Turbulence* (Springer, New York, 2011).
- [75] J.-P. Blaizot, E. Iancu, and Y. Mehtar-Tani, *Phys. Rev. Lett.* **111**, 052001 (2013).
- [76] Y. Mehtar-Tani and S. Schlichting, *J. High Energy Phys.* **09** (2018) 144.
- [77] S. Schlichting and I. Soudi, *J. High Energy Phys.* **07** (2021) 077.
- [78] A. H. Mueller, *Phys. Lett. B* **475**, 220 (2000).
- [79] S. Mrowczynski, *Phys. Lett. B* **314**, 118 (1993).
- [80] P. B. Arnold, J. Lenaghan, and G. D. Moore, *J. High Energy Phys.* **08** (2003) 002.
- [81] P. Romatschke and M. Strickland, *Phys. Rev. D* **68**, 036004 (2003).
- [82] P. Romatschke and M. Strickland, *Phys. Rev. D* **70**, 116006 (2004).
- [83] E. S. Weibel, *Phys. Rev. Lett.* **2**, 83 (1959).
- [84] S. Hauksson, S. Jeon, and C. Gale, *Phys. Rev. C* **103**, 064904 (2021).
- [85] A. Mazeliauskas and J. Berges, *Phys. Rev. Lett.* **122**, 122301 (2019).
- [86] J. Bjorken, *Phys. Rev. D* **27**, 140 (1983).
- [87] M. Gyulassy and T. Matsui, *Phys. Rev. D* **29**, 419 (1984).
- [88] J. Ghiglieri, G. D. Moore, and D. Teaney, *J. High Energy Phys.* **03** (2016) 095.
- [89] J. Ghiglieri and D. Teaney, *Int. J. Mod. Phys. E* **24**, 1530013 (2015).